Title
Ultrafast Dynamics Studied by Few-Femtosecond Soft X-ray Transient Absorption Spectroscopy

Author
Ross, Andrew Dean

Publication Date
2022

Peer reviewed|Thesis/dissertation

Ultrafast Dynamics Studied by Few-Femtosecond Soft X-ray Transient Absorption Spectroscopy

by

Andrew Dean Ross

A dissertation submitted in partial satisfaction of the

requirements for the degree of

Doctor of Philosophy

in

Chemistry

in the

Graduate Division

of the

University of California, Berkeley

Committee in charge:

Professor Stephen R. Leone, Co-chair
Professor Daniel M. Neumark, Co-chair
Professor Graham R. Fleming
Professor David Attwood

Spring 2022

Ultrafast Dynamics Studied by Few-Femtosecond Soft X-ray Transient Absorption Spectroscopy

Abstract

Ultrafast Dynamics Studied by Few-Femtosecond Soft X-ray Transient Absorption Spectroscopy

by

Andrew Dean Ross

Doctor of Philosophy in Chemistry

University of California, Berkeley

Professor Stephen R. Leone, Co-chair

Professor Daniel M. Neumark, Co-chair

X-ray Transient Absorption Spectroscopy (XTAS) has enabled real time measurements of numerous physical processes of great chemical importance. The technique is sensitive to electronic and molecular structure with element specificity and short time resolution. However, XTAS experiments that can probe carbon-containing molecules are still in their infancy. An apparatus is designed and constructed that provides efficient X-ray flux to probe transitions from the carbon 1*s* shell to the valence levels. The apparatus is able to use a visible pump pulse, less than 5 fs in duration, and a few-femtosecond cross-correlation is established. In vibrational studies of small molecules, core-excited potential energy surfaces along the symmetric stretch normal mode are extracted. Other vibrational modes are not observed, and the reasons are discussed as a limitation of XTAS. Dissociation of strong-field ionized CCl_4^+ is tracked in real time, measuring a time scale associated with Jahn-Teller distortion in this system. The signal also shows two previously unobserved intermediates in a symmetry-broken covalently bonded form of CCl_4^+ and a non-covalently bonded complex between a CCl_3^+ moiety and atomic Cl. Additionally, an excited state that results in Cl^+ and CCl_3 is observed. Finally, experiments measuring the electronic properties of solid-state systems are undertaken that show similar recombination times in semiconducting and metallic-containing single-walled carbon nanotube bundles, among other results.

To my family

Contents

List of Figures

List of Tables

Acknowledgments

The work in this thesis would not be possible without the help of many individuals that I have been fortunate to have met in my life. To start, I would like to thank my advisors Steve Leone and Dan Neumark. They have been a great source of wisdom and guidance, and I'm glad they took me into their groups in my first year.

Secondly, I'd like to thank my mentors and teachers. When I first started learning, Peter Kraus and Chris Kaplan showed me the ropes and taught me not just what I needed to know to run the experiment, but also how to be a good scientist. The knowledge that I've learned has come from both excellent academic teachers and the myriad of friends in stimulating conversations.

Next, the work that I've done cannot be done without an extra pair of hands and a second head. I thank Lou Barreau not just for her excellent work but also for her guidance and for being a great lab mate. She had a big part in building what was created. I have also had the pleasure of working with Valeriu Scutelnic, Eric Haugen, Enrico Ridente, Samay Garg, Mikias Balkew, and Emma Berger, and everyone else in the Leone and Neumark groups.

Diptarka Hait has been a good friend since the I arrived in Berkeley. He's a great person, incredibly understanding. He's also the smartest researcher I know, and his help was absolutely vital to this work.

And I got to meet the guys in the wood and metal shops. When I started working, the room was a blank floor, and it was only with the help of Doug Scudder, Jody Brenner, Gerald J Poole, Ryan Woloshyn, Clint Jessel, David Karst, Emanuel Druga, and Mike Brateng that the infrastructure got installed and the equipment got built. And, they're always good for a laugh.

Finally, I'd like to thank my family. My parents have been the most wonderfully supportive parents throughout my whole life and career. They are amazing and incredible human beings, and I'm lucky to call them Mom and Dad.

Chapter 1

Introduction

At its core, chemistry is the study of the rearrangement of atoms and electrons. In everyday life, people experience chemistry in the baking of a cake, rusting of iron, or changing colors of leaves. We perceive these as taking a long time for the whole object, but the physics that govern these on the atomic scale is much faster[1], on the order of femtoseconds (fs), 10^{-15} seconds. To put this timescale in perspective, there are as many femtoseconds in one minute as there are minutes in the lifetime of the universe[2].

On this timescale, molecules can vibrate at periods ranging from 7.7 fs for the light atoms in H_2[3], to relatively slowly, 1,111 fs for larger movement in DNA[4]. Molecules can absorb light and break apart into smaller pieces in 10 fs to 10,000 fs or longer[5]. In solids, electrons can dissipate energy and recombine in this time, and the specifics are very important for industries such as the manufacture of solar cells[6]. The femtosecond is the time scale on which many important processes occur, and having access to the first few femtoseconds allows many more of these processes to be studied.

Additionally, some of the most important systems to study are carbon-containing molecules and solids. They include the organic molecules that are vital to life, for which the chemical dynamics govern the processes of our bodies. They also include simple molecules, such as CO_2, which exhibit clear-cut examples of fundamental processes that can be studied most easily in basic systems. There are also new crops of carbon-based electronics that use the unique bonding of carbon for different purposes in things like graphene and diamond[7, 8]. Being able to study carbon at the few-femtosecond time scale can provide new insight into the basic fundamental chemistry that drives much of the world around us.

1.1 Pump-Probe Experiments

This thesis will cover several different processes in gases and solids. They are fast enough that they cannot be studied with electronics, as computers have processing speeds that are a million times slower than some of these processes. Instead, specialized tools and techniques that use light are employed in order to illuminate the ultrafast world.

One of the main ways that ultrafast dynamics are measured is with a technique called pump-probe spectroscopy, heralded by Ahmed Zewail, Nobel prize winner in 1999[5]. It uses light separated into two pulses, a pump and a probe. The probe acts as a camera for the system, capturing its state at a given time. Usually, the state is measured by the absorption of the light of the probe pulse, where different materials absorb different colors[9, 10].

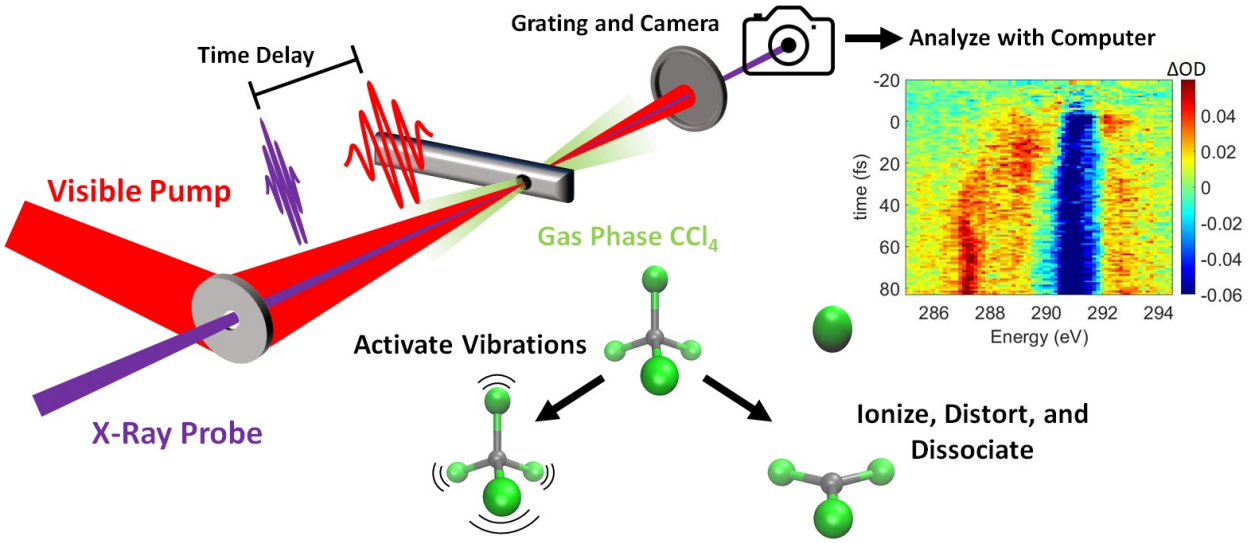

Figure 1.1: A representation of the experiment used in this thesis. It uses a visible pump pulse to excite samples, such as CCl_4, starting vibrations, ionization, dissociation, and other ultrafast dynamics. After a delay, the sample is probed by absorption of an X-ray pulse. The X-ray is dispersed onto a camera with a grating, which is analyzed with a computer. Changes are observed in the absorption energies (x-axis) as the probe measures early times (top) to later times (bottom).

With just the probe pulse, the system remains in a ground state, and the probe would measure only the static absorption. In order for the probe to measure the transient dynamics of the system, the ultrafast processes must be induced. The pump pulse excites the sample and starts the ultrafast processes, and after a delay, the probe measures the state of the system. In the time between the two pulses, the system evolves according to the physical laws. By changing the delay between pump and probe, the state of the system is measured at different times in that process, which is accomplished by physically altering the path length of one of the pulses with the distance being converted to time by dividing by the speed of light[9]. If the probe acts as a camera, taking pictures of the system at any given time, changing the delay with respect to the pump turns the pictures into a "molecular movie," allowing the dynamics to be viewed in "real time"[11, 12]. An example of the pump-probe technique used in this thesis is shown in Fig. 1.1.

To continue the metaphor of a camera and movie, a camera with a long shutter speed may be appropriate for taking pictures of mountains, but cannot used to take pictures of a sporting event, as the image will blur all their movement together. Similarly, the shortest processes that can be measured are limited by how short the laser pulses are. Both the pump and probe pulse durations need to be short to have good resolution in time, as the temporal resolution is determined by the convolution of the duration of the two pulses, called the cross-correlation[9]. Therefore, in order to measure femtosecond processes, femtosecond pulses are necessary.

At the level of measuring few-femtosecond processes, the Heisenberg uncertainty principle needs to be considered[13]. The well-known equation that limits how precisely the position and momemtum can be known can be converted to show the same limit between energy and time:

$$\Delta x \Delta p \geq \frac{\hbar}{2} \rightarrow \Delta E \Delta t \geq \frac{\hbar}{2}$$

For a time resolution of 1 fs, the energy resolution must be worse than 1.825 eV[14], which is often not sufficient resolution for the probe to distinguish between the different absorption colors in different states of a system[15]. Fortunately, pump-probe spectroscopy can get around this limitation by first interrogating the sample with the probe, utilizing the short temporal duration, followed by separation of the probe pulse into its colors by a grating, which can give energy resolution less than 0.1 eV[15].

The uncertainty principle also affects how the pump and probe pulses are prepared. In order to get short pulse durations, the range of photon energies in the pulse must span a relatively wide range. The laser systems that can be purchased directly from companies typically only support 30 fs pulses with 0.07 eV bandwidth (35 nm bandwidth at 800 nm)[16]. This must be broadened in energy to cover several eV with all energies kept in phase to support nearly single-cycle pulses down to 3.5 fs[15, 17], as is described in Chapter 2, which is used for the pump pulse. Similarly, the probe must span several eV to maintain the temporal resolution, which can be easily accomplished at higher photon energies, up to the X-ray.

1.2 X-Ray Spectroscopy

While there are many variants of pump-probe spectroscopy that use different pumps, probes, and number of pulses[15, 18–20], the experiment in this thesis uses a relatively simple variant called X-ray Transient Absorption Spectroscopy (XTAS). It is X-ray by using X-ray light as a probe, transient by using a variable pump-probe delay, and absorption spectroscopy by measuring the absorption of the probe pulse. X-rays are generally considered to start at 145 eV, and this thesis uses the range 145 - 370 eV to refer to soft X-rays[21].

Using X-rays as a probe has several advantages over visible light. The first is that it can support shorter temporal durations, as an X-ray pulse can have bandwidths of 100s of eV[22]. The higher energy of X-rays over visible light means that the wavelength of X-ray

light is shorter, so the duration of the pulse is less limited by the period of an oscillation[22]. State-of-the-art equipment has shown to be able to produce X-ray pulses as short as 43 attoseconds (as, 10^{-18} s)[23].

The second advantage X-rays have is that they allow different elements in a sample to be probed separately. When a molecule absorbs an X-ray, it excites an electron from one of its core levels to a valence level[24]. The core levels of elements have energies that strongly depend on the positive charge of the nucleus, and thus the identity of the element. Core levels can be separated by 10s of eV for the constituent atoms in a molecule, such as the carbon $1s$ level at 284 eV, the chlorine $2p$ level at 200 eV, or the sulfur $2p$ level at 163 eV[25]. With access to individual elements, the local environment around those elements can be probed, such as the local charge around an element[24, 26].

In order to probe a state with the core shell of an atom, two conditions must be met. The first is that the valence level must have spatial overlap with the atom[22]. The atom's core levels are highly localized around the atom, and the electron cannot easily move from that atom to valence states on another atom, far away. This is not an issue for most of the bonding and anti-bonding orbitals of the small molecules in this thesis, but it can be an issue for non-bonding states that can only be probed from their atom[22]. The other condition is that for the absorption of a photon there must be a change in dipole between the initial state and the final state, which is known as the Laporte rule[27]. This most strictly applies to atoms, where transitions from $s \rightarrow s$ or $p \rightarrow p$ orbitals are forbidden, but it also applies to molecules and solids where a transition can be forbidden or significantly weaker if the valence state has the same symmetry as the core state[27]. These are called dark states in X-ray spectroscopy, and it imposes limitations on the states that can be probed by XTAS[18].

The third advantage is that X-rays provide a transition that can measure each of the valence states from a common energy level. This is especially useful in solids, where visible spectroscopy measures the difference between the valence band and the conduction band, as a unit[28]. By exciting from a core level, the valence band can be probed separately from the conduction band. That can be necessary for a measurement, because the dynamics of electrons excited into the conduction band can be very different than the dynamics of holes left in the valence band[28]. Similarly, in molecules, the absolute energy of each electronic band can be measured, instead of just the relative energies between each.

X-ray Sources

The act of generating X-rays is not difficult in concept. Indeed, X-rays can be generated by simply peeling sticky tape in a vacuum[29], and X-rays are commonly used in dental and other medical equipment from electrons accelerated by charged plates from cathode to anode[30]. They can provide an abundance of photons. However, these X-rays are not coherent and cannot provide the time resolution required for pump-probe spectroscopy. In order to gain the benefits of probing with X-rays, a stable, high photon flux, and temporally short source of X-rays is essential, and they must have photon energies that corresponds to the elements of interest, specifically extending above the carbon K-edge ($1s$) at 284 eV.

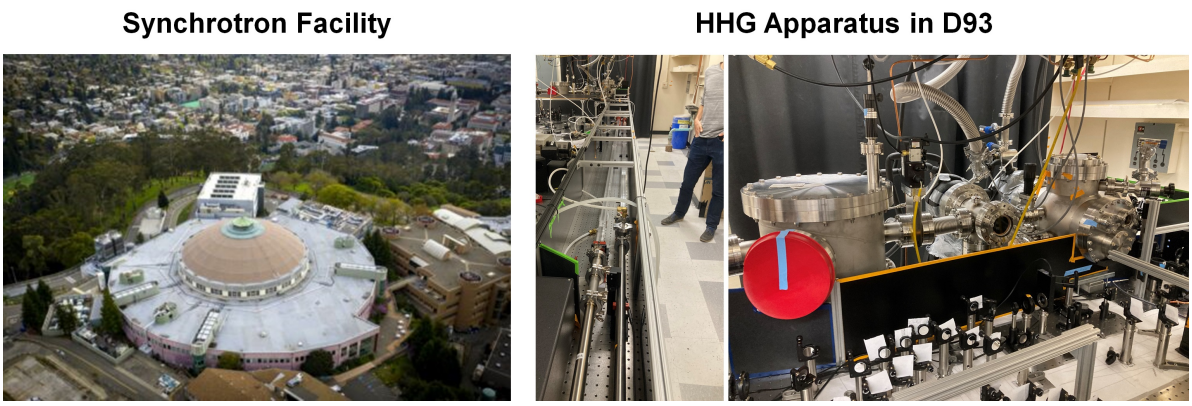

Figure 1.2: A comparison of the sizes of synchrotrons to HHG sources. The left shows the Advanced Light Source at Lawrence Berkeley National Laboratory (image from: https://berstructuralbioportal.org/als/), where the synchrotron comprises a ring along the circumference. The right shows the HHG source constructed here in room D93 in Hildebrand Hall.

For scientific X-ray sources, the gold standard for several years was synchrotron radiation[31–35]. Synchrotrons operate by acceleration of electron packets in a storage ring to high velocities over several kilometers, at which point the packets move through an undulator or wiggler, regions of alternating magnetic poles of different strength. The undulator or wiggler forces the electrons into a sinusoidal path, which generates light from the acceleration of each oscillation, and the energy of the generated X-ray photons can be changed by using different magnet spacings[31, 34]. The X-rays generated with synchrotrons is very bright, a high flux in the range of 10^{20} photons/(s*mm^2*mrad^2*0.1%bandwidth)[33]; although, the pulse durations of these sources can only be achieved in the 10s of picoseconds, based on the electron pulse durations, e.g. 60 ps for the Advanced Light Source at the Lawrence Berkeley National Laboratory in California, USA[34]. The picosecond scale is short and useful for many applications, but it is too long for the dynamics of interest in this thesis, on the femtosecond timescale.

A technology becoming increasing popular for use in this type of science is the free electron laser (FEL). The generation of light, similar to synchrotrons, comes from acceleration of electrons in a sinusoidal manner. However, in a free electron laser, the bunch of electrons interacts with X-ray light to force the electrons into packets, evenly spaced to lead to purely constructive interference and coherence in the emitted X-rays[36, 37]. This leads to significantly more efficient generation with brightnesses up to 10^{35} photons / (s*mm^2*mrad^2*0.1%bandwidth)[38] and pulse durations down to 2 fs[36, 37, 39].

Synchrotrons and FELs are incredibly useful scientifically, but they have the notable problem of being expensive. Each facility requires several square kilometers of space to appropriately accelerate their electrons, including large campuses and facilities dedicated to

their operation[31]. Another type of X-ray source is called high harmonic generation (HHG). It can be done on a tabletop in a single room, capable of operating with the electricity available to a typical house[16, 40]. An example of the size difference is shown in Fig. 1.2. HHG is capable of generating energies between 10s and 100s of eV[22, 41–44]. HHG does not produce nearly as many photons as synchrotrons, only producing $\sim 10^8$ photons/s in the soft X-ray[45]. However, it is capable of much better temporal resolution with pulses down to 43 as[23]. Very few apparatuses that use X-rays for the carbon K-edge exist in the world, and none existed that used a short 800 nm pump for measuring the processes of interest. So a new apparatus was designed and constructed by me and my coworkers, which is detailed later in this thesis, using HHG as the X-ray source, the process of which is explained below.

High Harmonic Generation

High Harmonic Generation (HHG) is a process that converts low energy photons to much higher energy photons, usually from visible or infrared (0.5 - 3 eV) to Extreme Ultraviolet (XUV) or X-ray (20 - 1000 eV)[22, 41–44]. Usually, sum frequency processes are only efficient in doubling the fundamental frequency, such as 92% of the fundamental energy converted to the 2^{nd} harmonic in special crystals, for a Nd:YAG laser in a material such as or BBO crystals[46], compared to frequency tripling at 0.001% efficiency in germanium[47]. The expected trend in efficiency based on second and third harmonic generation would suggest that higher order of harmonics would produce a flux of photons far too low for experiments. HHG has a relatively high efficiency of 10^{-3}% to 10^{-6}% to each harmonic[14]. The way this relatively efficient process is best understood is by the three-step model[48, 49], shown in figure 1.3.

The first step in the three-step model is tunnel ionization, usually in a noble gas, such as He. The light from the fundamental laser is considered from the wave nature of light's wave-particle duality. The wave contains an oscillating electric and magnetic field, and when the laser is focused to very high intensities, the electric field at a given time can be very large, around 6 V/Å for a typical intensity of 5×10^{14} W/cm^2. These high electric fields are strong enough to significantly disturb the potential of the electrons in the He potential well, shown in figure 1.3. With this potential bending, the barrier for the electron to break free of the He nucleus potential becomes small. A smaller barrier leads to increased probability of tunnel ionization, a quantum mechanical extension of the electron wavefunction through the barrier into free space and allows the electron to ionize without sufficient energy to exceed the remaining potential barrier[14, 41, 44]. Once the electron is tunnel ionized, it is free to be accelerated by the electric field.

The second step is propagation. This step describes the movement of the newly freed electron in the laser's electric field. Initially, the electric field responsible for ionization will accelerate the electron away from the He nucleus. However, the laser electric field is oscillating, and so after less than half a period of the fundamental frequency (1.33 fs for 800 nm input) the electric field will reverse directions and accelerate the electron back towards

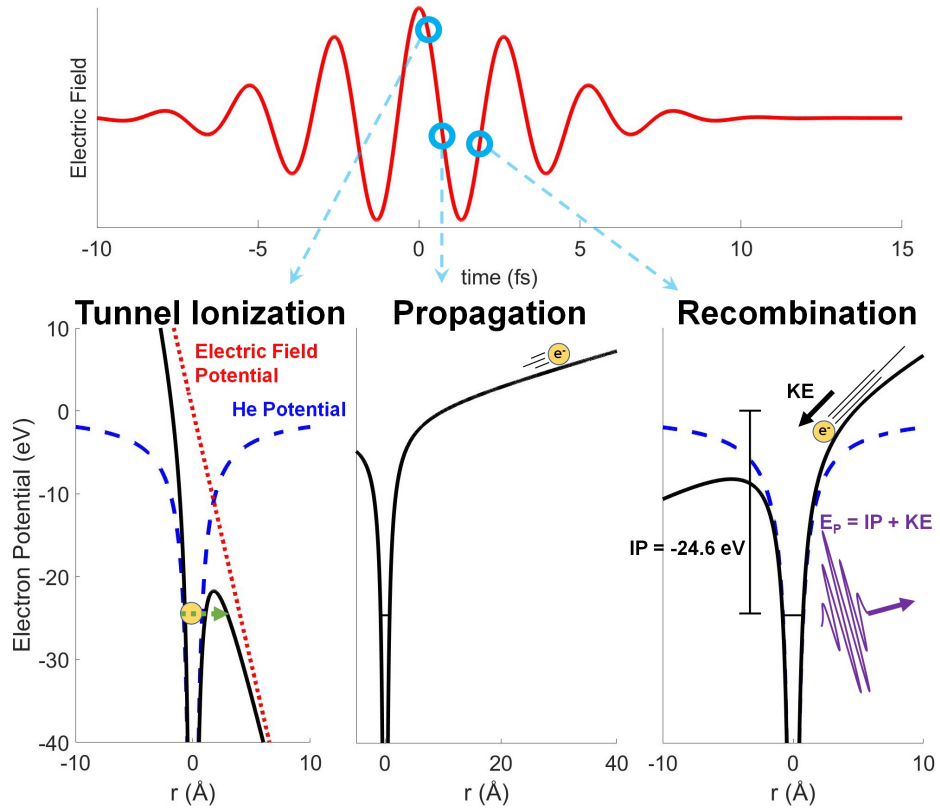

Figure 1.3: A visual representation of the HHG process during the strong electric field of a fundamental laser, corresponding to a maximum intensity of 5×10^{14} W/cm^2 (top). The bottom shows the three step process, Tunnel Ionization, Propagation, and Recombination[48, 49]. The blue dashed line is the potential of the electron in Helium with no field. The red line shows the potential of the electron due to the electric field, and the black line is the sum of the two potentials. The electron shown is a visual representation of the tunnel ionized electron. An additional electron that remains trapped near the He nucleus is not shown.

the He nucleus. As the electron accelerates, it gains increasing kinetic energy, and eventually it may collide with the nucleus[14, 50–52].

The third step is recombination. There is a probability that the fast moving electron can overlap the nucleus in space and recombine. The recombination of the two produces a photon output with energy:

$$E_{photon} = IP + KE_{electron}$$

where, IP is the ionization potential of the noble gas ($\text{IP}_{He} = 24.6$ eV[53]), and $\text{KE}_{electron}$ is the kinetic energy of the electron at the time of recombination[14]. The kinetic energy can be calculated as an integral of the energy the electron gains in the electric field, but more

useful is the maximum photon energy available:

$$E_{photon_{max}} = IP + 3.17U_P$$

where U_P is the ponderomotive energy, the cycle-averaged kinetic energy $U_P = \frac{e^2 E_a^2}{4m\omega^2}$, where e is the charge of the electron, E_a is the electric field amplitude, m is the mass of the electron, and ω is the frequency in radians of the fundamental laser pulse. The 3.17 multiplier applies to the trajectory that gains the greatest kinetic energy[14]. The important part of this equation is noting how it scales with the fundamental laser pulse; the intensity, I, is proportional to E_a^2 and the wavelength is $\lambda = c/(2\pi\omega)$, where c is the speed of light. The scaling for the maximum photon energy becomes:

$$E_{photon_{max}} \propto I \times \lambda^2$$

With this, visible light can be converted into XUV or X-rays[14, 22, 41–44, 48, 50–52].

Extension of High Harmonic Generation into Soft X-ray

In order to access photons at the carbon K-edge at 284 eV, most of the energy must come from the kinetic energy, as the ionization potential of noble gases only goes up to 24.6 eV in He[53]. With the above description, it may seem reasonable that extension of the photons can be achieved simply by increasing the intensity of the readily available and intense 800 nm lasers that can be purchased from manufacturers[16, 54, 55]. However, problems arise in practice. The electron is not a hard ball but more accurately a loose wavepacket of probability density. When the electric field is increased to the extent that the barrier to ionization is completely suppressed, the so-called over-the-barrier regime[52], the wavepacket can become very disperse and recombination is made extremely unlikely, resulting in near zero X-ray flux, unless very careful considerations are taken[50–52]. Therefore, even with the high IP of He, there is a limit to the electric field that can be realistically used to generate higher energy photons, and typically, 800 nm is used as a fundamental driving laser up to ∼120 eV[56, 57].

The solution that several have found successful is to increase the wavelength of the driving laser to make use of the λ^2 scaling. Physically, this allows the electron to spend more time accelerating before the electric field inverts. More acceleration means more kinetic energy and higher energy photons, but it also means that the electron wavepacket has more time to diffuse, which lowers the likelihood of recombination. The scaling of HHG efficiency that has been observed is $\lambda^{-5.5}$[22, 58, 59], so an arbitrarily long wavelength cannot be used to do experiments at arbitrarily high energies. A handful of apparatuses have been constructed using drivers of 1300 nm[60, 61], 1800 nm[61–63], 3000 nm[64], and others. These have reached up to 1000 eV[65] and performed transient experiments up to the titanium L-edge at 460 eV[66]. This experiment will use 1300 nm to have high efficiency in the soft X-ray, including the carbon K-edge.

It has also recently been shown that higher energy photons can be made with short wavelength drivers by using intensities strong enough to ionize the HHG medium and then generate HHG with the ions, referred to as the overdriven regime[67, 68]. The higher ionization energies of the ions allow stronger electric fields and higher energy photons.

Maintaining Short Pulses

Simply generating photons with HHG is not sufficient to get probe pulses short enough to study the ultrafast dynamics desired. At each reversal of the electric field in the fundamental laser, HHG can potentially result in a recombination event and an X-ray photon. A long series of these recombinations leads to an X-ray pulse train, which has total length similar to the fundamental laser pulse and would limit the temporal resolution of the pump-probe experiment[22, 24, 52]. The simplest solution is to make the fundamental pulse shorter. This limits the number of oscillations that have an electric field intense enough to induce tunnel ionization and is known as amplitude gating[22, 69].

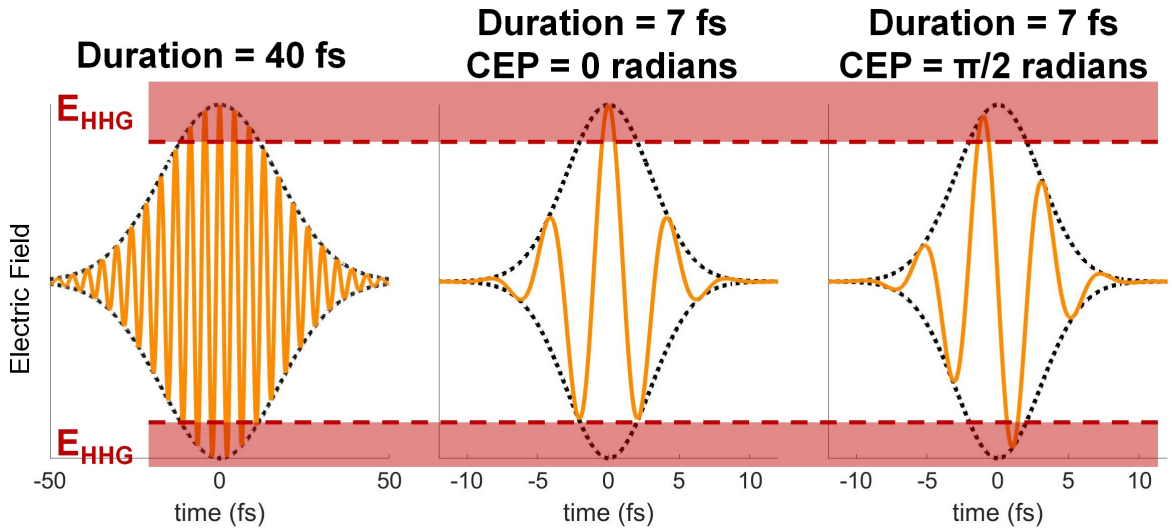

Figure 1.4: Longer HHG driving pulses lead to multiple potential HHG bursts. Making a simplification that tunnel ionization only occurs at electric fields exceeding a certain value, the figure on the left shows the 40 fs, 1300 nm pulse would lead to nine bursts of photons. The middle shows a compression of the pulse that leads to only one cycle that exceeds this critical electric field. However, pulses with the same duration but different carrier-envelope phase (CEP) can produce two bursts, shown on the right.

In the extreme case, amplitude gating can result in only a single X-ray burst, ejected at a particular time within the period of the fundamental. This can lead to X-ray pulses that are much shorter than the fundamental pulses. X-rays with duration on the order of 100s

of attoseconds have been routinely achieved, and the current record is 43 as[23]. However, obtaining these short pulses requires extreme control of the properties of the fundamental laser. As mentioned earlier, the overall duration of the laser, called the envelope, can only be made short by combining a large range of frequencies together to overcome limitations imposed by the uncertainty principle and by keeping the frequencies in phase[22, 24, 70]. This is often expressed as keeping the group delay dispersion (GDD) and higher order dispersions close to 0[70, 71]. In addition to making the envelope short, the electric field can shift within the envelope, called the carrier-envelope phase (CEP). Changing the CEP by $\pi/2$ radians can result in 2 separate recombinations, shown in Fig. 1.4. The emissions are spaced by half a period of the fundamental, so making harmonics with a short pulse but no CEP will result in temporal resolution in the 1-2 fs range, instead of the optimal 100 as range[22, 24, 72, 73].

In terms of the HHG spectrum that will be generated, in the optimal case with a short fundamental and CEP of 0 radians, the energy range of X-rays is continuous[24, 72, 74, 75]. However, without CEP, multiple X-ray bursts may be created that interfere constructively or destructively with one another, called phase matching[22, 24, 36]. The period of the fundamental and the centrosymmetric noble gas medium for HHG produce constructive interference for odd harmonics of the fundamental and destructive interference for even harmonics. This results in modulation in the spectrum, which can lead to noise. The extension with a very long fundamental laser produces strong phase matching and very discrete peaks in the X-ray spectra at odd harmonics, a 2ω energy spacing[22, 24, 36].

1.3 X-ray Signals and Analysis

While the presence of the appropriate photons theoretically enables measurement of ultrafast processes, the signals are meaningless without appropriate analysis. This section gives an overview of how the raw data is manipulated and what signals are expected to coincide with which processes.

When a measurement is taken, the physical quantity that is measured is the number of photons that strike a particular region of a CCD camera, measuring a spectrum. The region of the CCD corresponds to particular energies, defined by diffraction of the X-rays by a grating, which is calibrated by measuring the lack of photons at known energies from the absorption of common species. The absorption of a sample can be measured by comparing the measured signal with the sample and without the sample:

$$OD = -\log_{10}(I/I_0)$$

where OD is the optical density (OD), also called absorbance, I is the signal with sample, and I_0 is incident X-ray flux, the signal without the sample. Obtaining I_0 requires physically moving the sample out of the path of X-rays, which reduces the experimental duty cycle.

For a pump-probe transient measurement, the absorption of most samples are not expected to change drastically, so the change in optical density, ΔOD, is a quantity that

highlights the processes more effectively. This quantity can be obtained by taking spectra with the pump on and off:

$$\Delta OD = \left(-\log_{10}\left(\frac{I_{on}}{I_0}\right)\right) - \left(-\log_{10}\left(\frac{I_{off}}{I_0}\right)\right) = -\log_{10}\left(\frac{I_{on}}{I_{off}}\right)$$

where I_{on} is the spectrum measured with the pump on and I_{off} is the spectrum with pump off. This quantity can be measured without measuring the incident flux, I_0, due to cancellation within the logarithms, which means the sample does not need to be physically moved and saves time in data collection.

Due to the low number of photons in the X-ray probe, especially in the soft X-ray, compared to the infrared region, there is considerably more noise in the X-ray data. Large portions of this noise are due to changes in the harmonic flux, which are correlated across the energy spectrum and can be removed. The first of this type of noise is HHG intensity fluctuations, where the overall flux across the entire energy range is reduced temporarily. This can occur due to vibrations in the table, hiccups in the He gas flow, modulations of the laser, or some other parameter that cannot be effectively controlled. If this happens during a pump on measurement, a positive ΔOD will appear across the spectrum, and a negative signal will appear during a pump off measurement. The second type of noise is HHG energy fluctuations, where the phase-matching conditions are changed and the peaks of HHG flux at the odd-harmonics are shifted[24, 76]. This is particularly a problem for short fundamental pulses where the phase-matching is not strictly enforced by many X-ray bursts and changes in the CEP produce significant changes to the HHG. These fluctuations introduce noise at repeated 2ω of the fundamental spacing in the ΔOD data.

Both of these noise sources can be corrected out, though. By choosing a region of energies where a ΔOD of 0 is expected, the correlation matrix of that region can be calculated and applied to the rest of the energies, in an algorithm created by other members of this group called"edge referencing"[76]. This severely reduces the noise associated with HHG intensity and energy fluctuations, and it is essentially necessary for working with the less stable extension to the soft X-ray. Those noise sources are not the only noise in the experiment; there is always random shot noise from the camera, for example, which cannot be removed and will be more significant with the lower photon counts.

Gas Phase Signals

With a lower noise, the XTAS signal can be observed. The most common type of signal is a negative ΔOD called "ground state bleaching"[24, 77]. In its simplest form, bleaching means that OD at a particular energy is lower after excitation from the pump than before in the ground state; the change in OD is negative. Usually, the bleach is strongest where the ground state has the highest absorption (static absorption), where there is the most absorption to be lost. Commonly, the ground state bleach refers to population of the ground state being converted to an excited state, which absorbs more at a different energy and results in a positive ΔOD. As a fairly effective simplification, negative ΔOD means the ground state

population is reduced, and positive ΔOD means that a new state is being formed with absorption at those energies.

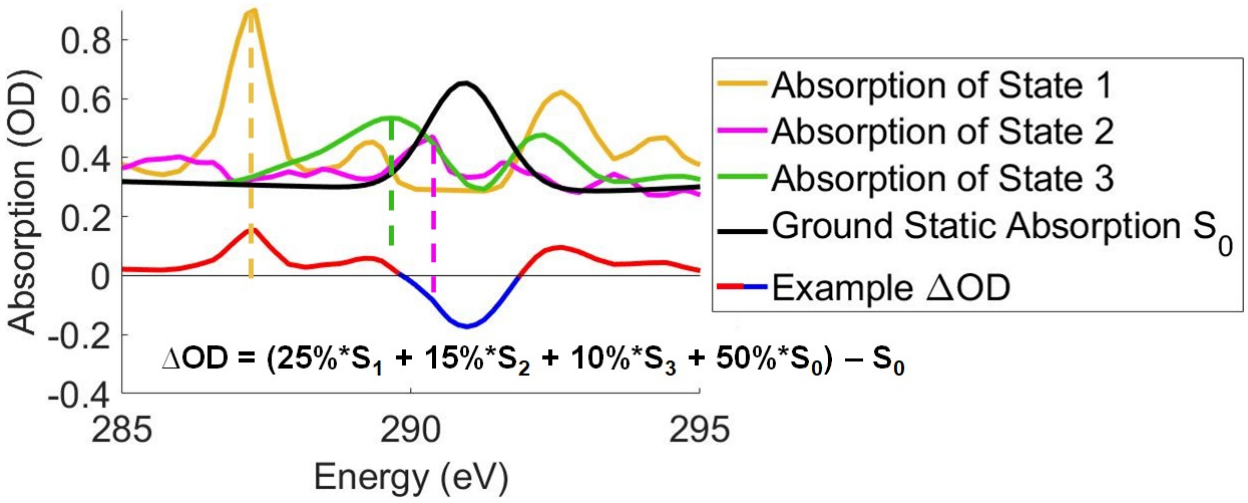

Figure 1.5: The absorption of three different excited states of CCl_4 and the ground state are shown on top. An example ΔOD signal is shown below, containing 25% State 1, 15% State 2, 10% State 3, and 50% remaining in the ground state. The ground state bleach from loss of the ground state is colored blue. The positive ΔOD from the absorption of the new species is shown in red. Absorption features can be observed in the bleach as kinks on top of the broad signal. Disambiguating multiple states from the ΔOD start point can be difficult, but it is possible by comparing multiple time points and pump intensities.

These new states can be from excited electronic states, ionized molecules, molecules that have dissociated, or something different; although, the specific types of signals from each can be very different from molecule to molecule. Determining exactly which signals correspond to which species is usually done by comparison of their energies to previous literature or computed spectra[78–80]. That said, excited electronic states in the types molecules typically studied are exciations from a filled highest occupied molecular orbital (HOMO) to an unoccupied orbital, often the lowest unoccupied molecular orbital (LUMO). The HOMO becomes partially unfilled, which allows the transition from the core level to the lower energy former HOMO and creates an absorption at lower energies, a positive ΔOD signal at lower energies. This is referred to as state opening[17, 81]. Similarly, the partially filled LUMO has reduced transition probability, due to being partially occupied, and so the absorption at that energy goes down, and an intense ground state bleach is observed at that energy, which is referred to as state blocking[15, 17, 81, 82]. At other energies, the electronic state will change the absorption, depending on the molecule, which will show additional changes[17]. These effects can be reduced if some or all of these transitions are

dipole forbidden or disallowed[18, 83].

For ionized molecules, an electron is lost, and there is an expected positive ΔOD, similar to the HOMO, at the electronic state from which the electron was lost. However, there is no associated state blocking, as the electron is no longer bound to the molecule. Ionized molecules may distort significantly and produce several other signals at various energies as symmetries are broken[21, 84]. Additionally, removal of an electron creates a positive charge around the atoms, which cause the nuclei to bind the electrons more tightly. This increases the transition energy from the core to valence orbitals, and leads to a net shift of absorption to higher energies, a blue shift. This effect can vary for different atoms in an ion, as the local charge may be distributed differently between the constituent atoms, and lone atomic ions feel this effect most strongly.

The main signature of a dissociating molecule is that features of the chemical products appear. If one of the products is an atom, sharp spectral features in Rydberg lines are common.

In order to access the time dynamics of these signals, slices at particular energies along the time axis are taken, called lineouts[85, 86]. To improve the signal-to-noise ratio, regions with the same signal are often integrated or averaged together[15, 86, 87]. Lifetimes of states are generally assumed to be first order and irreversible from one state to another. These are extracted by fitting to an exponential, $[S_2] = [S_1]_0 \times e^{-1/\tau \times t}$, where $[S_2]$ is the population of the second state, $[S_1]$ represents the population of the initial state, and τ is the lifetime of the initial state. This can be extended to 3 states as:

$$[S_3] = \frac{1/\tau_1 [S_1]_0}{1/\tau_2 - 1/\tau_1} \times (e^{-1/\tau_1 \times t} - e^{-1/\tau_2 \times t})$$

For each of these states, an appropriate ΔOD must be assigned, as it is possible that none of the states have an equivalent absorption to the ground state; although, in some cases, the final state is the ground state[88, 89].

A different type of signal is from molecular vibrations. The main feature of these signals is a repeated oscillation at a frequency given by the appropriate vibration. This can be made more sensitive by taking a lineout at the energy with the strongest signal and Fourier transforming it. If the vibration gets out of phase, the signals will become blurred along the time axis. An extreme case of this is often observed in an electronically excited state returning to the ground state with significant vibrational energy, a hot ground state. In it, the many positions away from equilibrium will be probed, which will have absorptions at slightly higher and lower energy than the cold ground state, and so a single peak in the static absorption will result in a positive-negative-positive ΔOD signal with the negative portion centered at the peak of the static absorption. This work will also show in chapter 3 that having differences in shape between the ground state and the core-excited state along the vibrational mode is paramount to observing a vibration signal with XTAS.

Lastly, there are short-lived signals that arise from interaction with the electric field of the pump. A common effect in strong-field experiments is a mixing of electronic states with dipoles along the electric field, referred to as the Stark effect[90]. As the states mix, they

split away from each other in energy. This results in a shift of the static absorption features, resulting in 2 part features, either positive-negative or negative-positive ΔOD features, depending on the direction of the shift. The mixing is not selective, so the direction of shifts will depend on the density of a given molecule's electronic states[18, 90]. The Stark effect only lasts the duration of the pump laser pulse and it often requires a strong electric field to have a strong signal. Another common effect is autoionization, where an atom absorbs an X-ray photon to excite into a Rydberg level, which can decay by a lower level filling the core-hole and the excited electron being ionized[18]. It can be disrupted by the visible pump pulse, which suppresses the absorption associated with autoionization, leading to a strong signal with few-fs duration. It is often using for finding temporal overlap of pump and probe pulses and determining the temporal resolving power of the experimental apparatus[60, 91].

There are as many other types of signals as there are processes, such as 4-wave mixing[18, 92] and many more, so this will not be a complete list, but it does highlight the main signals typically observed in XTAS and specifically observed this thesis.

Solid Signals

One of the main processes of interest in solids is the dynamics of the electrons after excitation. When a semi-conductor is excited with sufficient photon energy to exceed the band gap, electrons are moved from the valence band to the conduction band, creating an electron-hole pair. This electron-hole pair produces a signal similar to the state opening and state blocking in molecules, with a positive and negative feature, respectively. With sufficient energy resolution, the position of the electrons and holes in the band structure can be determined based on the positive and negative features[15, 26, 87, 93]. The amplitude of the signal and its decay can also show when the pair recombines and energy can no longer be harvested from the system[15, 87, 93].

Similar to the vibrational energy that can be made in excess in molecules, the absorbed photon energy in solids can be converted to movement of the lattice, vibrational energy. In some cases, particular phonon vibrations can be excited[94], but often the vibrations are incoherent and the observed X-ray signal consists of a broadened version of the static spectrum. In the ΔOD, these signals are characterized by a positive-negative-positive feature, centered on the broadened absorption peak[28, 87].

Additionally, the excitation into the conduction band can lead to changes in the lattice that lead to the band gap shrinking[28, 87]. The result of this is that the conduction band shifts to lower energies, red shifting the X-ray absorption similarly. This usually produces a positive-negative ΔOD signal, as the leading edge of the conduction band static absorption leads to more absorption at higher energies.

The XTAS technique is an extremely powerful tool in that it has the potential to observe any and all of these details. However, with great power comes great responsibility, and it is the duty of the researcher to carefully construct an experiment to differentiate these signals and to appropriately use analysis techniques to assign processes and quantify their dynamics.

1.4 Outlook

The work in this thesis details an apparatus for the measurement of few-femtosecond processes with X-ray Transient Absorption Spectroscopy in the soft X-ray and several experiments on both gases and solids. Chapter 2 details the parameters of the constructed apparatus as well as experimental conditions that were changed to optimize its functionality. In Chapter 3, studies on coherent vibrational superpositions show a method for the extraction of the core-excited potential energy surface, relative to a particular core-excited state. In Chapter 4, the dissociation of an ionized molecule is tracked in real time from its earliest distortion to final separation, including multiple intermediate states. Finally, Chapter 5 shows the results of measurements on solids in the soft X-ray, studying defects and recombination times in different materials.

Chapter 2

Experimental Apparatus

Some of the content and figures of this chapter are reprinted or adapted with permission from Lou Barreau, Andrew Ross, Samay Garg, Peter M. Kraus, Daniel M. Neumark Stephen R. Leone, "Efficient table-top dual-wavelength beamline for ultrafast transient absorption spectroscopy in the soft X-ray region". Sci Rep 10, 5773 (2020).

2.1 Design Goals

The study the dynamics of solids and molecules at the K- and L-edges of their constituent atoms required design and construction of a new experimental apparatus. The main requirement of such an apparatus would be to generate photons extending from the cutoff of high harmonic generation (HHG) sources driven by 800 nm wavelength source pulses, ∼120 eV[56, 57], up to and past the carbon K-edge, 285 eV. This will enable the study of several elements, including sulfur, chlorine, and carbon, which constitute several molecules and solids important in life and industry. To study these species with X-Ray Transient Absorption Spectroscopy (XTAS), the apparatus must generate these photons in sufficient proportions to have signal-to-noise ratio for useful scientific conclusions can be drawn. The photon flux at 300 eV in a 1% bandwidth that has been previously achievable in He is 1.6×10^5[95] and 1.8×10^5[63], which gives a target for the flux we aim to achieve. This flux must also be short in temporal duration in order to observe the fast transitions between states. Additionally, the probe photons must be able to be separated by energy to differentiate between the different states of interest. Previous systems in this energy range have shown to have resolution of ∼0.4 eV[21, 63, 95].

For the other pulse in the transient experiment, the pump laser pulse must be capable of inducing the fast processes of interest. For molecular vibrations, this requires that the pulse be shorter than half of a period of vibrations, which for something like CO_2 is half of 26 f[96]. For solids, the photon energy must be enough to excite the band gap in semiconductors; for example, molybdenum disulfide has an indirect band gap of 1.23 eV[97], and other semi-conductors may have a larger gap. For this reason, it is preferable to use a pump

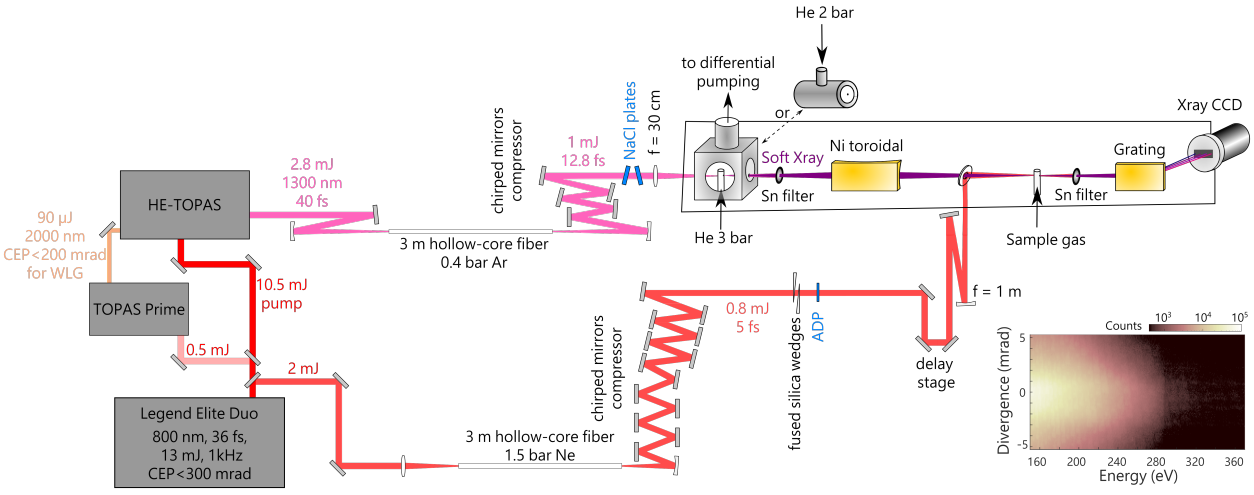

Figure 2.1: Summary of the beamline. Soft X-ray pulses are produced from high-order harmonic generation with few-cycle SWIR pulses in helium. Few-cycle pulses centered at 800 nm are simultaneously produced and are used as a pump in ultrafast transient absorption experiments. The different steps are detailed in the text. A typical X-ray camera image is shown at the bottom right. The drop in signal after ∼280 eV is due to carbon contamination of the X-ray optics, causing absorption at the carbon K-edge.

pulse centered at 800 nm and spectrally broadened to include lower wavelengths, down to 600 nm.

Finally, the apparatus must be able to run the experiment continuously over a long enough time to collect the statistics necessary to make scientifically accurate statements. The time required for XTAS is typically over several hours. This will require that HHG flux remains high over this time and that temporal drift between pump and probe can be minimized to maintain good resolution. Processes as short as 6 fs are the target of this apparatus, so temporal jitter or drift should be less than 6 fs. pulse-to-pulse instabilities in intensity of the laser pulses can introduce noise; although, each acquisition of the camera averages together 300-10,000 pulses. The desired level of pulse-to-pulse instability is on the order of $< 5\%$ for the X-ray flux and $< 2\%$ in the visible pump intensity.

2.2 General Layout

In general, the apparatus for an XTAS experiment consists of two sections. First, the preparation of visible and infrared pulses to the appropriate duration and intensity, and second, the propagation of the generated X-ray pulses. The preparation of pulses can be done in air and mostly consists of obtaining the appropriate spectral bandwidth with low dispersion. The propagation of X-rays must occur in a vacuum to prevent reabsorption of

X-rays[14]. The conversion between visible/IR to X-ray takes place in vacuum via HHG.

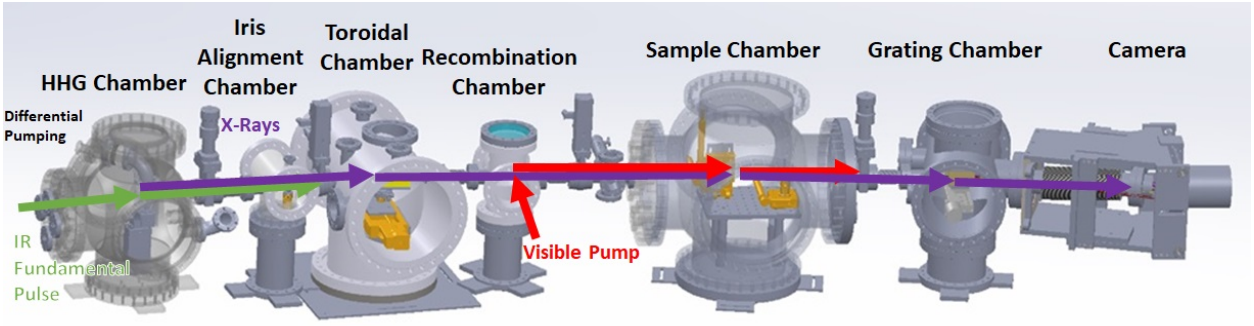

Figure 2.2: Design of the vacuum chambers for propagation of X-rays. X-rays are generated by HHG in the HHG chamber, using high pressures of He, which is reduced by differential pumping. The iris chamber allows ease of alignment of the fundamental laser. The X-rays are refocused by a toroidal mirror, through an annular mirror in the recombination chamber, where the visible pump is propagated collinearly onto the sample. The grating separates the X-rays in energy to be collected by the CCD camera. The visible and infrared pulses are absorbed by metal filters. Turbomolecular pumps are attached to the HHG, iris, sample, and grating chambers to pull vacuum.

The laser system begins with chirped pulse amplification of an 800 nm pulse, which is done by a Coherent Legend Elite Duo Ti:sapphire laser with carrier-envelope phase (CEP) stabilization. It can generate a 13 mJ, 30 fs, 800 nm pulse with a 1 kHz repetition rate. The pulse is split, and a portion is converted to 1300 nm by an optical parametric amplifier (OPA), which is spectrally broadened in a hollow core fiber (HCF) and compressed temporally by chirped mirrors. This drives the HHG process and produces soft X-Ray photons up to 370 eV. These are focused onto the sample and dispersed by a grating onto a CCD, which is collected and analyzed by code. The 800 nm pump is the other portion split off at the beginning, which is similarly spectrally broadened in a separate HCF and compressed with chirped mirrors. It is delayed by a variable stage and focused onto the sample. This layout is shown in Fig 2.1. The set of vacuum chambers that was designed for this apparatus is shown in Fig. 2.2.

Production of few-cycle short-wave infrared pulses

Few-cycle pulses centered at 1300 nm in the SWIR are produced using an OPA followed by spectral broadening in a hollow-core fiber filled with a rare gas [98] and compression with chirped mirrors [99]. An initial split of the 13 mJ pulse takes 11 mJ for the OPA and that is further split into 0.5 mJ and 10.5 mJ for use in a two-stage OPA, which converts 800 nm to SWIR (1300 nm). The two-stage system is obtained from Light Conversion and is

designed to provide CEP stability of the signal pulses. The first stage is a low energy OPA (TOPAS Prime), pumped by 0.5 mJ, which provides 90 μJ of 2 μm pulses in the idler. Due to the parametric amplification process, the idler pulses are passively CEP stabilized, with a stability of ¡200 mrad. They are then used as the seed for the white light generation (WLG) in a second, high energy, OPA (HE-TOPAS) pumped with the remaining 10.5 mJ of 800 nm light. This design should ensure the CEP stability of the signal pulses over the 1200-1600 nm tunable range of the OPA, regardless of the CEP stability of the pump laser. However, the following results are obtained with a CEP-averaged signal pulse.

The 2.8 mJ, 1300 nm, 40 fs output is focused with a 2-m focusing mirror to a focal size of 390 μm (at $1/e^2$) at the entrance of a 3-m-long, 700-μm-inner diameter stretched hollow-core fiber (HCF) filled with 0.4 bar of argon (Few-Cycle Inc.). The ratio of beam waist to fiber diameter was experimentally adjusted for best transmission through the fiber, and it was found that this slightly smaller value (0.56) compared to the optimal value for coupling to the LP_{01} mode[100] (0.64) yielded higher output power. After broadening through self-phase modulation, the spectrum extends from 1000 nm to 1500 nm (see the dashed line in Figure 2.3d), supporting 9.3 fs pulses with up to 1.45 mJ per pulse. After recollimation, the pulses are compressed with a set of four ultra-broadband dispersive mirrors (PC1816, Ultrafast Innovations GmbH) that provide an average of -150 fs^2 per reflection over the 1000-1700 nm spectral range. For fine-tuning of the group-delay dispersion (GDD), the beam goes through a pair of counter-rotating 2-mm thick NaCl windows, which have a GDD of +47.8 fs^2/mm at 1300 nm. Eventually, the NaCl windows were replaced with anti-reflection coated SF-11 wedges, which were less hygroscopic and had similar GDD of +76.7 fs^2/mm at 1300 nm. The pulses are characterized using a home-built dispersion-free second harmonic generation Frequency-Resolved Optical Gating (SHG-FROG), and the results are shown in Figure 2.3a-d. The retrieved pulse has a full width at half maximum (fwhm) in intensity of 12.8 fs, which corresponds to less than 3 optical cycles, with 80% of the energy in the main pulse. Further compression could be achieved with a better control over third-order dispersion.

The ultra-broadband dispersive mirrors are optimized for chirp compensation over a 700-nm bandwidth in the SWIR. In order to test the tunability of the HCF compressor, the central wavelength of the OPA is increased to 1400 nm, the rest of the system remaining identical. The spectrum is broadened in 0.6 bar of argon and extends from 1050 to 1600 nm (Figure 2.3h), with up to 1.15 mJ per pulse. From the SHG-FROG measurement and retrieval shown in Figure 2.3e-g, the pulses are compressed down to 9.6 fs fwhm, that is 2 cycles at 1400 nm, with 88% of the energy in the main pulse. Thus, we see that our system allows wavelength tuning in the SWIR over at least a 100 nm range.

Simultaneous production of few-cycle visible-near IR pulses

The 2 mJ pulses at 800 nm that are split before the pumping of the OPA stages (see Figure 2.1) are compressed to few-cycle duration using a similar method [98] in a second, 400-μm-inner diameter stretched HCF filled with 1.5 bar of neon. After propagation over two meters to compensate for the delay acquired by the SWIR pulse in the OPA stages,

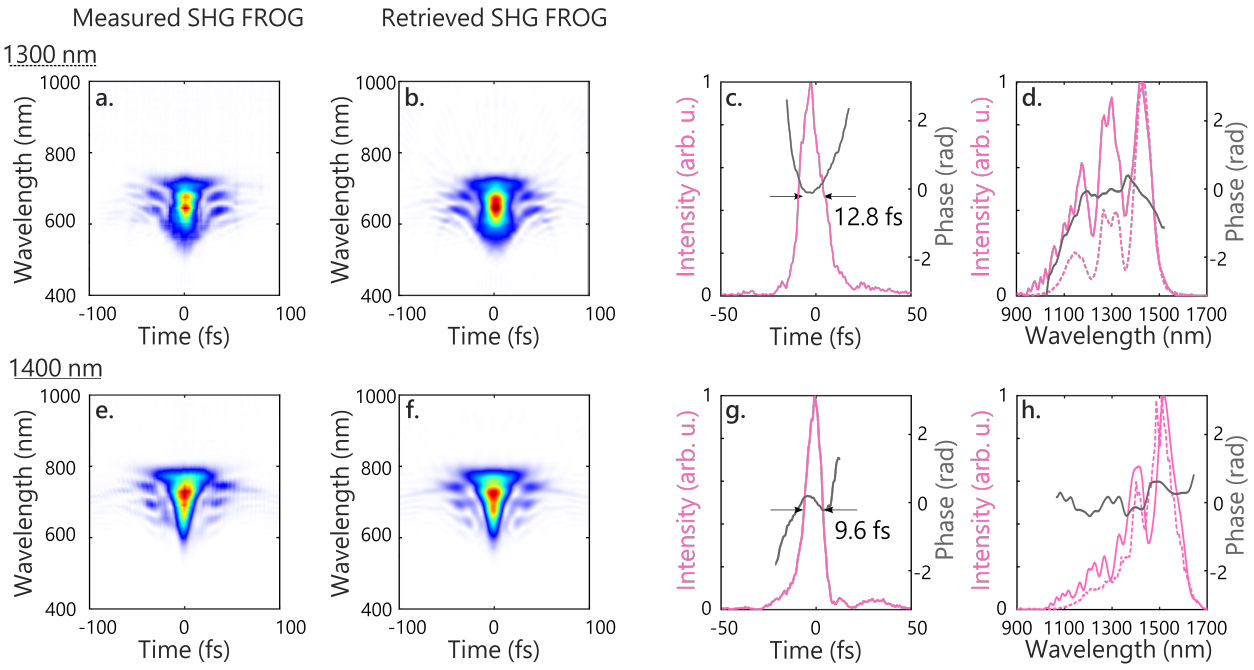

Figure 2.3: Characterization of the compressed SWIR pulses produced with the OPA central wavelength set at 1300 nm (**a-d**) and 1400 nm (**e-h**) with SHG-FROG. **a,e.** Measured spectrogram. **b,f.** Retrieved spectrogram. **c,g.** Retrieved temporal intensity (pink) and phase (grey). **d,h.** Retrieved spectral intensity (pink) and phase (grey). The dashed line is the spectrum at the output of the fiber as measured with a spectrometer (Ocean Optics FLAME). Phases are shown for intensities >5% of the maximum intensity.

the beam is focused with a 2-m focusing lens to a 280 μm spot size at the entrance to the fiber. At the output, the pulse energy is 0.8 mJ with a spectrum covering 550-950 nm (Figure 2.4c). Compression is achieved with reflections on sixteen ultra-broadband dispersive mirrors (PC1332, Ultrafast Innovations GmbH), transmission through fused silica wedges and finally through a 2-mm-thick Ammonium Dihydrogen Phosphate (ADP) crystal, which corrects for third-order dispersion [101]. The visible-near IR (vis-NIR) pulses are characterized with a d-scan module (Sphere Ultrafast Photonics) [102], whose results are shown in Figure 2.4. The d-scan phase retrieval algorithm indicates a pulse duration of 4.75 fs fwhm, which is 1.1 times the Fourier limit, with 75% of the intensity in the main pulse. Compression of the vis-NIR pulses to 1.8 cycle is realized at the same time as the compression of the SWIR pulses described in the previous section. Therefore, these two pulses can be used together in a pump-probe experiment. We note that shorter pulse durations in the vis-NIR with similar pulse energy can be achieved with this method [101], and could most likely be obtained here if the compression of the Ti:sapphire laser could be tuned independently for pumping the OPA stages and the vis-NIR HCF compressor. The intensity of the pump can be changed

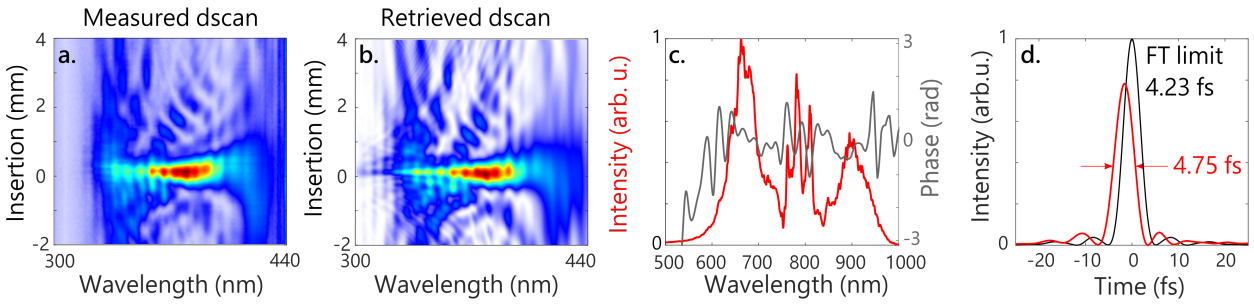

Figure 2.4: Characterization of the few-cycle 800 nm pulses used as a pump. **a.** Measured dscan. **b.** Retrieved dscan. **c.** Measured spectrum (red) and retrieved spectral phase (grey) of the compressed pulses. **d.** Retrieved temporal intensity (red) and Fourier-limited pulse (black).

programatically with a polarizer and rotating waveplate before the chirped mirrors.

The visible pump is delayed from the X-ray probe by a delay stage, which consists of two separate motorized stages. A long stage provides access to long delays. The long stage is a Newport UTM100PP.1, which has an accuracy of 1.5μm and a range of 100 mm. It allows for 10 fs steps with a total range of ∼600 ps; although, the usable range is limited by somewhat by imperfect retroreflection that moves spatial overlap of pump and probe pulses on the sample. Measurements up to 100 ps have shown repeatable signal. Mounted on top of the long stage is a smaller stage with better resolution, a Physik Instrumente P-611.1S, which has a 100 μm range and a precision of ∼2 nm. This small stage enables delay precision down to 13 as over a range of ∼600 fs. During a measurement, only one stage is moved at a time. When less than 600 fs are needed, the small stage is used while the long stage remains inactive to use the better resolution of the small stage.

Soft X-ray spectrometer

The soft X-ray (SXR) pulses are produced via the process of high-order harmonic generation by focusing 0.7 mJ of the few-cycle SWIR pulses with a f = 30 cm lens down to a 80 μm (at $1/e^2$) diameter focus (∼ 2 x 10^{15} W/cm^2) into a 4-mm-long gas cell continuously flowing with helium at a backing pressure of 2.8 bar (see Fig. 2.1). The use of a lens is unusual with few-cycle driving pulses[63, 95, 103–105]; however, the GDD near 0 of fused silica for 1300 nm (-2.4 fs^2/mm) provides minimal pulse lengthening from chirp and geometrical sources[106]. The gas cell is surrounded by a 7-cm-edge-length cube for differential pumping, sealed along the propagation axis with cellophane tape through which ∼1 mm holes are laser-drilled. The cube and the cell itself is evacuated by a roots blower with 900 m^3/h pumping speed, such that the pressure inside is calculated to be ∼ 1 Torr and is measured to be ∼ 1x10^{-3} Torr in the surrounding chamber. After HHG, the SWIR light is filtered out with a metallic foil

(Zr, Sn, Ag, Ti or Al can be used depending on the spectral region of interest). The SXR is focused by a Ni-coated toroidal mirror at 4° grazing angle into the sample, which can be a gas cell or a solid membrane. Changes between different samples can be easily achieved with motorized stages in the two dimensions perpendicular to the propagation axis. The spectrum is dispersed by an aberration-corrected concave grating and imaged onto an X-ray CCD camera (Greateyes, GE 2048 512 BI UV1). The camera is movable along the grating focal plane to fully capture the SXR spectrum. Depending on the spectral region of interest, two different gratings can be used, optimized for 5-25 nm (50-247 eV, Hitachi 001-0660) or 1-6 nm (207-1239 eV, Hitachi 001-0659), referred to as the low- and high-energy gratings in the following. The grating rotation and camera position can be adjusted to optimize the spectral resolution. The resolution of two gratings in the spectrometer has been determined using the Ar $2p_{3/2}^{-1}4s$ absorption line [107] to be 325 and 190 meV fwhm at 244.39 eV, corresponding to $\Delta E/E = 1.3$ x 10^{-3} and $\Delta E/E = 7.8$ x 10^{-4} for the low and high energy gratings, respectively. While the resolution of the high-energy grating is better, its increased groove density results in a lower efficiency by a factor of ~ 3. Unless otherwise mentioned, all the spectra shown in the following are measured using the low-energy grating.

Optimization of the photon flux at the carbon K-edge

2.3 Optimization of HHG Flux

Driving wavelength

Here we study how the high-harmonic flux in the cutoff region differs for two few-cycle driving pulses of different wavelengths in the SWIR. Indeed, at the single-atom level, the HHG efficiency scales with λ^{-6} (refs. [59, 108]). However, this goes together with an increase in the cutoff photon energy as λ^2 (ref. [109]), and calculations have shown that the atomic response can be macroscopically overcome under certain phase-matching conditions [110]. In the previous section, the tunability of the few-cycle SWIR source was demonstrated. We therefore compare the SXR spectra produced when driving the HHG in the 4 mm gas cell with the 1300 nm and 1400 nm pulses characterized in Figure 2.3. The HHG spectra produced in these conditions are shown in Figure 2.5a. From the measured spectra, the photon fluxes are calculated at the source using the known quantum efficiency of the CCD camera and number of electrons generated per X-ray photon of a given energy, as well as tabulated toroidal mirror reflectivity, metallic filter transmission, and grating efficiency. At both wavelengths, the spectra are continuous and extend from below 150 eV (not shown in Figure 2.5 because of the limited size of the camera chip) to above 300 eV. As expected, the maximum photon energy produced with few-cycle pulses centered at 1400 nm is higher compared to 1300 nm. The photon flux is 2 to 10 times larger at the 1300 nm driving wavelength over the 150-280 eV spectral range. However, in the carbon K-edge region above 280 eV, the two drivers produce similar high harmonic fluxes. The measured photon fluxes, in

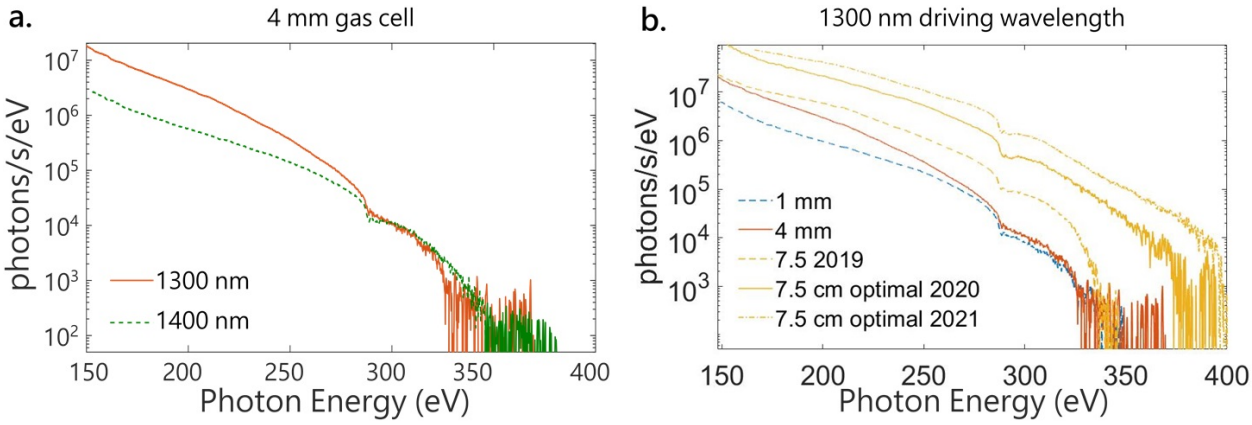

Figure 2.5: Optimization of the flux at 300 eV with the driving wavelength and the gas cell length. **a.** Soft X-ray high-order harmonic spectra generated in helium with few-cycles pulses with the OPA central wavelength set at 1300 nm (red, solid) and 1400 nm (green, dashed) in a 4 mm gas cell. **b.** Soft X-ray high-order harmonic spectra generated in helium with few-cycles pulses with the OPA central wavelength set at 1300 nm in 1 mm (blue, dotted), 4 mm (red, solid) and 7.5 cm (yellow, dashed) length gas cells. These first 3 were taken on subsequent days for better comparison. Further optimization of the SWIR HCF gas pressure for HHG with the 7.5 cm cell yields the solid yellow curve (optimal from 2020) and the dotted-dashed yellow curve (optimal from 2021).

photons/s in 1% and 10% bandwidth at 300 eV, are summarized in Table 2.1 and compared to literature values for SXR HHG sources driven by few-cycle SWIR pulses.

HHG gas cell length

The question of macroscopic effects in HHG with SWIR pulses has been the subject of recent experimental and theoretical work [95, 110–112]. Here we compare the SXR flux obtained in helium with few-cycle 1300 nm pulses in continuously flowed gas cells of different lengths. The spectrum obtained in a 4 mm gas cell described previously is reproduced in red, solid in Figure 2.5b. Johnson *et al.* showed that, in the so-called overdriven regime, plasma defocusing effects strongly reshape the HHG driving pulse, already in the tails of the pressure distribution around the gas cell [63]. In order to limit these effects, a shorter gas cell of 1 mm length (1 mm outer diameter and 500 μm inner diameter) is used in place of the 4 mm one described before. The corresponding HHG spectrum, generated in 4 bar of helium, is shown in blue on Figure 2.5b. No increase of the cutoff is observed, and the flux at 300 eV is 2x less than with a longer interaction medium (Table 2.1).

Since the absorption length at 300 eV of 2 bar of helium is $\sim$1 cm, a longer HHG medium was also tried[113]. SXR pulses are generated in a 7.5 cm long tube, sealed at the entrance

Condition	Photons/s in 1% BW at 300 eV	Photons/s in 10% BW at 300 eV	Photons/s in 1% BW at 200 eV
1400 nm, 4 mm cell	$3.4\text{x}10^4$	$3.3\text{x}10^5$	$1.18\text{x}10^6$
1300 nm, 4 mm cell	$3.4\text{x}10^4$	$3.6\text{x}10^5$	$6.4\text{x}10^6$
1300 nm, 1 mm cell	$2.5\text{x}10^4$	$2.7\text{x}10^5$	$2.0\text{x}10^6$
1300 nm, semi-infinite 7.5 cm cell (2019)	$2.5\text{x}10^5$	$2.4\text{x}10^6$	$1.2\text{x}10^7$
1300 nm, semi-infinite, optimal 2020	$1.4\text{x}10^6$	$1.3\text{x}10^7$	$4.5\text{x}10^7$
1300 nm, semi-infinite, optimal 2021	$4.1\text{x}10^6$	$3.9\text{x}10^7$	$8.2\text{x}10^8$
1850 nm, 12 fs in Ne[95]		$2.8\pm0.1\text{x}10^7$	
1850 nm, 12 fs in He[95]		$1.8\pm0.1\text{x}10^6$	
1800 nm, 12 fs in Ne[63]	$3.0\pm0.8\text{x}10^6$		
1800 nm, 12 fs in He[63]	$1.6\pm0.4\text{x}10^5$		

Table 2.1: Comparison of photon fluxes in the soft X-ray in existing beamlines using HHG driven by few-cycle SWIR pulses.

with a 500 μm thick window and with a teflon foil through which a hole is produced with the laser at the end. The focus of the SWIR is towards the exit of the cell, therefore being qualified as semi-infinite [114, 115]. No nonlinear effects in the entrance window were observed at the working intensities. A reduced ~ 2 bar helium pressure is required to optimize HHG in the semi-infinite gas cell, so differential pumping is not necessary. Instead, the roots blower pump is used to back the turbomolecular pump attached to the HHG chamber, where the pressure is measured to be $\sim 10^{-3}$ Torr in these conditions. As shown in dashed yellow in Figure 2.5b, this gas cell produces an order of magnitude more photon flux at 300 eV, with the maximum achievable photon energy remaining identical. Therefore, the semi-infinite gas cell is used in the following experiments. Following this observation, the other experimental parameters were optimized to maximize the SXR flux. Broadening the SWIR pulse in 0.7 bar of argon, instead of 0.4 bar previously, produces the solid yellow spectrum visible on Fig. 2.5b, with 1.4 x 10^6 photons/s in 1% bandwidth at 300 eV. Further improvements in the coupling into the HCF and improvements to the compression of pulses before the HCF produces the dashed-dotted yellow spectrum, with 4.1 x 10^6 photons/s in 1% bandwidth at 300 eV (see table 2.1).

We note that continuous SXR spectra are obtained in all the reported cases, but this observation is not proof of the production of isolated attosecond pulses - these spectra are measured with random CEP and the lack of CEP stability can cause random phase shifts in the HHG spectra that then appear as a continuum [116]. The semi-infinite gas cell yields more photon flux around the carbon K-edge, but is probably less suited for the production of isolated attosecond pulses. However, few-fs SXR pulses at the carbon K-edge (combined with a few-fs pump) would be able to probe ultrafast dynamics on the few tens of femtoseconds timescale, such as passage through conical intersections in organic molecules. Temporal characterization of the SXR pulses [105, 117] was not attempted. However, the temporal resolution of the beamline is estimated from a transient absorption experiment in the fol-

lowing section. It is limited by the durations of the vis-NIR pulse (see Fig. 2.4), the SXR probe, and the optical path fluctuation of the ∼15 m long interferometer. The delay jitter has been measured using a balanced optical cross-correlator [118] to be 2 fs rms over 10 s.

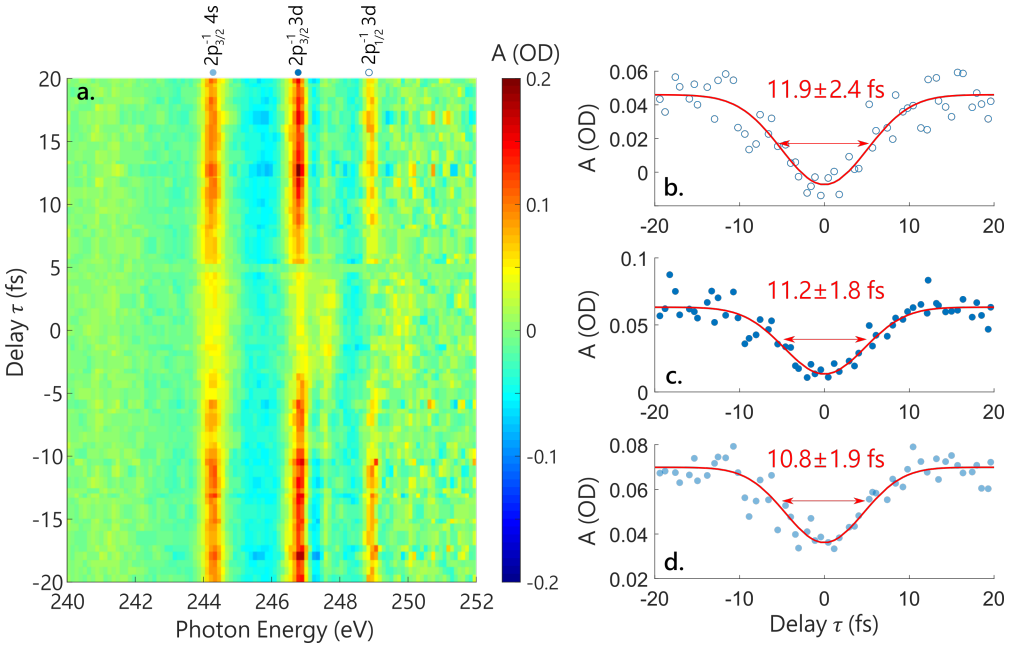

Figure 2.6: Transient absorption spectroscopy in the vincinity of the Ar $L_{2,3}$ edge with sub-5 fs vis-NIR pulses. **a.** Soft X-ray absorption spectra of argon as a function of the delay between the SXR and vis-NIR pulses. Negative delay values correspond to the SXR arriving first. At each time step the spectrum is acquired during a period of 15 s, for a total measurement time of 38 min. **b-d.** Lineouts of (a) at the $2p_{1/2}^{-1}$ 3d energy (b), $2p_{3/2}^{-1}$ 3d energy (c) and $2p_{3/2}^{-1}$ 4s energy (d). The blue dots are the experimental data and the red line is a Gaussian fit, whose full width at half-maximum duration is indicated.

Determination of Instrument Response function by Ar at the $L_{2,3}$-edge

In order to realize pump-probe experiments, the sub-5 fs vis-NIR pulse is time-delayed and focused into the sample gas cell with a concave mirror and recombined with the SXR on a hole mirror (see Fig. 2.1). The optical light is filtered by a metallic foil before the SXR spectrometer. A representative transient absorption experiment is performed in argon, using SXR produced with the 7.5 cm long HHG gas cell filled with 2 bar of helium. The delay-dependent absorption spectra are shown in Figure 2.6a. At each delay point τ, the absorbance

A is calculated as $A(\tau) = -\log_{10} \frac{I(\tau)}{I_0(\tau)}$, where the reference spectrum I_0 is reconstructed by using a Fourier low-pass filter directly on the measured signal $I(\tau)$. This procedure allows for removal of the intensity fluctuations of the SXR spectra and is well-suited in the case of narrow absorption lines [93]. In Fig. 2.6a, A then represents the absorption with respect to the continuum absorption background. Here, the SXR excites 2p core-excited states of argon. In the presence of the vis-NIR pulse, with a polarization parallel to the SXR polarization and intensity of ~ 3 x 10^{13} W/cm^2, the absorption lines are ac Stark-shifted. This corresponds to a decrease in absorbance at the position of the static lineshape. The spectral resolution (325 meV at this energy, see previous section) prevents the observation of hyperbolic sidebands and the direct measurement of the temporal decay of these states[119, 120]. However, the delay dependence of the pump-induced bleach of the absorption line can give an upper bound of the temporal resolution of our experiment. The changes in absorbance as a function of the SXR-NIR delay for the $2p_{1/2}^{-1}$ 3d, $2p_{3/2}^{-1}$ 3d and $2p_{3/2}^{-1}$ 4s states are shown in Figure 2.6b-d, respectively. For these three states, the changes can be fit with a Gaussian function of $\sim$ 11 fs fwhm. We note that in a similar experiment employing SXR and two-cycle 1700 nm pulses, Chew *et al.* observed sub-cycle oscillations that were attributed to a signature of tunnel ionization[121]. Due to averaging of the CEP, these oscillations are not resolved in our experiments. It would be interesting to study such tunnel ionizations in the future, as the calculated Keldysh parameter in our experiment is also in the tunneling regime but different than at 1700 nm.

2.4 Determination and correction of time zero drift with balanced optical cross-correlator

Over several hours, the relative path lengths can change between the pump and probe arms. This is a common problem in transient absorption experiments and leads to time smearing, where delays from one pulse are binned with delays with an offset from other iterations, which leads to loss of temporal resolution. Time smearing becomes more of a problem with longer pump and probe arms, as each reflection and optic can vibrate or expand to create small differences that compound into large time changes. This can happen on roughly two scales: shorter than 1 second, the acquisition time of a single time step, and over several minutes or hours, between separate iterations of a full scan. In order to observe and correct these issues, a way to accurately determine the relative delay between pump and probe on a pulse-to-pulse basis is necessary.

For this purpose, a balanced optical cross-correlator (BOC) is constructed and installed. These devices are commonly used in pulse synthesis, where they have been shown to keep separate 2 color laser pulses at the same relative delay to within 30 as[122]. The structure is shown in Fig 2.7, where 1300 nm and 800 nm are combined on a dichroic mirror and propagated collinearly. The two pulses are split by a beam splitter. One side is transmitted through glass, which delays one of the beam colors more than the other, as the refractive

index of 800 nm is slightly larger than of 1300 nm cite. This results in one of the arms with the visible leading and the other with the IR leading. Both beams are focused into a BBO crystal, which allows sum frequency generation the beams overlapped in time and space with total intensity proportional to the amount of overlap. The sum frequency generation intensity is measured by a photodiode.

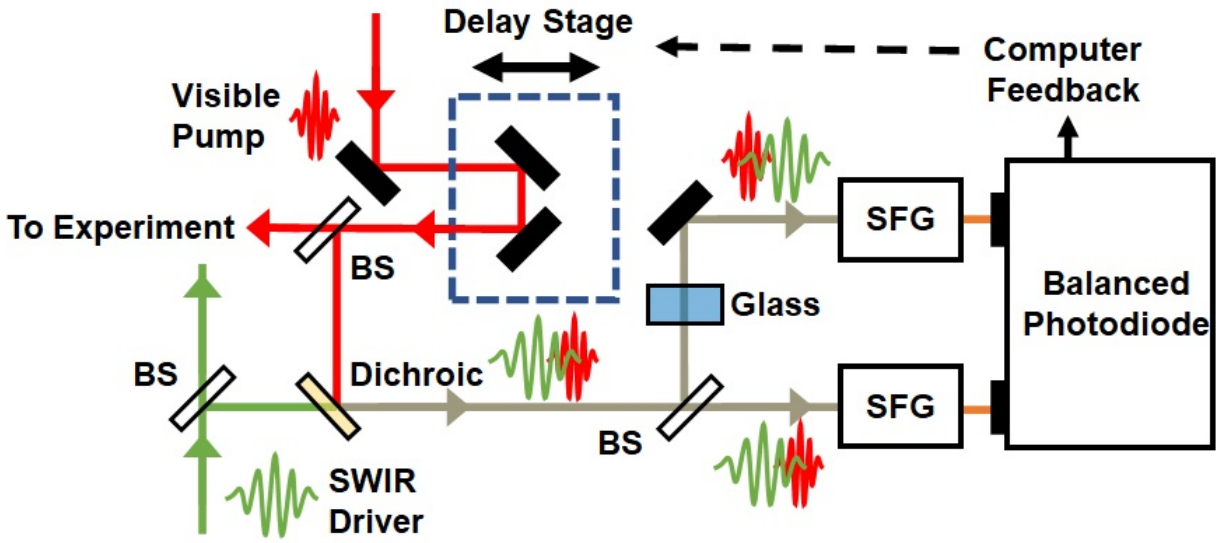

Figure 2.7: General layout of a balanced optical cross-correlator (BOC). The acronyms used are: BS = Beam Splitter, SFG = Sum Frequency Generation, Dichroic = Dichroic Mirror. Visible pump and SWIR driver for HHG are propagated collinearly with the visible leading. That beam is split by a half-silvered mirror and one side propagated through glass, which has a larger index of refraction for the visible, delaying it. Both beams undergo sum frequency generation, and their relative intensities are compared by a balanced photodiode. The computer can feedback to the delay stage to keep both intensities equal and time zero constant. Relative delays between 2 color pulses have been accurately determined to within 1 fs[122].

By taking the difference of the photodiode signal of the two arms, the difference between the initial delay of the two pulses relative to an internal time zero is determined. The internal time zero is the case in which one arm has 800 nm leading 1300 nm by the same amount that the latter leads the former in the other arm, which results in equal photodiode signals and a difference of zero. As the delay on the visible input pulse is lengthened, the first arm becomes more intense while the other becomes less intense, which is clear from the difference. This results in a region of delays where the difference voltage is linear with respect to the visible delay, which corresponds to the region where the pulses remain partially overlapped in time and generating SFG. To calibrate the BOC, the visible input delay is scanned and

the difference recorded; the difference voltage vs input delay in the linear region is fitted to a linear curve. From this, the relative delay of pump and probe can be measured for each pulse.

Short time fluctuations

The fluctuations that occur during a single acquisition were measured by acquiring BOC values for 10 s, or 10,000 pulses at 1 kHz. Initially, fluctuations of 2.3 fs standard of deviation over that 10 s were typical of the system.

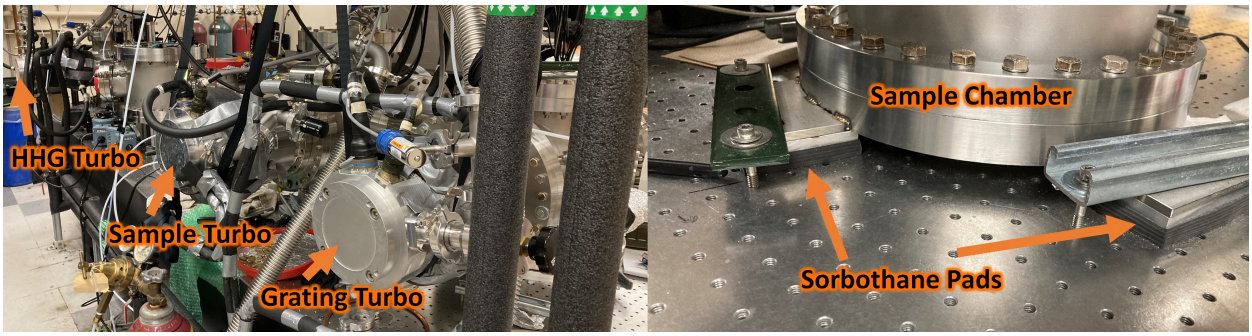

Figure 2.8: Photographs of the turbomolecular pumps, which introduced significant timing jitter are shown on the left. The simple solution of a rubber pad underneath the vacuum chambers is shown on the right.

In order to determine the source of these fluctuations, a frequency analysis of the BOC was carried out. The time zeros were Fourier transformed, which showed large peaks at several different frequencies. Working on the hypothesis that these were being driven by the vacuum pumps necessary to the experiment, a series of measurements were taken by turning off each individual pump, the results of which are shown in fig 2.9. Random changes in low frequency noise can lead to measurements with fewer pumps on having larger standard of deviations, but the disappearance of particular Fourier peaks was consistent in turning off particular pumps. The large roots blower roughing pump was responsible for a sharp 60 Hz peak. Various turbo pumps' controllers were found to be responsible for several broad vibrations with the largest pumps, a Shimadzu 1303 (sample turbo) and 1003 (HHG turbo), causing the largest problems, which are shown in fig. 2.8. With all pumps off, the standard of deviation was 1.2 fs jitter at best.

Reduction of fast jitter by pump isolation

In order to reduce noise most effectively, steps were taken to isolate the vacuum pumps from the table. First, a bucket was secured around the foreline to the roots blower near the pump, and sand was added, which reduced vibrations slightly, but not entirely. Additionally,

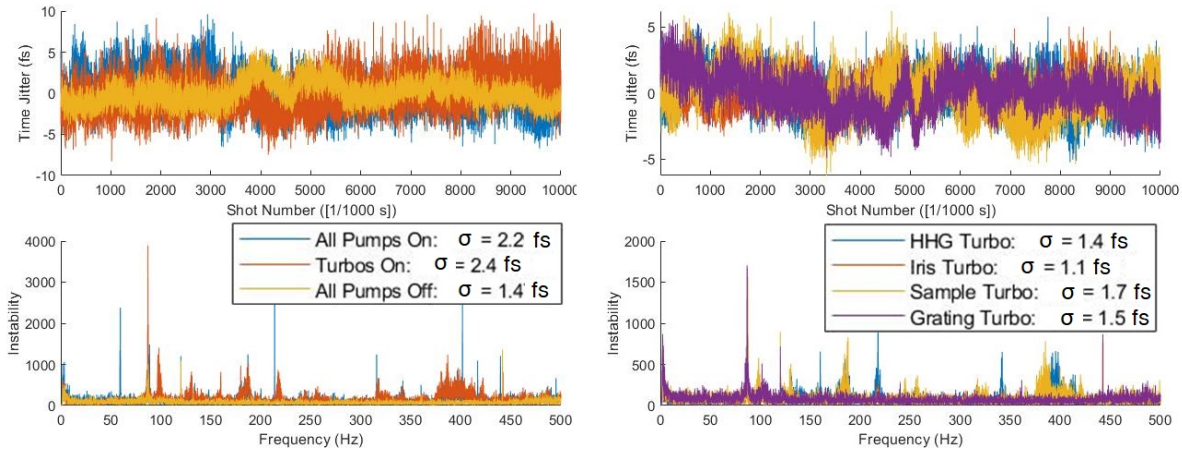

Figure 2.9: Time zero instability measurements in the initial experiment. The left shows progression from all pumps on to all pumps off. The right shows measurements where the only pump on is the controller of particular turbo pumps (no turbos are spinning). Standard of deviations for a measurement are shown in the legend in femtoseconds.

another bag of sand and loose packing material was secured around the flexible portion of the vacuum foreline, and it was secured to overhead struts with ratcheting tie down straps. This effectively eliminated the 60 Hz noise.

To separate the turbo pumps from the table, blocks of rubber were added under the vacuum chamber feet. Specifically, 1/4" thick, hardness 70 durometer sorbothane from Thorlabs was cut into 3" x 4" sections, the size of the chamber feet, and each chamber used 3-4 sections. The chambers were secured to the table by a bar with bolts screwed into the table, despite worries that this would transfer vibrations through the bolts. This solution is shown in fig. 2.8. Securing the chambers had the additional effect of compressing the sorbothane, so that no settling or chamber movement was observed after months. Taking BOC measurements showed that the frequencies associated with turbo pumps were eliminated, and that very little difference was observed between the pumps being on or off, shown in fig 2.10.

In the course of these investigations, another source of noise was found to be an intermittent white noise from the floating table. This caused large positive spikes in time zero, shown in fig 2.10. It would disappear for days at a time and was not constantly present on days when it was. The exact cause was never determined; although, it may be from the building air compressor. Turning the air supply off and not floating the table was found to eliminate this. The best noise levels were observed with a floating table, which was a standard of deviation of 0.69 fs over 10 s, most of which was low frequency noise. This is within the period of an 800 nm electric field change, which means that the system is stable enough to measure the short time scales desired.

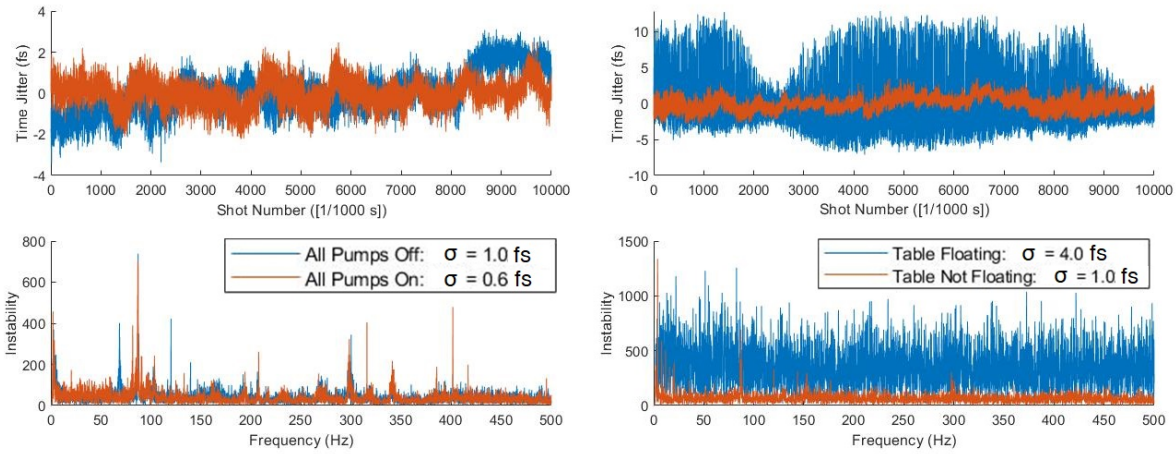

Figure 2.10: The left shows time zero instabilities measured with all vacuum pumps on compared to off. No frequencies are observed associated with the pumps, showing the efficacy of the sorbothane. The right shows large fluctuations associated with the floating the table, which appears as white noise.

In all measurements, an instability with a broad frequency of 87 Hz was found to persist. This frequency could be exasperated by jumping on the ground hard, which suggests that it is not coming from a pump, but the source of this frequency has not yet been identified.

Correction of long time drift

The drift in time zero was also measured over several hours. Changes of up to 40 fs were observed with up to 20 fs in one hour, shown in fig 2.11. The largest changes were observed around 1:00 PM with the quietest time around 5:00 PM. The large changes did not seem to be correlated with class changes from undergraduates by comparing days with and without classes.

Corrections to the long drift were undertaken by programming a feedback system. The program finds time zero on the BOC when the XTAS experiment begins, which it defines as the original time zero. Then, on subsequent iterations of the full delay, time zero is re-found on the BOC and the difference from the original is subtracted from the delay points to be scanned by the delay stage. Thus, it supplies a correction that keeps the pump and probe relative delay on the sample consistent to within 6 fs with an average of $\sim$3 fs over scans lasting up to 10 hours.

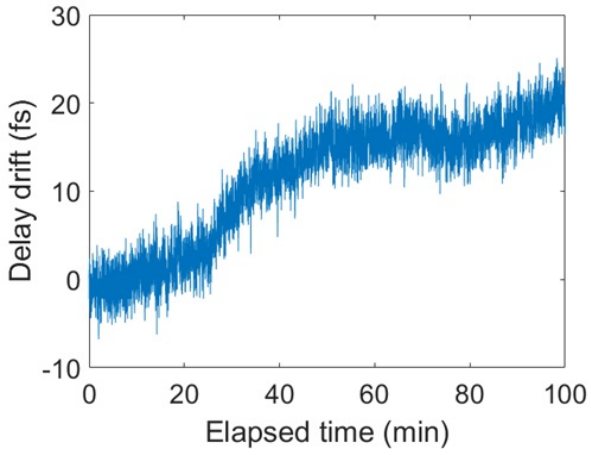

Figure 2.11: Time zero instability measured over an hour, showing drifts up to 20 fs. Longer measurements showed drifts up to 40 fs.

2.5 Data Acquisition

For experiments, data is acquired by central control of several Labview programs, written primarily by Samay Garg and myself. The program controls the pump shutter state, gas cell position, delay stage, and camera acquisition. XTAS measurements are run in a pump-on, pump-off configuration, where the unabsorbed flux is not measured on each cycle, and ΔOD is calculated as:

$$\Delta OD = -\log_{10}\left(\frac{I_{on}}{I_{off}}\right)$$

The CCD camera is cooled to -30° C to reduce dark counts. Typical camera acquisitions are 300 ms - 10,000 ms, depending on the absorption of the sample and the X-ray flux. At 1 kHz, this corresponds to averaging of 300 - 10,000 individual pulses. During acquisition of a transient measurement, the shortest step sizes used are 1 fs and longer step sizes are often used, depending on the time range of the dynamics of interest. A typical transient experiment contains $\sim$80 time steps, which generally produces a sufficient signal-to-noise ratio for quantitative measurements in $\sim$4 hours. Measurements that require more time steps are averaged for longer. The longest an experiment has been run is 10 hours. During that time, the BOC kept the temporal overlap between pump and probe pulses. In order to ensure that measurements are repeatable, they are repeated at least 2-3 times, usually with slightly different parameters, such as pump intensity or time step size.

2.6 Summary

An instrument capable of performing X-ray Transient Absorption Spectroscopy is constructed. Compression of pulses is achieved down to 12.8 fs for 1300 nm, 9.8 fs for 1400 nm, and 4.75 fs for 800 nm. Different parameters for maximum flux were tested, and it was found that the longest (semi-infinite) HHG gas cell performed the best, generating an order of magnitude more flux than the thinnest (1 mm). It was also found that the 1300 nm fundamental generated slightly more flux overall than 1400 nm fundamental; although, this may have been due to limitations of the tunability of equipment. A final optimal flux of 4.1×10^6 photons/(s*1% BW) at 300 eV is reached. A cross-correlation of 11 fs is achieved. Finally, a balanced optical cross-correlator was built that enabled determination of time jitter between pump and probe pulses and enabled reduction of jitter by finding erroneous vibrations. A final timing jitter of 1.0 fs was measured over 10 s.

Chapter 3

Core-excited state slopes probed by real-time tracking of molecular vibrations

3.1 Introduction

Upon excitation with photons in the X-ray regime, molecules enter a core-hole excited state, which can have a vastly different potential energy surface, compared to the ground state[123–127]. That newly formed core-excited potential energy surface (CEPES) can drive nuclear motion in the ultrashort lifetime of the core-hole, as long as a few femtoseconds[128–130]. Several other X-ray photon techniques depend strongly on the core-excited state, such as Resonant Inelastic X-ray Scattering and Resonant Photoemission[123, 125, 127]. In general, the potential surface dictates the ultrafast dynamics that occur during the core-hole lifetime. In molecules, vibrational modes can be excited from the core-excited state if the CEPES differs from the ground state PES in its slope along vibrational modes, which makes the X-ray absorption spectrum influenced by multiple vibronic transitions and makes extraction of the CEPES difficult[131, 132]. The theoretical ability to predict the CEPES can vary based on the exact implementation of Density Functional Theory[124, 133], and thus experimental measurement can help to provide values for comparison and highlight strengths and weaknesses in different theoretical methods.

In order to measure the CEPES accurately, a technique must be used that goes beyond static absorption measurements, as static absorption will probe only the ground state wavepacket of the equilibrium geometry. Instead, a transient technique is required, such as XTAS. In this experiment, the sample is first excited to a superposition of vibrational states by Impulsive Stimulated Raman Scattering (ISRS), driven by the short 800 nm pump. This launches a wave packet along the Raman active vibrational modes[134, 135]. Specifically, it activates the Raman modes that have a period more than double the duration of the laser pulse[134, 135]. As the molecule vibrates, the absorption to the CEPES is tracked by the

soft X-ray probe at a series of delay times from the initial excitation, resulting in different absorption energies from the vibrating nuclear positions.

$$E_{photon}(q) = PES_{core-excited}(q) - PES_{ground}(q)$$

where E is the energy of the absorbed photon and q is the set of nuclear positions along a vibrational mode, which is shown in figure 3.1[125, 126, 136]. In the case of a symmetric stretch, all bond distances change by the same amount as q changes. The bond distance can serve as a measure of q in this case, and it is used where appropriate in this chapter. Otherwise, q will be scaled to a convenient unit distance. The ground state potential energy surface is easily calculated or derived from experimental Raman data and the energy of the photon is measured by this experiment to extract information about the CEPES.

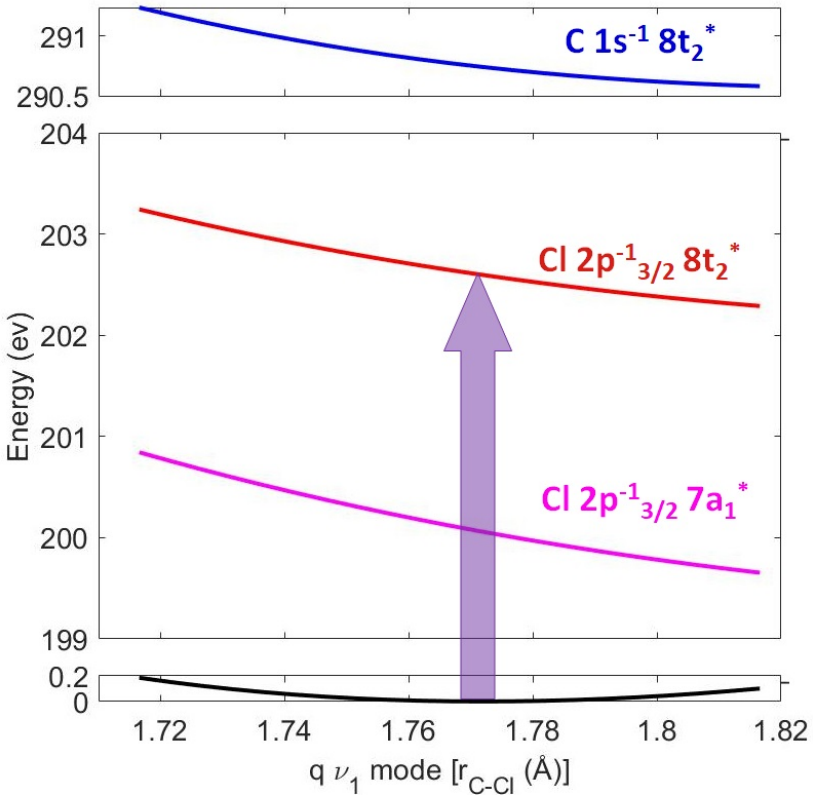

Figure 3.1: An example of the transitions involved in vibrations is shown for the CCl_4 symmetric vibration. The scale of the energy spacing is the same for each of the 3 regions. The experimentally measured energy is: $E_{photon}(q) = PES_{core-excited}(q) - PES_{ground}(q)$. For the symmetric stretch, q can be defined in terms of the bond lengths, as all lengths remain identical.

With a calculated ground state potential, the vibrational wave packet, defining the average nuclear positions and their spread, can be simulated by solving the time-dependent

Schrodinger equation: $\hat{H} = \hat{T} + \hat{V} - \mu\hat{F} - \alpha\hat{F}^2 - i\hat{W}$ where $\hat{H}$ is the Hamiltonian, $\hat{T}$ is the kinetic energy, $\hat{V}$ is the calculated potential, $\hat{F}$ is the electric field from the laser pulse, μ is the dipole, α is the polarizability as a function of distance along the vibration coordinate, and $\hat{W}$ is the negative imaginary potential, which is used in numerical solutions to prevent issues at the edge of the grid for simulations[137–139]. The dipole of the molecules studied in this thesis is initially close to 0, but can become significant from the polarizability in the intense laser electric field, which induces movement of the wavepacket, which continues as a vibration after the laser pulse ends. This equation can be solved numerically by a program run in Matlab: https://sourceforge.net/p/wavepacket/wiki/Home/ [137–139]. The results of these simulations show that despite the wave packet consisting of a superposition of a potentially large number of vibrational levels, the overall shape of the wave packet remains similar to the ground state wave packet, which suggests that the spread and shape of the X-ray absorption will be similar to the ground state as well. Additionally, it shows agreement with the classical derivation of ISRS, which suggests that the maximum excursion along the vibrational cooridinate will be proportional to the intensity of the laser pulse, or the pump power[140], which gives a way to determine if the experiment is behaving as expected and better define the CEPES.

Because the molecular vibration by definition repeats, the information on the CEPES is accessed multiple times as time progresses in the measurement of XTAS. The repetition at regular intervals allows enhanced detection of the vibrational frequencies and other noise to be more easily discarded. It also allows multiple frequencies to be distinguished if they are present[141].

3.2 Code Development

Due to the nature of measuring vibrations, the transient absorption data has correlations between energy that provide overlapping information, which can lead to much stronger signals if properly accounted for. For example, the vibration leads to a net shift of the energy of a state absorption, which leads to a positive ΔOD on one side of the energies and a negative ΔOD on the other, an example of which is shown in fig 3.2. Simply adding these two signals together or taking a line out along one of the energies ignores large pieces of this information. However, there is no existing analysis code that can take advantage of the additional information, so code must be developed, according to a model, expressly for this purpose. Applying a model of a shifted static spectrum can allow extraction of the exact energy changes in a more consistent manner. Another consideration that must be taken into account is that at the intensities used in these experiments to excite the vibrations, the molecular samples can also be ionized, and any model used will also need to take these new absorptions from the ionized molecule and its derivatives into account.

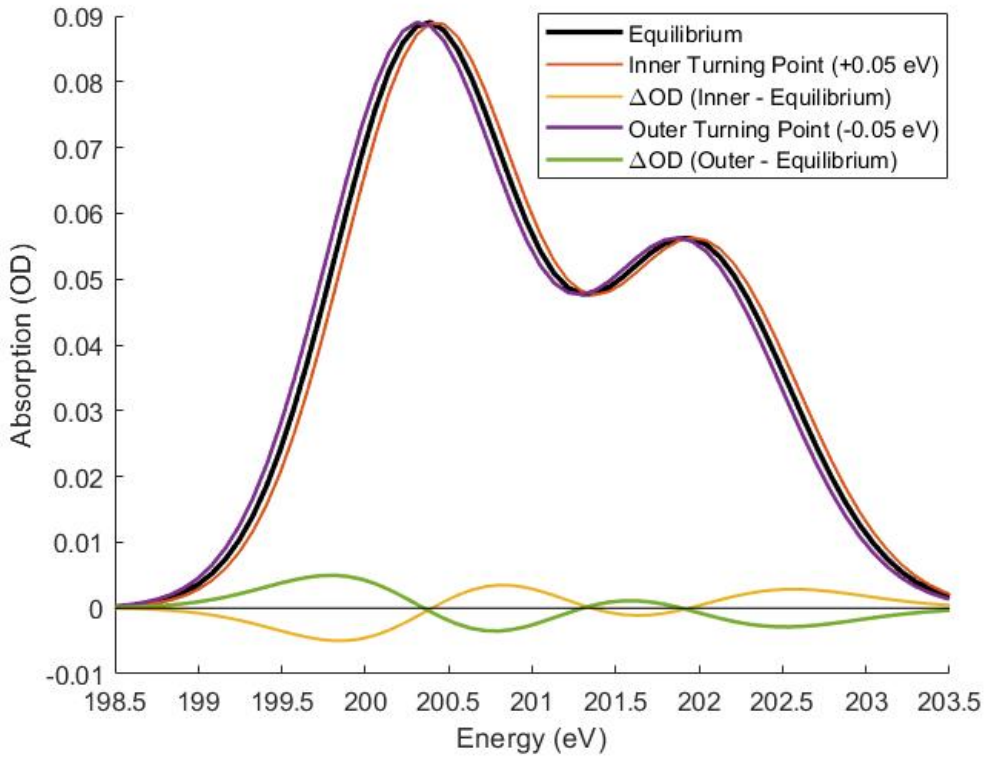

Figure 3.2: An example of the types of data that result from vibration is shown for the Cl $2p^{-1}$ $7a_1^*$ of CCl_4. The shift of ± 0.05 eV corresponds to roughly 0.005 Å of movement along the symmetric stretch. Notice that the ΔOD signals are strongest where the slope of the static absorption is the largest, and the ΔOD is smallest where the peaks are centered.

Noise Reduction by Fourier Filtering

The data is filtered and large amounts of correlated noise are removed using the edge referencing algorithm discussed previously[76]. However for vibration data, where each time step must have minimal noise in order not to introduce new frequencies, elimination of noise from changes in X-ray harmonic intensity is paramount. In the normal algorithm for ΔOD, a spectrum with a pump on is compared to a pump off, $\Delta OD = -\log_{10}(I_{on}/I_{off})$, so camera integrations of X-ray pulses where there is a net change in the X-ray flux between on and off can result in net changes of positive or negative ΔOD, which adds noise between each time point, affecting Fourier space. Edge referencing removes a lot of this noise, but at higher energies these intensity fluctuations are much stronger and require additional filtering.

A way to achieve more complete removal of X-ray harmonic intensity fluctuation is to remove comparison of 2 different X-ray shots, such that only the pump on spectra are used for calculating the ΔOD. This can be achieved by using the Fourier filtering tech-

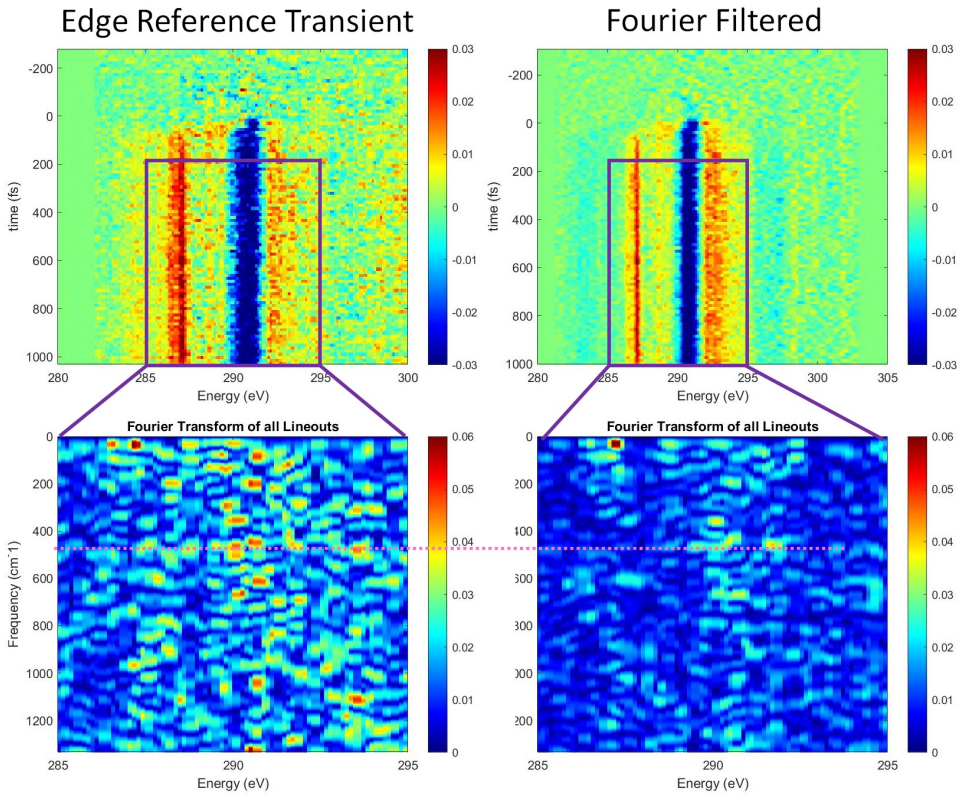

Figure 3.3: The results of noise filtering by edge referencing and Fourier filtering are compared. The symmetric vibration frequency is clear only for the Fourier filtered spectrum. Note again that the Fourier filtering applies only on the spectral axis; improvements in the Fourier transform of the temporal axis are only due to reduction of noise.

nique developed by Christian Ott[93]. At each delay point τ, the absorbance OD is calculated as $OD(\tau) = -\log_{10}\frac{I(\tau)}{I_0} - -\log_{10}\frac{I_{low-frequency}(\tau)}{I_0}$, where the low frequency spectrum, $I_{low-frequency}$ is reconstructed by using a Fourier low-pass filter along the energy axis directly on the measured pump on signal $I(\tau)$, and the pump off X-ray data is not used. The reference spectrum, I_0 cancels out, so it is largely irrelevant, but it must be chosen so that it does not contain negative absorptions, as this will affect the filtering in the Fourier domain. Typically, I_0 is just an experimental spectrum with no gas absorption, but a string of large numbers works just as well. This algorithm acts separately on each time point and does not directly influence the separate time points. This procedure allows for removal of the intensity fluctuations of the X-ray spectra[93]. It can be modified easily to recreate the standard ΔOD by simply subtracting the signal obtained at a time delay with known zero signal, $\Delta OD(\tau) = OD(\tau) - OD(-200fs)$. This can also be combined with edge referencing to remove noise associated with harmonic modulation, the 2ω peaks of the fundamental laser

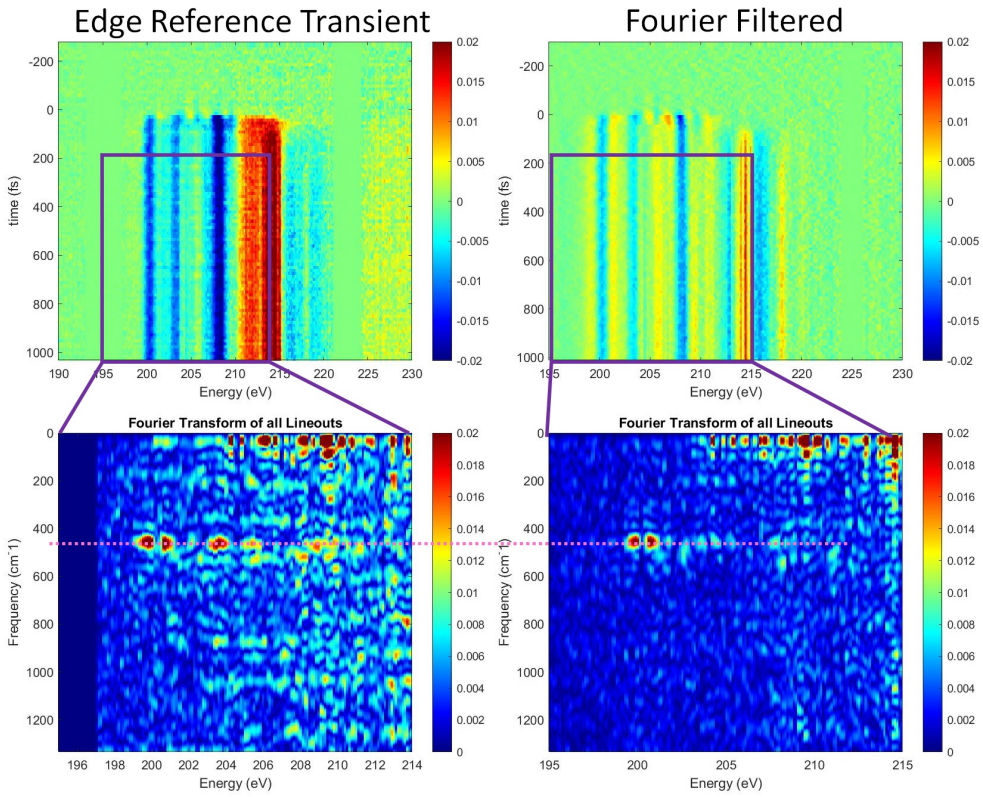

Figure 3.4: The results of noise filtering by edge referencing and Fourier filtering are compared. The spectral features have the low frequency component removed by the Fourier filtering, which causes it to have a drastically different shape; although, the frequency information in the time domain is generally preserved. Note that the frequency peak at 203 eV is smaller, due to the greater low frequency components in that region, compared to 200 eV.

for HHG that shift in energy with changing phase matching conditions.

It is well-suited in the case of narrow absorption lines. In regions where the static X-ray absorption has few low-frequency components (those consisting of stand alone Voigt-like peaks) the Fourier filtered ΔOD data closely resembles that of the standard algorithm, $\Delta OD = -\log_{10}(I_{on}/I_{off})$. A comparison of the 2 noise reduction algorithms is shown for the C K-edge CCl_4 in fig 3.3. In regions where the static spectrum consists of low-frequency components, the Fourier filtered data appears very different from the standard algorithm. For all cases, the Fourier transforms of the data along the time axis show reduced noise signal; although, the actual signal is also reduced in the regions with low-frequency static components, shown for the Cl $L_{2,3}$-edges of CCl_4 in fig 3.4.

Physical parameter extraction by large multivariate fitting

The usual method for extracting temporal information from XTAS data is to take a lineout at a particular energy along the time axis[24, 86, 142, 143]. This is useful in that it does not require a correct model of the temporal evolution. However, in order to make use of all of the information provided, the data must be able to be fully recreated according to a model that represents the physical parameters of the experiment. This is attempted by making a multivariate fit, and this particular implementation does this fitting for multiple datasets at once. An example of a finished fit for one dataset is shown in Fig. 3.5.

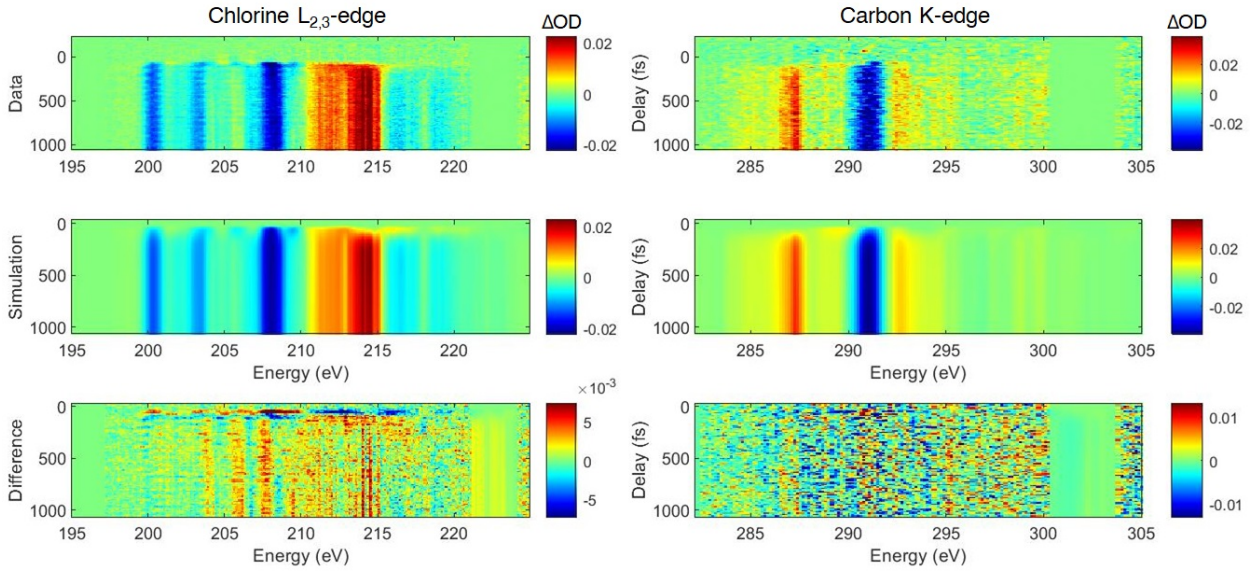

Figure 3.5: An example of one dataset fitted by the multivariate fitting algorithm. Both the chlorine and carbon edges are shown in the two columns. The top row shows the data. The middle row shows the result of the fitting. The bottom row shows the difference between the data and the fitting (the top and middle rows). Note that the colorscale on the bottom row is zoomed by a factor of 2 to highlight errors. This shows only one dataset. For this fitting, 9 datasets are fitted simultaneously. The others are not shown for space considerations.

After the data for each dataset is prepared, it is saved in files containing the ΔOD, the static absorption of that measurement, delay axis, and pixel-to-energy calibration axis. A dataset is the set of data taken continuously with no changes to the experiment, usually datasets represent data from different days, but they may also be single days with multiple conditions. Slight differences in energy calibration and sample pressure are determined by comparing the static absorption of each dataset to a master static spectrum. Changes are made to internal parameters are made accordingly to energy calibration and pressure to make each dataset comparable to each other. These are all loaded into a single program to

fit all of them to a model.

The model is concerned with 2 different parts: 1: non-oscillatory changes to different electronic states, including ionization, excited states, or extreme nuclear changes, and 2: oscillatory changes, in this case due to vibration. A complete model of both are necessary for extracting the CEPES, and this model will be used in part for state disambiguation in chapter 4. For the sake of an example, this description will use $CCl_4{}^+$ as a typical case.

The first part of the model follows the general assumption that

$$\Delta OD = (P_1 \times OD_1 + P_2 \times OD_2 + P_3 \times OD_3 + ... + P_{static} \times OD_{static}) - OD_{static}$$

where, $P_1 + P_2 + P_3 + ... + P_{static} = 1$ are coefficients denoting the percent of molecules in a particular state at a particular time and P_{static} is the percent that remain in neutral CCl_4. The optical density, OD, of each of the states is the goal of this fitting procedure. The number of states involved is able to be changed, based on the expected number of states. In this case, at least 3 states are necessary to get a decent representation of the data, the C_{2v}, C_{3v}, and CCl_3 + Cl^+ forms.

The new absorptions, OD_1, OD_2, etc., are represented pixelwise as parameters simply by absorptions spaced linearly between 2 energies. For example, the Cl L-edge used 201 points, and the C K-edge 81 points. These linear spacings were interpolated onto the nonlinear energy axis that converts camera pixels to photon energy of each dataset. This representation of absorptions is very inefficient in terms of numbers of parameters, but it is exceptionally faster in converging to the global minimum. A set of pairs of absorption and the spacing from the last point in energy was also tried that required roughly 1/3 of the number of parameters, but it took ∼40 times as many iterations to converge. The more chemically accurate representation with Gaussians corresponding to particular transitions was also attempted, and while it could represent the static spectra with the fewest parameters, 30 for the Cl L-edge and 15 for the C K-edge, the set of values that were fit simultaneously (parameter space) was so riddled with local minima that it often would not change the parameters from their initial values. Another representation that was attempted was representing the static spectrum as a Power series, where additional terms in the series were added as sequential fits, which worked well for a single new static spectrum in SF_6, but does not work as well with multiple new spectral populations and required many parameters so was slow to build up the necessary terms, especially as sharp spectral features require a large number of elements in the power series. For these reasons, a power series representation was abandoned after SF_6.

The states are evolved in time to allow one state to become another and capture the dynamics of the system. When one state becomes another, its population is simply transferred into the absorption of the new one with no intermediate transition, because doing so would overly complicate the algorithm with minimal gain. The method of population fitting is to represent each state's P population as a function of time with two single exponentials for rise and decay:

$$P_1(time) = (erf((x-c)/0.1fs)+1) \times (-1*a*e^{(x-c)./(-1*\tau_{in})}+a) \times ((1-d)*e^{(x-c)/(-1*\tau_{out})}+d)$$

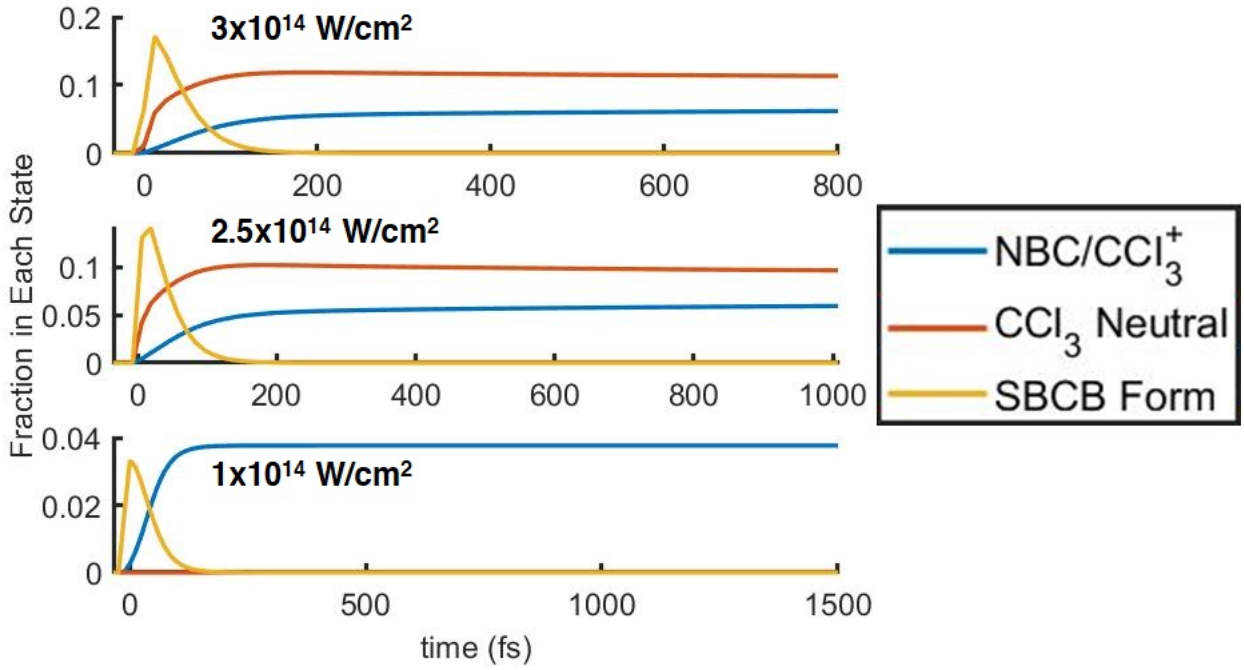

Figure 3.6: An example of the population curves used in a fitting are shown for 3 datasets in a 9 dataset fitting. The fraction in each state is defined such that 100% = 1, 20% = 0.2, etc. The 3 datasets represented have approximate intensity of the pump pulse of 3×10^{14} W/cm^2, 2.5×10^{14} W/cm^2, and 1×10^{14} W/cm^2. The colors of the curves represent the same states in each plot, blue: NBC, red: CCl_3 neutral after Cl^+ dissociates, and yellow: SBCB form.

where c is a time offset to compensate for poorly decided time zeros, τ_{in} is the time constant for growing in, τ_{out} is that for growing out, a determines the maximum population, and d determines the final population of that state as a percentage of the maximum. The error function, erf, at the beginning is to set the population to zero before ionization and allow it to evolve after that. An example of population curves resulting from a fit are shown in Fig. 3.6. This function is chosen over subtraction of exponentials in order to be able to allow a population to finish at an arbitrary value, rather than 0, so that the same function can be used for initial, intermediate, and final states. Population curves are created for each state, and the curves are then normalized to ensure $P_1 + P_2 + P_3 + ... + P_{static} = 1$ at each time point. This is done to reduce the amount of local minima in the parameter space so that the fit can better find the global minimum, and this is the reason for several design decisions in this program. A potentially more accurate model might have been to assign k values between each state and calculate the populations numerically as a function of time; however, this would have required more time, taking the required time to run the algorithm from hours to potentially days.

The amount of total ionization for each dataset was determined by fitting to a single new state and minimizing the second derivative by transition energy of that state's absorption. This is similar to what's done in static add back techniques[21, 84], which results in a percent ionization chosen that minimizes the contribution of the original static spectrum in the excited state spectrum while ensuring that there is no negative absorption. When multiple new states are used, the ionization percent will tend towards 100% for the most intense cases, so it is instead held constant at the result determined by a single state. Minimization of the second derivative of the new states is also used when multiple new states are fitted to reduce trading between multiple states; however, it makes features such as the narrow Rydberg lines of Cl and Cl^+ get smoothed over.

The second part of the model is concerned with the oscillatory features due to the vibrations. The main assumption of this part of the model is that described in the introduction that the energy of absorption is equal to the Potential Energy Surface of a specific core-excited state minus that of the ground state:

$$E_{photon}(q) = PES_{core-excited}(q) - PES_{ground}(q)$$

where q is the movement along the vibrational mode. In the model, $E_{photon}(q)$ is represented as a polynomial with a potentially variable degree; although, only SF_6 was found to have good enough S/N to make use of a quadratic or above. Another assumption was that the vibration occurs in a part of the potential well that is approximately harmonic, i.e. that the vibration q position can be denoted by a sine function $q(t) = A \times sin(\omega(t - c) - \phi)$, where A is the amplitude of vibration, proportional to the input power, ω is the frequency of vibration, c allows for slightly shifted time zeros in each of the individual datasets, and ϕ is the phase of the vibration, relative to time zero. The difference between the c and ϕ parameters is that c affects the rise of excited and ion signals and is allowed to change for each dataset, while ϕ is held constant across all datasets. The phase parameter is allowed to change as a fit, and it was found to be close to $\pi/3$; although, this is may be because the program defines time zero as the start of the ground state bleach (when the leading edge of the pump pulse arrives). Time zero is better defined as when the pump pulse is at maximum intensity. The evolution of the absorption with this assumption is simply that the Voigt function of static absorption changes in energy without changing its shape:

$$E_{photon}(t) = E_{polynomial}(q)(A \times sin(\omega(t - c) - \phi)$$

To note, while this assumption is a simplification, a more chemically accurate model was created and used that defined the vibration q position as a superposition of Morse vibrational levels, which could lead to different absorption shapes, based on the vibrational wavepacket. However, the result of this fitting was that the superposition and resultant wavepacket approximated the simplified assumption result, but required much more computational power. The simplified model provided exceptionally accurate fits, so the chemically accurate model was abandoned. One last assumption was made, that the all molecules in the electronic ground state molecules experience the same electric field and vibrations. This does not affect

the relative slopes of the core-excited states within a measurement and such an assumption is generally made for experiments like this[140].

The ΔOD as a function of time is then calculated based on this model and is broadened by convolution with a Gaussian to account for the temporal resolution of our experiment.

The model is subtracted from the data and fed into a minimization of least squares fitting algorithm, lsqnonlin in Matlab. The parameters that are needed and common to all datasets are:

1. OD of each new state
2. Frequency and phase of the neutral vibration
3. Core-Excited state slopes for the vibration of each transition
4. The lifetime constants, τ_{in}, τ_{out}, and d, for each of the new states

The parameters that are unique to each individual dataset are:

1. Timing delay offset, c
2. Population parameters, a, for each state in each dataset
3. Vibrational amplitude of the neutral
4. Temporal broadening amounts

3.3 Vibrations of SF_6

The molecule SF_6 is chosen because it contains multiple electronic states accessible with X-ray absorption, $2p^{-1}$ a_{1g}, $2p^{-1}$ t_{2g}, and $2p^{-1}$ e_g, each of which have a spin-orbit split core-state from the $2p_{3/2}$ and $2p_{1/2}$, separated by 0.77 eV; although, the e_g X-ray absorption is sufficiently broad that the spin-orbit splittings are not resolvable[144, 145]. In the ground state, these absorptions occur at: $2p^{-1}$ a_{1g}: 172.27 and 173.44 eV, $2p^{-1}$ t_{2g}: 183.40 and 184.57 eV, and $2p^{-1}$ e_g: 196.2 eV[144, 145], shown in fig 3.7. Only the a_{1g} state exists below the ionization potential; the t_{2g} and e_g states are located in a shape resonance, a state above the ionization potential, but bound by a potential barrier, which can introduce difficulties in theoretical calculations[146–148].

Additionally, SF_6 possesses 15 vibrational modes, but due to high symmetry, many are degenerate. For the purposes of the accessability by this experiment, only 3 non-degenerate modes are Raman active[149]. the symmetric stretching ν_1 (ν_1 = 775 cm^{-1} T_1 = 43 fs), asymmetric stretching ν_2 (ν_1 = 643 cm^{-1} $8t_2^*$= 52 fs) and bending ν_5 (ν_5 = 525 cm^{-1} T_5= 63 fs). The Fourier transform in fig 3.7 clearly shows the ν_1 mode but shows no signal for the other Raman active modes. An analysis of the ν_1 mode is given first, and a potential reason for the lack of observation of the other modes is give after that. These vibrational modes and

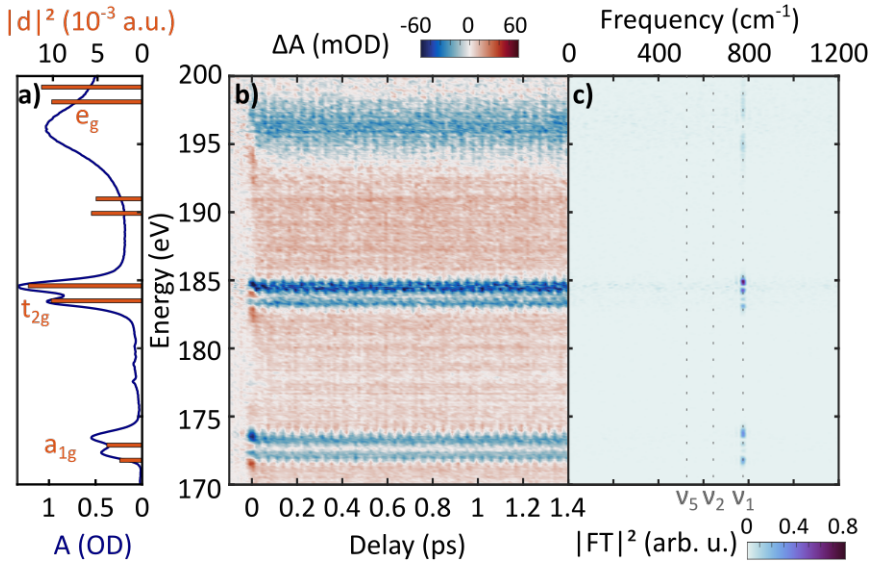

Figure 3.7: The static absorption spectrum of SF_6 is shown on the left. The spectrum is measured in this experiment. The lines are the calculated energies by Dr. Kimberg. The measured ΔOD from XTAS experiment is shown in the middle. The right shows the Fourier transform of the ΔOD data, showing only signal at the ν_1 mode.

their wavepacket dynamics have been studied previously[150–153], but never with respect to their core-excited states.

At low pump intensity, vibrations are observed in SF_6 with no other changes in the ΔOD. However, at higher intensity, a non-oscillatory signal arises that is attributed to $SF_5{}^+$. This signal can be extracted by 2 methods. The first is simple scaled addition of the static absorption to the ΔOD data by the equation $OD = \frac{\Delta OD}{IonizationFraction} + staticOD$, where the amount of ionization is an estimate. This will include other effects, such as broadening from vibrations. The second is to use the global fitting program, which accounts for both vibration and ionization simultaneously. Both are shown in fig. 3.8 in comparison to the ground state static absorption of SF_6.

Core-Excited Potential Slopes of SF_6

Core-excited potential slopes are extracted from all of the datasets by the fitting algorithm described previously. These slopes are in the form of eV vs vibration mode, q; although, the X-ray data contains only information on the relative value of q, so q is chosen arbitrarily to set the slope of the first state to -1 eV/q. This defines the q values, such that the other electronic states can be reported as relative slopes. In order to translate these relative slopes to absolute, the value of q would be scaled to the actual vibrational amplitude, which can be predicted from numerical solutions of the time-dependent Schrodinger equation if the

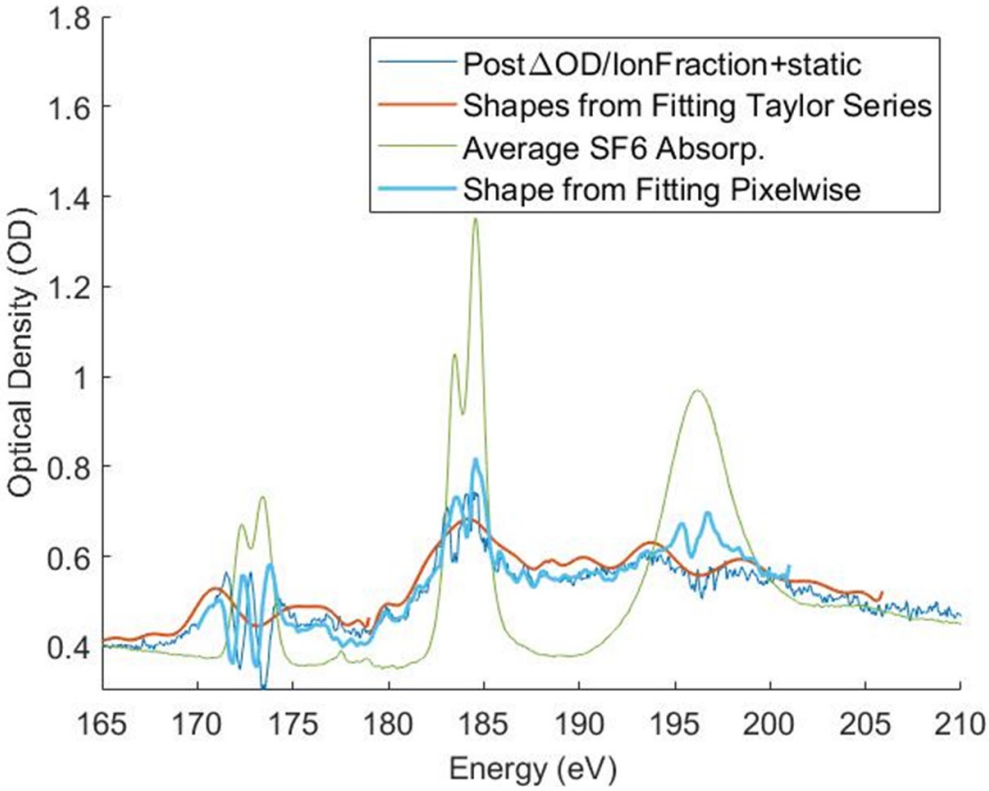

Figure 3.8: The absorption associated with the non-oscillatory data is shown and compared to the ground state SF_6 absorption. Shown are 3 different ways of extracting the absorption of the new OD. Previous experiments have used the $OD_{ion} = (\Delta OD/IonFraction +$ ground state static absorption)[21, 84], which is fast and easy to calculate, but requires some guess at the ionization fraction and will include errors if additional signals are present, such as vibration. The red line is the result of the fitting procedure for the vibration using a Taylor series to represent OD_{ion}; it is limited to low frequencies. Lastly, the teal line is the result of the newer fitting procedure using a pixelwise representation of OD_{ion}; it should be the most accurate. This non-oscillatory absorption is assumed to derive from $SF_5{}^+$ as $SF_6{}^+$ is known to be unstable[154].

intensity of the pump pulse is known[137]. However, the absolute intensity of the pump pulse is difficult to calculate without error, due to its dependence on the focus spot, which can be difficult to reproduce and measure, and the pump pulse duration and temporal shape, which changes on a daily basis and can only be estimated at the sample focus. A possible way to measure the pump intensity at the sample focus is to look at the rate of Ar ionization by strong-field ionization, which can be estimated from calculations somewhat accurately[155, 156], but the X-ray signal does not report exact rates and again the relative ionization

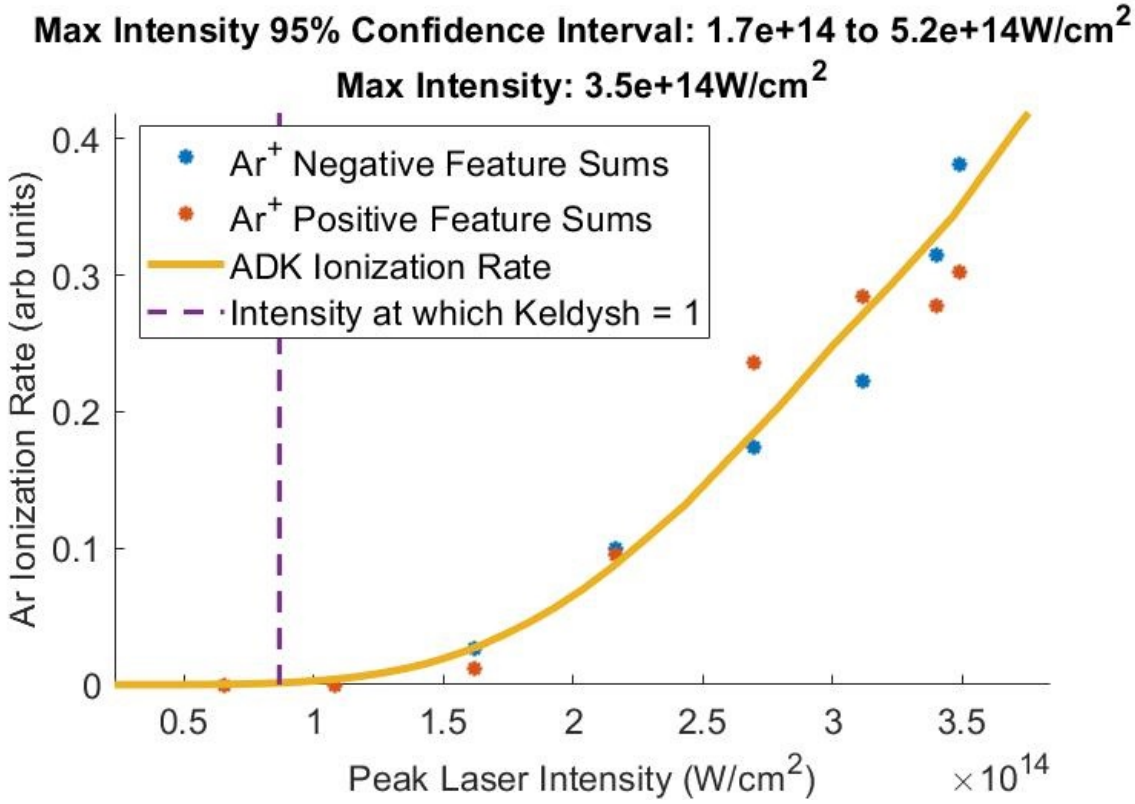

Figure 3.9: Internal calibration of the pump electric field intensity is done by comparison to the ionization rate of argon, using the ADK rate[155, 156]. The intensity for which the Keldysh parameter, γ, is equal to 1 is also indicated, which is the intensity above which ionization is generally considered to be tunnel ionization, compared to multiphoton ionization[157].

amounts must be obtained and compared to each other, which is done by linearly scaling the X-ray intensity and ionization rate until agreement with the shape of the literature ionization rates is reached. This comparison is shown in fig 3.9, which suggests that the maximum intensity is $3.5 \pm 1.8 \times 10^{14}$ W/cm^2; although, this estimation has not been used previously in other works and may contain some degree of systematic error, such as making an assumption about the pulse duration, which will affect the ionization rate[155]. Although, estimates based solely on the measured power and spot size are prone to measurement mistakes of their own, such as assuming that the spot size and pulse duration are perfectly Gaussian. Those estimates tend to overestimate the intensity, especially given that the pump beam is focused with an annular mirror, reducing how Gaussian the focus will be. The error present in the absolute values of the intensity are larger than the errors of the relative slopes obtained, as the relative slopes can be compared within an intensity measurement, so only

the relative slopes are compared.

The relative slopes of each of the core-excited state absorption for each electronic level for a polynomial of degree 1 are $2p^{-1}$ a_{1g}: -1.00, $2p^{-1}$ t_{2g}: -0.40 ± 0.07, and $2p^{-1}$ e_g: -1.2 ± 0.1. There is no error associated with the a_{1g} slope, because it is defined to be -1; any error that exists in the a_{1g} slope is included in the other two slopes. The ordering of slopes from smallest to largest is t_{2g}, a_{1g}, then e_g. The slopes with polynomial of degree 2 are $2p^{-1}$ a_{1g}: -1.00 ×q - 1 ± 4 ×q^2, $2p^{-1}$ t_{2g}: -0.40 ± 0.07 ×q - 0.3 ± 0.6 ×q^2, and $2p^{-1}$ e_g: -1.16 ± 0.13 ×q - 1 ± 3 ×q^2. These are both shown in figure 3.10. The negative quadratic terms suggest that the CEPES has a smaller quadratic term than the ground state PES. The 95% confidence intervals are larger than the negative values, so the experimental data does not prove that the quadratic term is smaller. The results show relatively small error due to use of multiple datasets in the fitting and the information in each agreeing with the model.

Additionally, because the amplitude of the vibrational coordinate is expected to scale linearly with pump intensity[140] and the amount of ionized SF_6 is expected to scale non-linearly by either multiphoton ionization or tunnel ionization[156, 157], the accuracy of the model can be assessed by comparison of these trends. Figure 3.11 shows this comparison for a power scan experiment, wherein the pump power was modulated by a half-wave plate and polarizer and measurements at different powers were taken as close to simultaneously as possible, eliminating potential changes to pump intensity from differing focus spots or alignment issues. The results show good agreement with expectation.

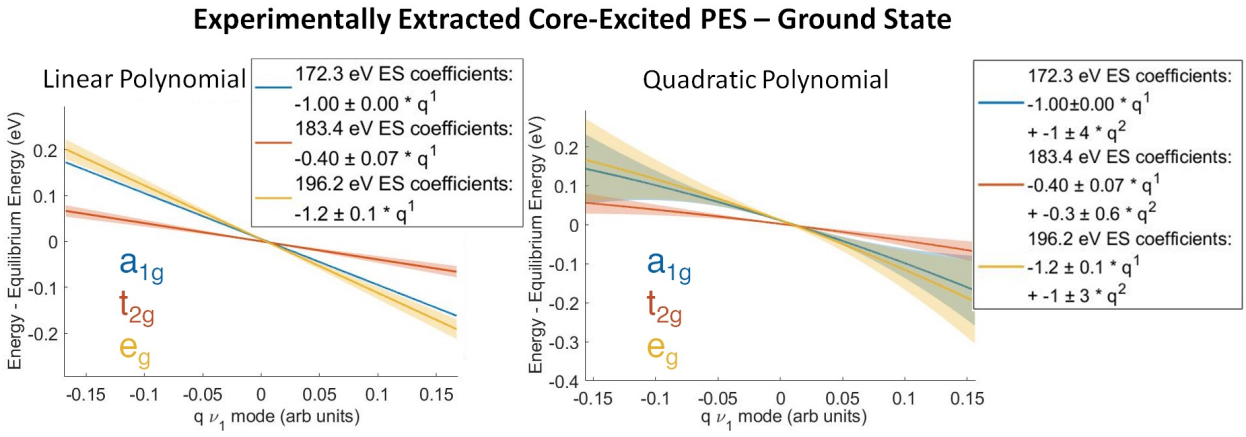

Figure 3.10: Extracted values for the core-excited states minus ground state for each electronic level (blue: $2p^{-1}$ a_{1g}, red: $2p^{-1}$ t_{2g}, yellow: $2p^{-1}$ e_g) for a polynomial of degree 1 (left) and of degree 2 (right). The 95% confidence intervals are shown as the bounded portion. The vibrational coordinate, q, is scaled such that the a_{1g} slope is -1.

Yet another way to obtain absolute slopes for the CEPES is to compare with a known slope for one of the electronic states, which defines what the x-axis, q, must be scaled to.

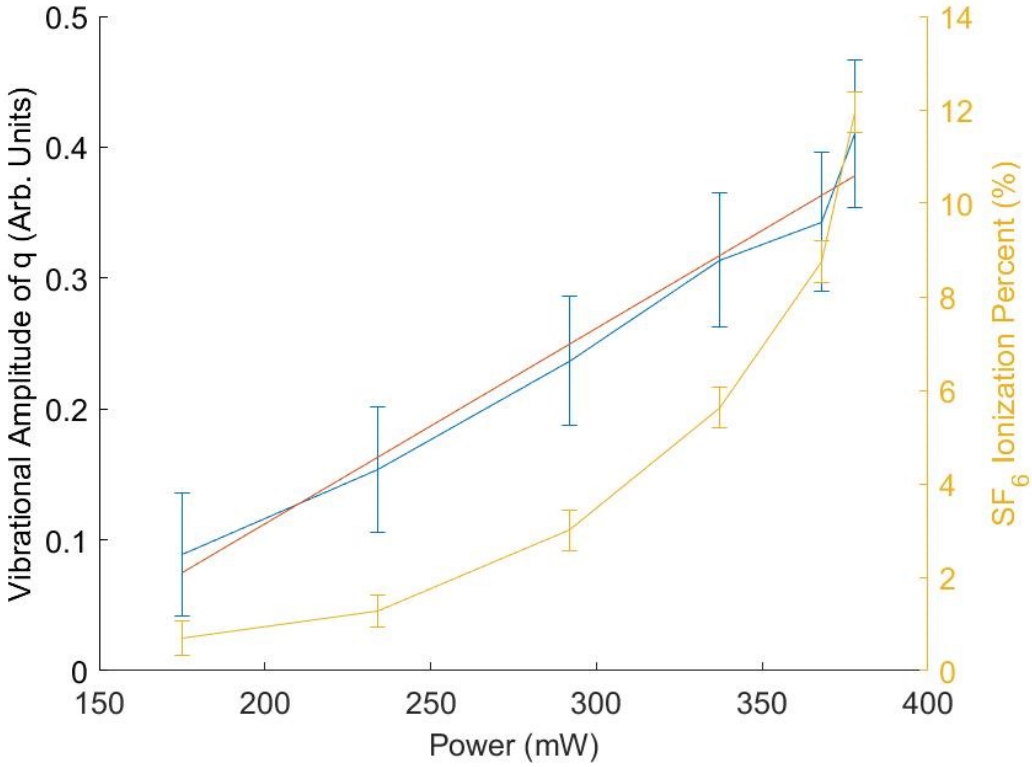

Figure 3.11: The fitting results of the vibrational amplitude and ionization percent are shown for a power scan of SF_6 taken on the same day. The linearity of the extracted vibrational amplitude (blue) and the non-linearity of the extracted ionization percent (red) show that the fitting procedure reproduces the expected dependence on pump intensity.

Experimental values for these slopes are obviously not available, so comparison can be made to theory. First though, the accuracy of the theory compared to this experiment can be assessed by comparison to the relative slopes attained by each. For this, a collaboration was done with Victor Kimberg's group, Pavel Krasnov and Svyatoslav Blinov from Department of Theoretical Chemistry and Biology, KTH Royal Institute of Technology, Stockholm, Sweden and the International Research Center of Spectroscopy and Quantum Chemistry, Siberian Federal University, Krasnoyarsk, Russia. The group uses the DFT method[158] under O_h symmetry constrained with the GAMESS software[159] using B3LYP functional[160] and def2-TZVP basis set[161]. Frequency-dependent polarizability at 800 nm along the ν_1 normal coordinate is calculated by the TDDFT approach[162] using the same level of theory. The B3LYP TDDFT method is also employed for the ground and core-excited states PES calculations using the ORCA software[163] with ano-pVTZ basis set[164], RI approximation[165], and quasi-degenerate perturbation theory[166] for spin-orbit coupling inclusion.

State Coefficient $E_{photon}(q) = \text{b}\times\text{q} + \text{c}\times\text{q}^2$	Experimental Linear	Experimental Quadratic	Calculation Kimberg
a_{1g}: b	-1	-1	-1
a_{1g}: c		-1±4	
t_{2g}: b	-0.40±0.07	-0.40±0.07	-.38
t_{2g}: c		-0.3±0.6	
e_g: b	-1.2±0.1	-1.2±0.1	-1.05
e_g: c		-1±3	

Table 3.1: The experimentally extracted coefficients for SF_6 are compared to theory. In all, q is scaled such that the slope of a_{1g} is -1.

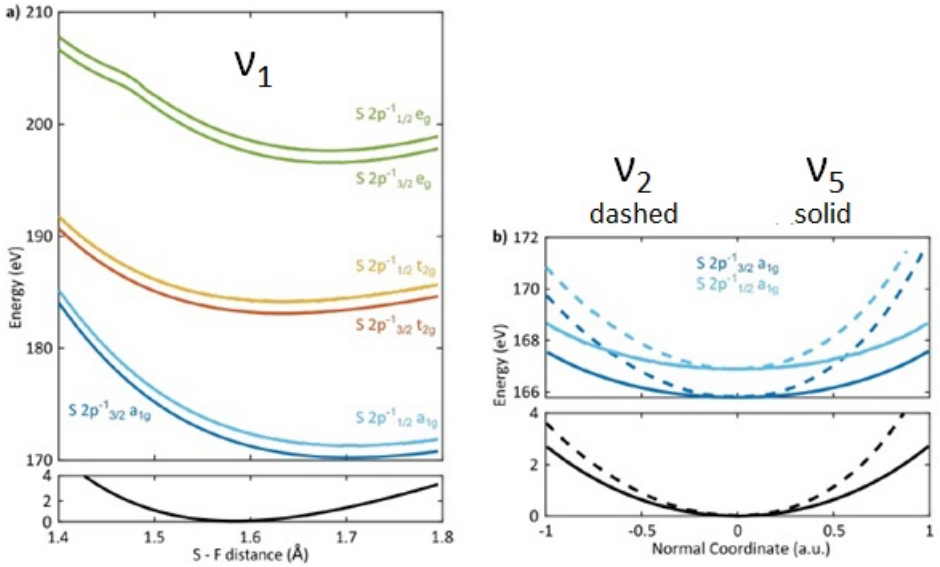

Figure 3.12: a) Ground (bottom, black) and core-excited (top) states potentials calculated along the ν_1 mode. b) Same as a) along the ν_2 (dashed line) and ν_5 (full line) modes.

The CEPES gradients calculated are on the order of 10 to 30 eV/Å, shown in fig 3.12a. The relative slopes calculated are $2p^{-1}$ a_{1g}: -1, $2p^{-1}$ t_{2g}: -0.38, and $2p^{-1}$ e_g: -1.05. Comparison to experimental values are shown in table 3.1. These are in the correct order of increasing slope as the experiment: $2p^{-1}$ a_{1g}: -1.00, $2p^{-1}$ t_{2g}: -0.40±0.07, and $2p^{-1}$ e_g: -1.17±0.13, and the t_{2g} state is well within the 95% confidence interval given by the experiment. However, the e_g state is only barely within the interval (extra significant figures are given to show that this is true). This suggests that either the experiment or theory or both is lacking. On the theory side, TDDFT has been shown to have issues with charge transfer, which may be an

issue considering that the e_g state is high in the shape resonance[147, 148]. Additionally, in the static absorption calculation in figure 3.7, the e_g state does not match well with the experimental absorption. On the experiment side, there are several assumptions made about the model, and the extraction method has not been shown to be successful yet. Although, this thesis will show in the next section another system that extracts the CEPES on states that lie below the ionization potential, bound states, as opposed to the shape resonances in SF_6, with comparison to a different level of theory that shows much better agreement.

In the Fourier transform of the experimental data, the other Raman active modes did not show a peak at their respective frequencies. The reason for this is two-fold. First, the ν_1 mode is generally stronger in Raman activity[149, 150]. The second reason can be shown by the theory that the slope of the CEPES has the same curvature as the ground state, shown in fig 3.12b. If the shape of the two are equivalent, the subtraction would have no q-dependence and would thus be invisible to experiment, which is what is observed. This is a major limitation of this technique for measuring and observing potential surfaces along an arbitrary vibration mode.

3.4 Vibrations in CCl_4

The molecule CCl_4 is unique for a few reasons. The first is that it has 2 anti-bonding electronic states that are well separated and easily accessible by X-ray absorption: the $7a_1^*$ and a triply degenerate $8t_2^*$[167, 168], both of which are typical bound states, and thus can be calculated more easily by theory.

The second is that all of the vibrations of CCl_4 are Raman active and have been measured with high frequency resolution[169, 170]. These consist of the totally symmetric, a_1 ν_1 mode, 456.6 cm$^-$1 (73.05 fs), the e bending ν_2 mode, 218.0 cm$^-$1 (153.0 fs), the asymmetric bend, t_2, ν_3 mode, 790.6 cm$^-$1 (42.19 fs), and the t_2 bending ν_4 mode, 309.7 cm$^-$1 (107.7 fs)[169]. The experiment was undertaken under the premise that the stronger Raman transitions in these other modes would allow measurement of multiple frequencies and extraction of core-excited potential energy surfaces (CEPES) along each normal coordinate. Additionally, the vibrations have a Fermi resonance between the ν_3 and the sum ν_1+ν_4, which splits and shifts the frequency of the two[169], which may lead to interesting effects in the X-Ray spectra.

The third reason is that both elements have absorption in the soft X-ray range that the instrument can probe. Specifically, the Cl $L_{2,3}$-edge, the $2p_{3/2}^{-1}$ and $2p_{1/2}^{-1}$, are around 200 eV with a spin-orbit splitting of 1.6 eV, and the C K-edge, the $1s^{-1}$, is around 285 eV[167]. This enables simultaneous observation of both elements as the molecule vibrates, which allows comparison of the CEPES between the central atom and terminal atoms. There is also an additional chlorine edge, the Cl L_1-edge, the $2s^{-1}$, at 260 eV, but this edge is too broad to extract useful information, especially for the purposes of vibrations, where the signal is proportional to the sharpness of the static absorption. The absorption spectrum is shown in fig 3.13. Assignments of the peaks is made in table 3.2. The spin-orbit area ratio differs from the expected number of orbitals of 2:1 for the L_3:L_2[173], which is somewhat common

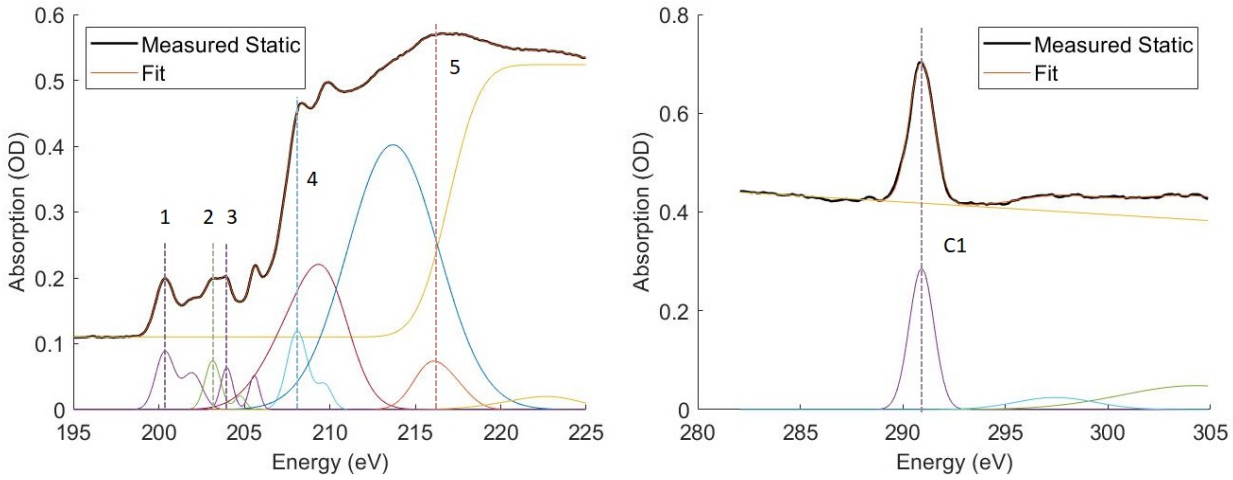

Figure 3.13: The absorption of CCl_4 is shown at the chlorine $L_{2,3}$-edges and carbon K-edge. Additionally, a breakdown of the absorption into the individual absorption components is shown. The chlorine edge contains the separate spin-orbit splitting of 1.6 eV from the L_3- and L_2-edges. The extra Gaussians after the rising edge are to better reproduce the measured data. The carbon absorption offset is due to the remaining absorption from the Cl atoms. Assignments of the absorption peaks are made in table 3.2.

for some of these edges[144]. In the static absorption, the downside of simultaneous element absorption becomes apparent; the absorption from the Cl edge extends all the way to the C edge, where it represents ∼50% of the absorption, even at the point of highest carbon absorption. This leads to far smaller photon flux available at that edge and increases the noise. In the static spectrum, it also becomes apparent that the $7a_1^*$ electronic state is not visible at the C K-edge, which is due to the matching symmetry of the core state and the $7a_1^*$ state, making the transition forbidden[167]. Still, the $8t_2^*$ state can be observed and measured.

An example ΔOD dataset and Fourier transform are also shown in fig 3.14. In the Fourier transform, the totally symmetric ν_1 mode is clearly visible at 456 cm^{-1}, especially at the Cl edge, but also less clearly at the C K-edge. The frequencies of the other modes are not visible. The ΔOD also shows non-oscillatory signals that change over the course of the time range. These correspond to changes following ionization and will be discussed in a later chapter.

Core-Excited Potential Slopes of CCl_4

The core-excited potential energy surfaces were extracted using the same program as previously. Again, the values obtained represent the subtraction of the CEPES and the the

Peak Assignments			Spin-Orbit Splitting Area Ratio
Peak	Energy (eV)	Assignment	$\text{Area}_{2p_{1/2}^{-1}}$ / $\text{Area}_{2p_{3/2}^{-1}}$
1	200.35	Cl $2p_{3/2}^{-1}$ $7a_1^*$	
1_{s-o}	201.95	Cl $2p_{1/2}^{-1}$ $7a_1^*$	1.37
2	203.15	Cl $2p_{3/2}^{-1}$ $8t_2^*$	
2_{s-o}	204.75	Cl $2p_{1/2}^{-1}$ $8t_2^*$	0.39
3	203.98	Cl Rydberg	
3_{s-o}	205.58	Cl Rydberg	1.40
4	208.1	Cl $2p_{3/2}^{-1}$ Delay onset and shake-up	
4_{s-o}	209.7	Cl $2p_{1/2}^{-1}$ Delay onset and shake-up	0.45
5	216	Cl Shape Resonance	
C 1	290.91	C $1s^{-1}$ $8t_2^*$	

Table 3.2: The assignments of the fitted absorption components, based on previous literature[171, 172]. The energy of the spin-orbit splitting for the Cl L_2-edge (s-o peaks) is 1.6 eV higher than the L_3-edge energy. The rightmost column displays the ratio of the area of the peaks for $\frac{L_2}{L_3}$; the expected ratio is 0.5, based on orbital splitting[173].

ground state, and the relative slopes of each electronic state are compared to each other with the Cl $2p^{-1}$ $7a_1^*$ slope arbitrarily set to -1. The extracted values are: Cl $2p^{-1}$ $7a_1^*$: -1, Cl $2p^{-1}$ $8t_2^*$: -0.81 $\pm$ 0.08, and C $1s^{-1}$ $8t_2^*$: -0.47 $\pm$ 0.05, which is shown in fig 3.15. The overlap of absorption features in the Cl $L_{2,3}$-edge static and the lower signal-to-noise, especially at the C K-edge, prevents fitting with good error bounds to obtain a quadratic or higher order shape of the CEPES. These slopes show that the terminal atoms have a larger change along the normal coordinate than the central carbon, which can help future experiments to predict expected signals. Additionally, in the Fourier transform of the data, the 456.6 cm^{-1} vibration was observable above the noise at 208.1 eV and its spin-orbit split transition at 209.7 eV, which is usually assigned to a delayed onset Rydberg state or a shake-up state[167, 171]. Extracting this gives a relative slope of -0.18 $\pm$ 0.06, which is much smaller than the other slopes and has a relatively larger range of errors, which suggests the nature of this state is different than the normal electronic states. However, the Rydberg states in either CCl_4 or SF_6 do not show vibration signals, which suggest the 208.1 eV state is an electronic state or something beyond a Rydberg state.

These extracted slopes can be compared to theory again, but at a different level, which has been shown to be more accurate in predicting static spectra and does not require arbitrary shifts to match experimental spectra, Restricted Open-Shell Kohn-Sham (ROKS)[133]. For CCl_4, theory work was undertaken by Diptarka Hait in the Martin Head-Gordon Group. Quantum chemical calculations were performed with the Q-Chem 5 software [174]. Structures were optimized with the ωB97M-V[175] density functional and the aug-pcseg-3[176]

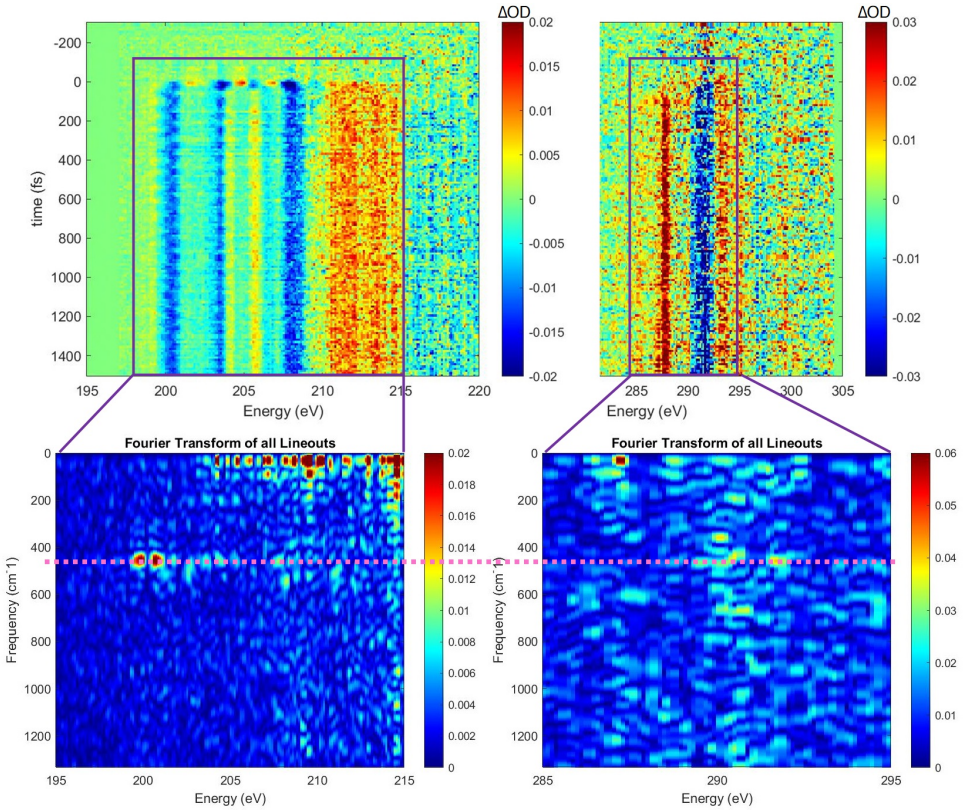

Figure 3.14: Example ΔOD data on the right with the Fourier transform along the time axis at each of those energies shown below. Only the ν_1 mode frequency is visible at 450 cm^{-1}. The positions of the vibrating electronic states are shown in figure 3.13 as peaks 1, 2, and C 1.

basis set. Zero-point energies were found at the same level of theory. Relative ground state electronic energies at the optimized geometries were computed with CCSD(T)[177] extrapolated to the complete basis set (CBS) limit. Core-level spectra were simulated with orbital-optimized density functional theory[178], utilizing the SCAN[179] functional. This approach has been shown to be accurate to ∼0.3 eV root-mean-squared error for both closed-shell[133] and open-shell[180] species, without any need for empirical translation of spectra. Detailed protocols for running such calculations are described in Refs [133] and [180]. Excited state orbital optimization was done with the square gradient minimization (SGM[181]) and initial maximum overlap method (IMOM[182]) algorithms, for restricted open-shell and unrestricted calculations respectively. The aug-pcX-2 basis[183] was used at the site of the core-excitation, and aug-pcseg-2[176] was used for all other atoms.

The absolute slopes given by this theory are: Cl 2p^{-1} $7a_1^*$: -11.09 eV/Å, Cl 2p^{-1} $8t_2^*$: -8.76 eV/Å, and C 1s^{-1} $8t_2^*$: -5.21 eV/Å, where the x-axis angstroms refer to the movement along

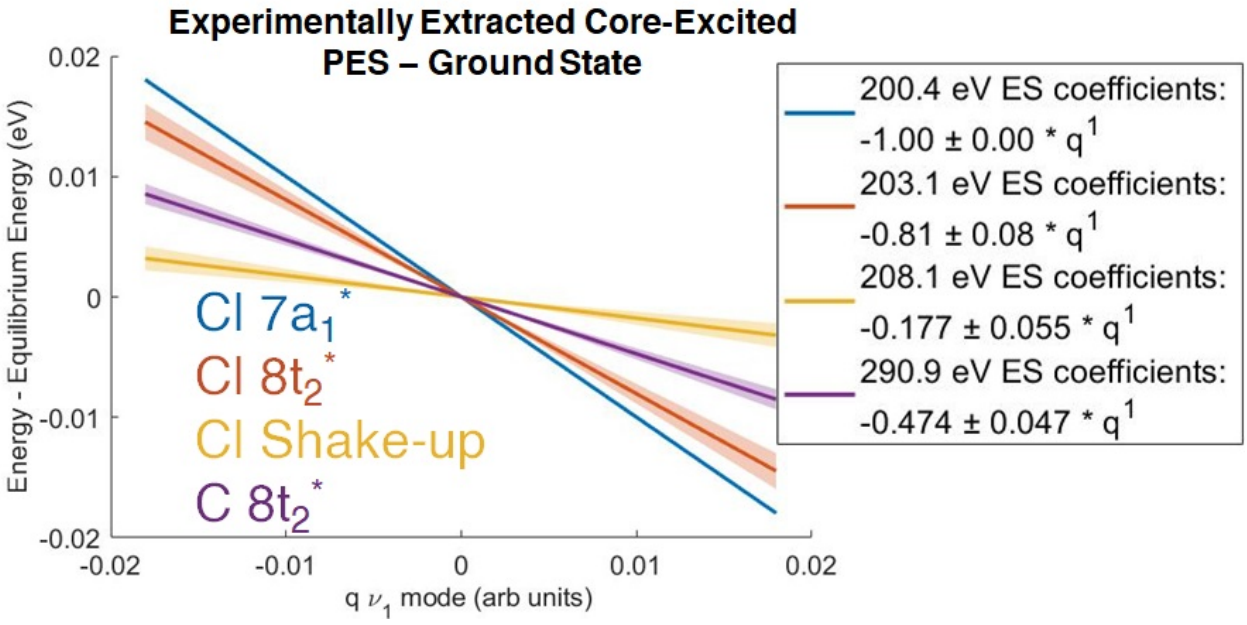

Figure 3.15: Extracted values for the core-excited states minus ground state for each electronic level (blue: Cl $2p^{-1}$ $7a_1^*$, red: Cl $2p^{-1}$ $8t_2^*$, yellow: Cl $2p^{-1}$ shake-up, purple: C $1s^{-1}$ $8t_2^*$) for a polynomial of degree 1. The 95% confidence intervals are shown as the shaded portion. The vibrational coordinate, q, is scaled such that the a_{1g} slope is -1.

State Coefficient $E_{photon}(q) = b \times q$	Experimental Linear	Calculation Hait
Cl $L_{2,3}7a_1^*$: b	-1	-1
Cl $L_{2,3}8t_2^*$: b	-0.81±0.08	-0.79
Cl $L_{2,3}$ Shake-up: b	-0.18±0.06	
C K $8t_2^*$: b	-0.47±0.05	-0.47

Table 3.3: The experimentally extracted coefficients for CCl_4 are compared to theory. In all, q is scaled such that the slope of a_{1g} is -1.

the ν_1 coordinate, in which all bond distances increase by the same amount, which can thus be represented as the change in bond distance. The feature at 208.1 eV was not calculated due as its character is not well understood[167]. Comparison between theory and experiment is shown in table 3.3. The relative slopes for these states are: Cl $2p^{-1}$ $7a_1^*$: -1, Cl $2p^{-1}$ $8t_2^*$: -0.79, and C $1s^{-1}$ $8t_2^*$: -0.47, which agrees strikingly well with the extracted values of -1, -0.81 ± 0.08, and -0.47 ± 0.05. The increased agreement from the SF_6 theory comes from both a better algorithm for X-Ray absorption calculation that does not require arbitrary

shifts to match experiment and from the fact that the states are not shape resonances.

With the increased agreement between experiment and theory, it is more reasonable to apply the theoretical absolute values of CEPES slopes to the experimentally extracted relative values, which gives: Cl $2p^{-1}$ $7a_1^*$: -11.09 eV/Å, Cl $2p^{-1}$ $8t_2^*$: -8.9 ± 0.9 eV/Å, and C $1s^{-1}$ $8t_2^*$: -5.2 ± 0.6 eV/Å, and the shake-up state at 208.1 eV would be 2.0 ± 0.7 eV. From this, the amount of nuclear movement can be estimated for each dataset. The smallest amplitude was 0.0018 Å and the largest was 0.0045 Å. These numbers seem very small, but they are close to the numeric solution of the Schrodinger equation for the maximum expected intensity, 0.006 Å, with the difference likely arising from errors in the expected intensity or deviations in the pump pulse shape from a perfect Gaussian envelope or, from an experimental perspective, an incorrect broadening was used in the extraction. These movements result in only 0.05 eV changes in the absorption from the ground state, but they are measurable by our experiment, which shows the sensitivity of the experiment.

Isotope Effect

Because CCl_4 contains chlorine, there are multiple isotopes that affect the frequency of vibration. The isotope effect has been measured previously[169, 170], and shows the ν_1 mode consists of vibrations at 453.7, 456.6, 459.5, and 462.7 cm^{-1} for molecules containing 0, 1, 2, and 3 Cl^{37}, compared to the more abundant Cl^{35}[169]. With these values and the known abundances of Cl^{35} and Cl^{37}, the amount of constructive and destructive interference is predicted, which is shown in fig 3.16. Based on it, the X-ray ΔOD signal should becomes less clear as the time approaches 3 ps. This destructive interference is expected to cause broadening of the static signal, as it corresponds to one population being red shifted and another blue shifted. The populations are expected to come back in phase at 10.5 ps, so an experiment was performed that scanned 37 time points near time zero, 3.3 ps, 6.6 ps, and 10.5 ps, the results of which are shown in fig 3.16. Indeed, a rephasing of the signal vibrational signal is apparent at 10 ps; although, the expected rephasing of the Fourier signal is 95% of the original, and the measured is ∼40%. This difference may be due rearrangement of vibrational energy, dephasing of the vibration from other sources, or spatial drift between pump and probe over the time difference.

The lack of other vibrational modes

In the Fourier transform of the data, the frequencies associated with the ν_{2-4} modes are not observed. These modes have been shown to be Raman active[169] and so should be present as nuclear motions in the experiment. The first order interpretation is that the CEPES has the same slope and shape as the ground state along those modes. A more accurate understanding can be reached by use of the same theoretical methods, again performed by Diptarka Hait. The results are shown in fig 3.17, which show that for the C K-edge $8t_2^*$ state, the individual electronic states are expected to have significant differences. The issue is that for the triply degenerate $8t_2^*$ state, the component states split in different directions and lead

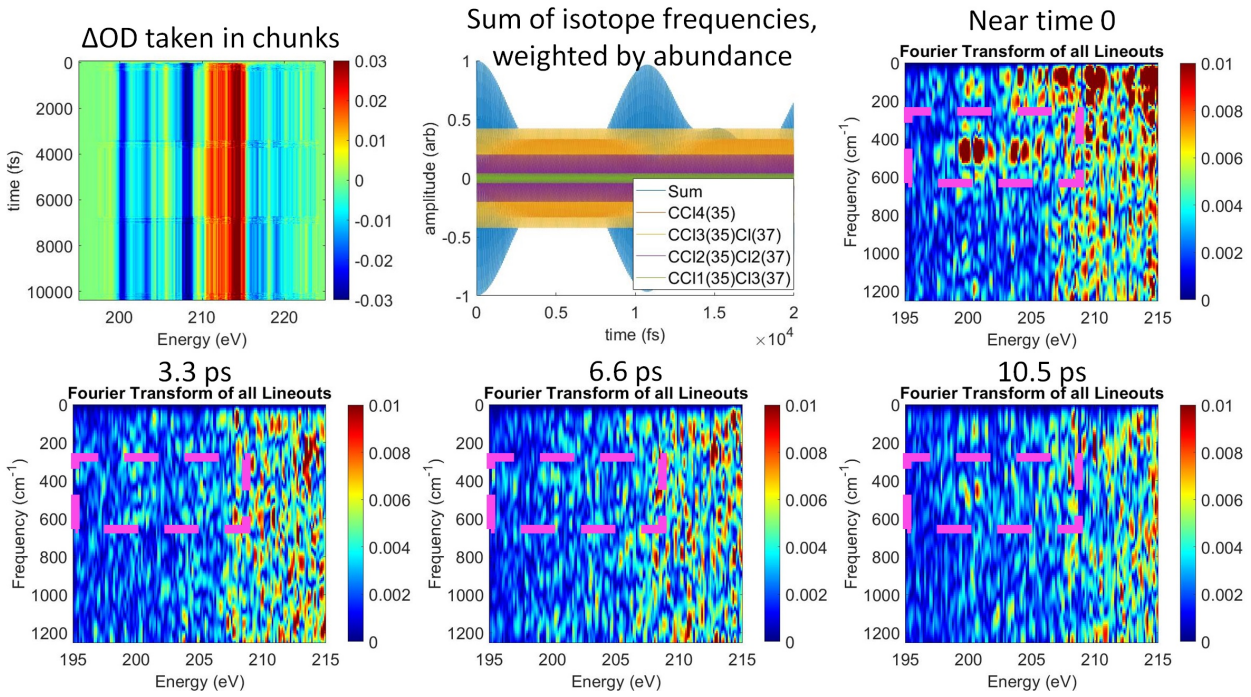

Figure 3.16: The data of a scan that covers 10 ps is shown in the upper left. The scan is broken into 4 equal chunks with no time points in between. The middle shows cosine waves of the frequencies of the ν_1 mode of the isotope combinations with amplitude proportional to their natural abundances; 4 Cl^{37} is not shown due to low abundance. The sum of them is the blue curve, which is the constructive interference between them and the expected coherence of the vibration signal. The rest are Fourier transforms of the 4 chunks, which show a strong signal at time zero, when all isotopes are in phase. This is followed by no signal at 3.3 and 6.6 ps, where the isotopes are out of phase. Finally, at 10.5 ps, the signal reappears with Fourier signal 40% of the time zero signal.

to a net result close to zero difference from the ground state. This is not the case for the ν_1 mode, where the symmetry of the molecule is not broken and all the $8t_2^*$ state remains essentially degenerate as the molecule vibrates. The slopes cannot be directly compared to the ν_1 mode, as there is not an easily definable way to transform the nuclear coordinate, q, to 1 Å, but for the plots shown in the figure, q has been defined as close to 1 Å as the average distance that the atoms move being 1 Å as 1 q unit. For the ν_3 mode as an example, as it is the most Raman active[184], one of the states has a slope more negative than the ν_1 while the others have a positive slope roughly half the value, resulting in a sum that is close to 0.

If this is the cause, the signal in the XTAS data would be slightly different for these modes. The absorption features of the electronic states would broaden as the molecule moves farther from equilibrium and would return to their original values as it returns to

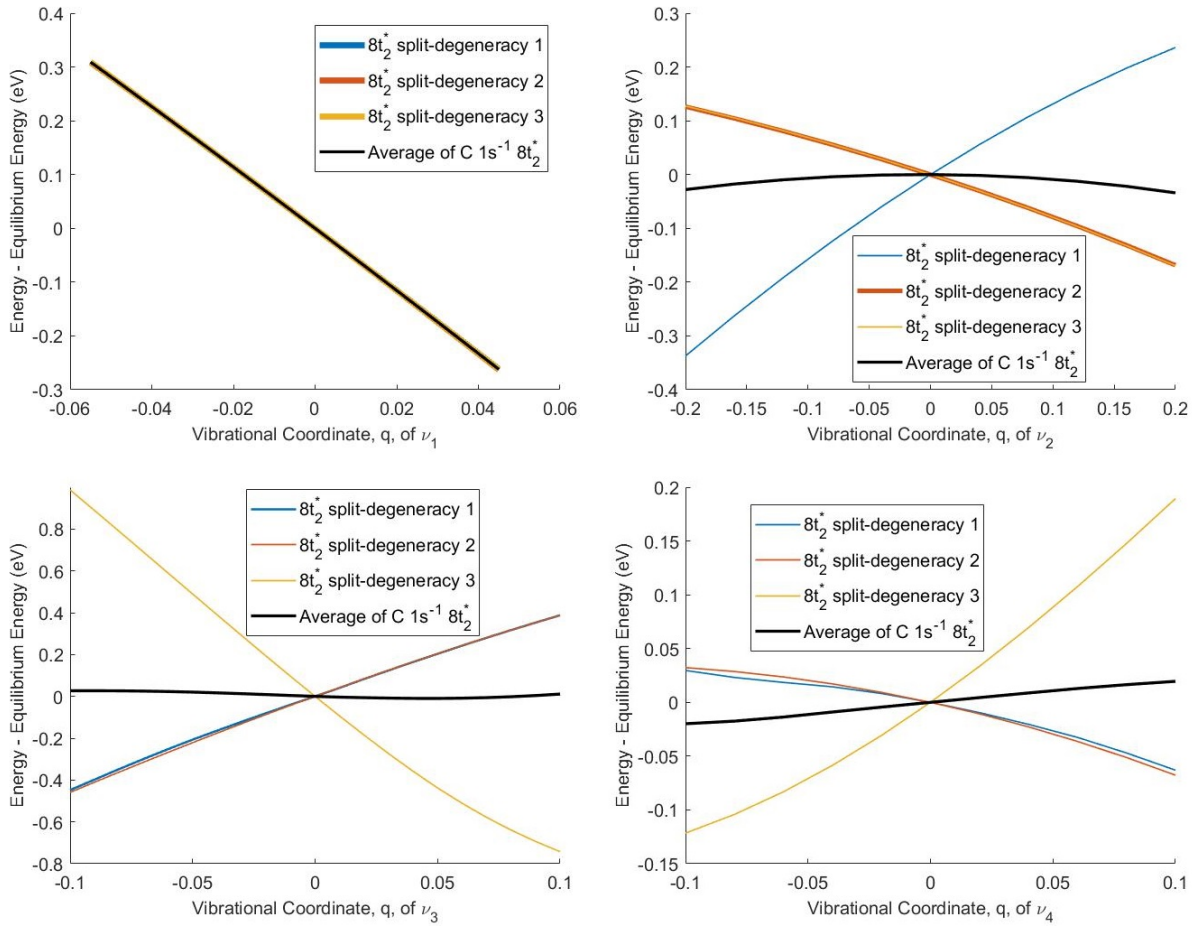

Figure 3.17: Calculated absorption energies at all 4 vibration modes are shown for the C $1s^{-1}$ $8t_2^*$ electronic state. The $8t_2^*$ state is composed of a triple degeneracy, which can be broken by the vibration and leads to destructive interference between them for all modes, except the ν_1 mode.

equilibrium. This would result in an observed frequency of twice the vibrational frequency, and would be more observable by the full simulation of the ΔOD data, as the program does, to make full use of the data at many energies. Unfortunately, the data are too noisy at the C K-edge to do this with CCl_4. It has been attempted, and a possible signal was extracted, but it does not exist above the noise of the experiment.

For other states, like the $7a_1^*$, which is not triply degenerate, the other frequencies might be more observable. However, the C $1s^{-1}$ $7a_1^*$ transition is forbidden. It is not forbidden at the Cl $L_{2,3}$-edge, but the frequencies are still not observed. The problem in this case is slightly different but similar. The four terminal chlorines each contain 3 p-orbitals from

which the absorption can occur. Moving the molecule along the ν_3 mode makes each of the chlorines nonequivalent and makes the 3 p-orbitals nonequivalent within a chlorine. All of these can lead to a mixture of positive and negative slopes that sum to 0. This has not yet been calculated, but will be.

3.5 Vibrations in CO_2

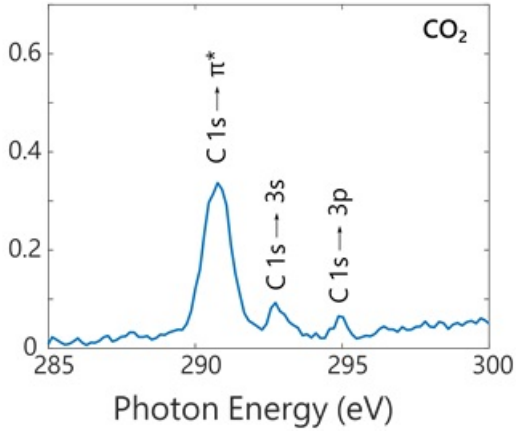

Figure 3.18: The static absorption spectrum of CO_2. Assignments are based on 2 works[185, 186]

In carbon dioxide, only one electronic state is accessible in the X-Ray range, so an investigation of the relative CEPES for carbon and oxygen was not undertaken. However, CO_2 is known for having a very strong Fermi resonance between its symmetric stretch and twice the bending motion[187, 188]. This splits the frequency of the two and gives two frequencies at 1285.4 (26.0 fs period) and 1388.2 cm^{-1} (24.0 fs)[96].

The static absorption is shown in fig. 3.18. Firstly, in the static absorption, the C $1s^{-1}$ 3s peak is clearly visible, despite both orbitals being gerade symmetry. Collaboration with John F. Stanton from University of Florida has suggested that this is due to an exceptionally large Pseudo-Jahn Teller effect in CO_2, which allows the 3s peak to borrow intensity from the the π^*. We will elaborate further in a future paper.

Secondly, in the transient data and Fourier transform in fig. 3.19 there is a non-oscillatory signal in the ΔOD data. Based on the other molecules studied by this apparatus, it's likely that this corresponds to the ion, $CO_2{}^+$. The splitting of the positive features suggests that this may be due to symmetry breaking by the Renner-Teller effect[189], which is the the linear version of the Jahn-Teller effect.

Lastly, the Fourier transform shows peaks at both the expected 1290 and 1388 cm^{-1}. Within this, the two frequencies appear at slightly different energies in the X-Ray data. The

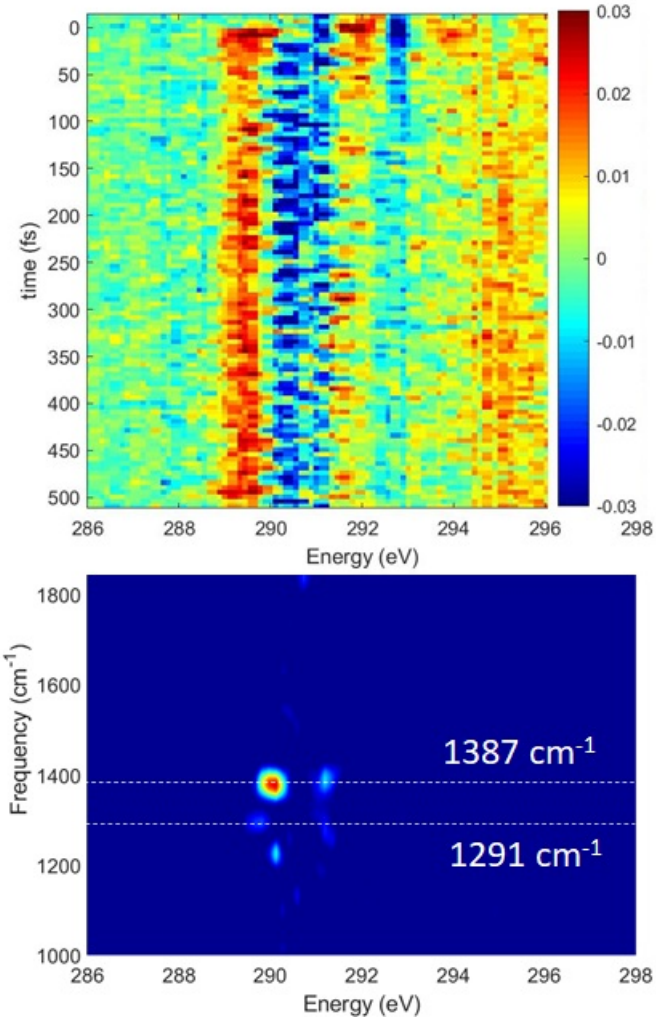

Figure 3.19: The ΔOD data and the Fourier transform of it. It shows vibration signal at different energies for the different parts of the Fermi resonance.

1290 cm^{-1} frequency extends to lower energies, ∼289.7 eV, while the 1388cm^{-1} is peaked at 290.0 eV. Both frequencies have the upper energy peak at the same energy, 291.5 eV. A paper measuring CO_2 in a synchrotron suggest that the main π^* peak is composed of two separate peaks, an A_1, associated with a bending motion, and a B_1, associated with linear motion[190]. The spectra that the paper show match well with the energies at which the frequencies are observed. This suggests that the 1388 cm^{-1} is more associated with the linear movement of the vibration, and that the lower frequency with the bending motion.

3.6 Summary

Experiments using XTAS allow vibrations of molecules to be measured in real time. Development of new code enables extraction of core-excited potential energy surfaces, relative to different electronic states. In SF_6, the extracted relative slopes are $2p^{-1}$ a_{1g}: -1.00, $2p^{-1}$ t_{2g}: -0.396 $\pm$ 0.07, and $2p^{-1}$ e_g: -1.2 $\pm$ 0.1. In CCl_4, the experimentally extracted relative values are Cl $2p^{-1}$ $7a_1^*$: -1, Cl $2p^{-1}$ $8t_2^*$: -0.81 $\pm$ 0.08, and C $1s^{-1}$ $8t_2^*$: -0.47 $\pm$ 0.05. Comparison to different levels of theory show better agreement for ROKS in CCl_4 than TDDFT in SF_6. In CCl_4, larger core-excited slopes are observed for the terminal atoms than the central atoms, and dephasing and rephasing are observed, due isotope effects. In both SF_6 and CCl_4, vibrational modes other than the symmetric stretch are not observed, which theory shows to be due core-excited slopes that match the ground state. This is due to the symmetry-breaking of those modes breaking degeneracy of the core-excited states, which serves as a limitation to XTAS in measurement of vibrations. Finally, in CO_2, oscillations corresponding to the Fermi resonance are observed at different energies in the X-ray, which suggests that the different vibration modes contained in the Fermi resonance couple to different core-excited states.

Chapter 4

Dynamics of CCl_4^+ Ions Prepared by Strong-Field Ionization

4.1 Introduction

The Jahn-Teller (JT) theorem[191] states that degenerate electronic states in non-linear molecules cannot be minima of energy vs nuclear positions, and will therefore undergo nuclear displacements that break the degeneracy. This is often observed in highly symmetric molecules with partial occupation of symmetry equivalent orbitals. A prototypical example of JT distortion is $CH_4{}^+$, which arises from ionization from the triply degenerate highest occupied molecular orbital (HOMO) of CH_4. The resulting cation rapidly distorts away from the tetrahedral (T_d) geometry of the neutral to a C_{2v} symmetry structure[192, 193] with two long and two short CH bonds. Baker et al. have attempted to measure the time required for the JT process via comparison of high harmonic generation in $CH_4{}^+$ to $CD_4{}^+$, where they report a difference between the geometry relaxation times of the two molecules up to 1.6 fs, but could provide no further information[194]. Recently, Gonçalves et al. calculated the JT timescale in $CH_4{}^+$ and found that distortion to C_{2v} occurs as early as 7 fs, while the heavier $CD_4{}^+$ takes longer to relax to the same structure[195].

Ionization of halogenated methanes is expected to lead to slower (and thus easier to measure) JT distortion, on account of the larger substituent masses. However, JT distortion has not been observed for such systems, as the resulting cations are quite short-lived and therefore difficult to study[196]. Indeed, it has been assumed that dissociation of the T_d conformation of $CCl_4{}^+$ to $CCl_3{}^+$ and Cl occurs without any intermediates[197, 198], as no stable ion is produced by direct photoionization[199]. Theoretical work[198, 200] has suggested a stable structure of the form $[Cl_3C{-}{-}{-}Cl]^+$, with one Cl 3.5 Å away from the C and weakly coordinating to it. However, there are no experiments that validate the existence of these possible $CCl_4{}^+$ complexes.

The instability of $CCl_4{}^+$ necessitates the use of a technique that is sensitive to changes in nuclear and electronic structure occurring within the first few femtoseconds after formation.

X-ray Transient Absorption Spectroscopy (XTAS) is such a method, as its time resolution is only limited by the duration of the pump and probe laser pulses and femtosecond resolution is readily achievable[72, 73, 91]. Following strong-field ionization by the pump, the X-ray pulse induces transitions from core levels to unoccupied orbitals, which ensures that XTAS is sensitive to the local environment of individual atoms in the probed molecular system[24, 72]. It is therefore well suited for probing possible JT distorted transient intermediates that may arise during a dissociation. Indeed, XTAS has previously been used to infer JT distortion in the benzene cation[84] and ring opening in cyclohexadiene[60]. Pertot et al.[21] also employed XTAS at the C K-edge to study the dissociation of CF_4^+, reporting rapid dissociation to CF_3^+ and F within ∼40 fs.

While several aforementioned studies focused on the C K-edge, HHG X-ray pulses span a relatively broad energy range[43, 91, 95] and can be used to study multiple atomic edges simultaneously. In particular, the Cl $L_{2,3}$-edge ($2p$ levels, ∼195-220 eV) is a natural complement to the C K-edge ($1s$ level, ∼280-300 eV) for studying chlorinated methanes. Signal from two elements potentially allows for the identification of species whose spectra might be unresolvable or involve forbidden transitions at any one particular edge. It also permits observation of any Cl dissociation both from the perspective of the departing atomic Cl species and the remaining C-containing molecular fragment.

Below, the results are presented of a time-resolved experimental and theoretical investigation of strong-field ionized CCl_4, by tabletop XTAS simultaneously at both the C K-edge and the Cl $L_{2,3}$-edge. Evidence is shown for an overall dissociation pathway of CCl_4^+ that is initiated by an ultrafast (∼6 fs) JT distortion driven symmetry breaking, away from the parent tetrahedral (T_d) geometry to an ensemble of Symmetry-Broken Covalently Bonded (SBCB) structures where all four Cl atoms remain covalently bonded to C. All SBCB forms can be viewed as vibrationally excited C_{2v} CCl_4^+, as this geometry is predicted by theory to be the only stationary point on the cation potential energy surface with four C-Cl covalent bonds. Theory further indicates that the ions are only temporarily trapped in the SBCB form, based on *ab initio* quasiclassical trajectory (QCT) calculations and computed X-ray spectral features from orbital optimized density functional theory (OO-DFT[178]) that can be directly compared to experiment. The experiments corroborate the computed spectral features and identify the timescales for the initial symmetry breaking. Similarly, experiment and theory synergistically describe the evolution of the transient SBCB cation to a non-covalently bound complex (NBC) between CCl_3^+ and Cl. The latter structure ultimately undergoes irreversible dissociation over relatively long timescales (∼ 800 fs). The overview of the calculated pathways for JT distortion and dissociation are summarized in Fig. 4.1. There is also evidence for a higher energy channel that results in CCl_3 and atomic Cl^+.

4.2 Methods

The tabletop experimental apparatus was previously described in Chapter 2. The pump pulse for this experiment that induces strong-field ionization (SFI) is centered at 800 nm,

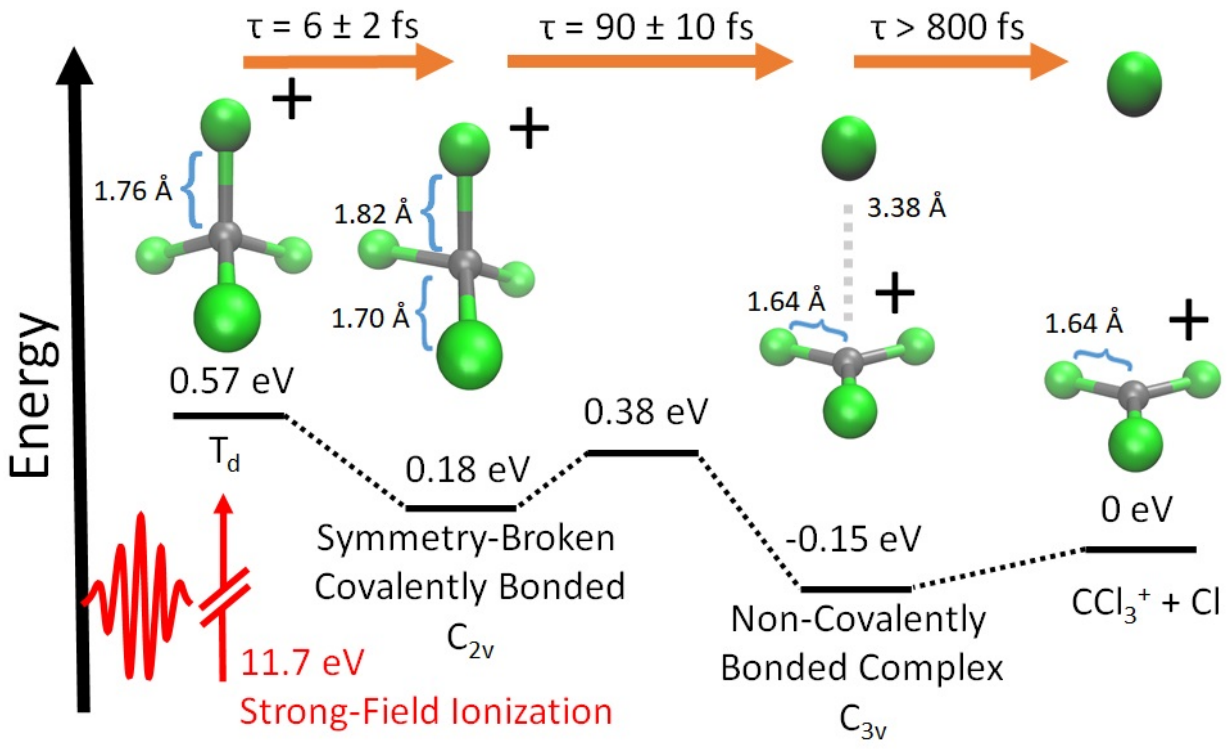

Figure 4.1: The sequence of intermediates for the dissociation of CCl_4^+ identified in this experiment. Geometries were optimized with ωB97M-V[175]/aug-pcseg-3[176]. Zero-point energies were computed at the same level of theory. Electronic energies at these geometries were subsequently found using CCSD(T)[177] extrapolated to the complete basis set (CBS) limit. The structures of the closest local minima are used for the symmetry-broken covalently bonded form and non-covalently bonded complex; although, the experiment samples a large range of nuclear configurations, due to vibrational energy. The energy is set to 0 for the dissociated ion. Time constants shown are gathered from the ΔOD data in Fig. 4.2b and c and their lineouts.

spectrally broadened, and compressed to about 6 fs in duration. The maximum energy of the compressed pulse at the sample is 150 μJ at 1 kHz repetition rate. It is focused to 65 μm full width at half maximum (FWHM) to achieve an electric field with peak intensity up to $3 \pm 1 \times 10^{14}$ W/cm^2. The probe are X-rays with energies up to 370 eV. The X-ray monochromator has 0.2 eV spectral resolution at the C K-edge Experiments are performed over different time ranges to cover a wider range of dynamics; the shortest have a step size of 1 fs and extend to 80 fs, and the longest have variable step sizes and extend to 10 ps. Additionally, experiments are run with varying pump power, from $\sim 1 - 3 \times 10^{14}$ W/cm^2, to assess how the power affects the temporal dynamics and final states. These

scans are taken as closely in time as possible to make the comparisons between scans more consistent. Timescales are extracted by fitting lineouts to exponential functions. Each fit includes convolution with a Gaussian of 8 ± 2 fs FWHM to account for the cross-correlation of the experiment, using the 95% confidence intervals as error bars. CCl_4 was obtained from Sigma-Aldrich at 99.5% purity and was vaporized by exposing the liquid to vacuum.

To better explain the features, a collaboration with theoretical chemists was made, and this work has a good description of the processes thanks to the work of Diptarka Hait, in the Martin Head-Gordon group at University of California - Berkeley. Quantum chemical calculations were performed with the Q-Chem 5 software [174]. Structures were optimized with the ωB97M-V[175] density functional and the aug-pcseg-3[176] basis set. Zero-point energies were found at the same level of theory. Relative ground state electronic energies at the optimized geometries were computed with CCSD(T)[177] extrapolated to the complete basis set (CBS) limit. *Ab initio* trajectory calculations on $CCl_4{}^+$ were performed with ωB97M-V/aug-pcseg-1, starting from the equilibrium CCl_4 T_d structure and with quasiclassical velocities[201] for nuclei (this ensures each normal mode of the neutral species has the associated zero point energy). A total of 256 trajectories (out of the 512 possible ones) were run. The trajectory calculations did not incorporate an external electric field, and thus can only provide a first estimate of timescales that can be compared to experiment.

X-ray absorption spectra were simulated with OO-DFT[178], utilizing the SCAN[179] functional, aug-pcX-2 basis[183] on the site of core-excitation, and aug-pcseg-2 basis[176] on all other atoms. This approach has been shown to be accurate to $\sim$0.3 eV root-mean-squared error for the core-level spectra of electronic ground states of both closed-shell[133] and open-shell[180] species, without any need for empirical energy translation of the spectra. Refs 133 and 180 provide detailed protocols for running OO-DFT calculations. Excited state orbital optimization was done with the square gradient minimization (SGM[181]) and initial maximum overlap method (IMOM[182]) algorithms, for restricted open-shell and unrestricted calculations, respectively.

4.3 Results and Discussion

General Features of Experimental Spectrum

The ground state static spectrum of CCl_4 is presented in Fig. 4.2a. The Cl $L_{2,3}$-edge is comprised of a number of peaks, several of which overlap, largely due to the Cl $2p$ spin-orbit splitting of 1.6 eV. The dominant features correspond to excitations to the $7a_1^*$ and $8t_2^*$ symmetry adapted linear combinations (SALCs) of σ^*_{CCl} antibonding orbitals. Transitions from the L_3 ($2p_{3/2}$) level to $7a_1^*$ and $8t_2^*$ occur at 200.4 eV and 203.2 eV respectively[167]. The corresponding L_2 ($2p_{1/2}$) transitions occur at 202.0 eV and 204.8 eV. All of these excitations are dipole allowed. Transitions to Rydberg levels lead to additional peaks, and a rising ionization edge begins and persists around 207.5 eV. The L_3 ionization energy of CCl_4 from X-ray photoelectron spectroscopy is 207 eV[202].

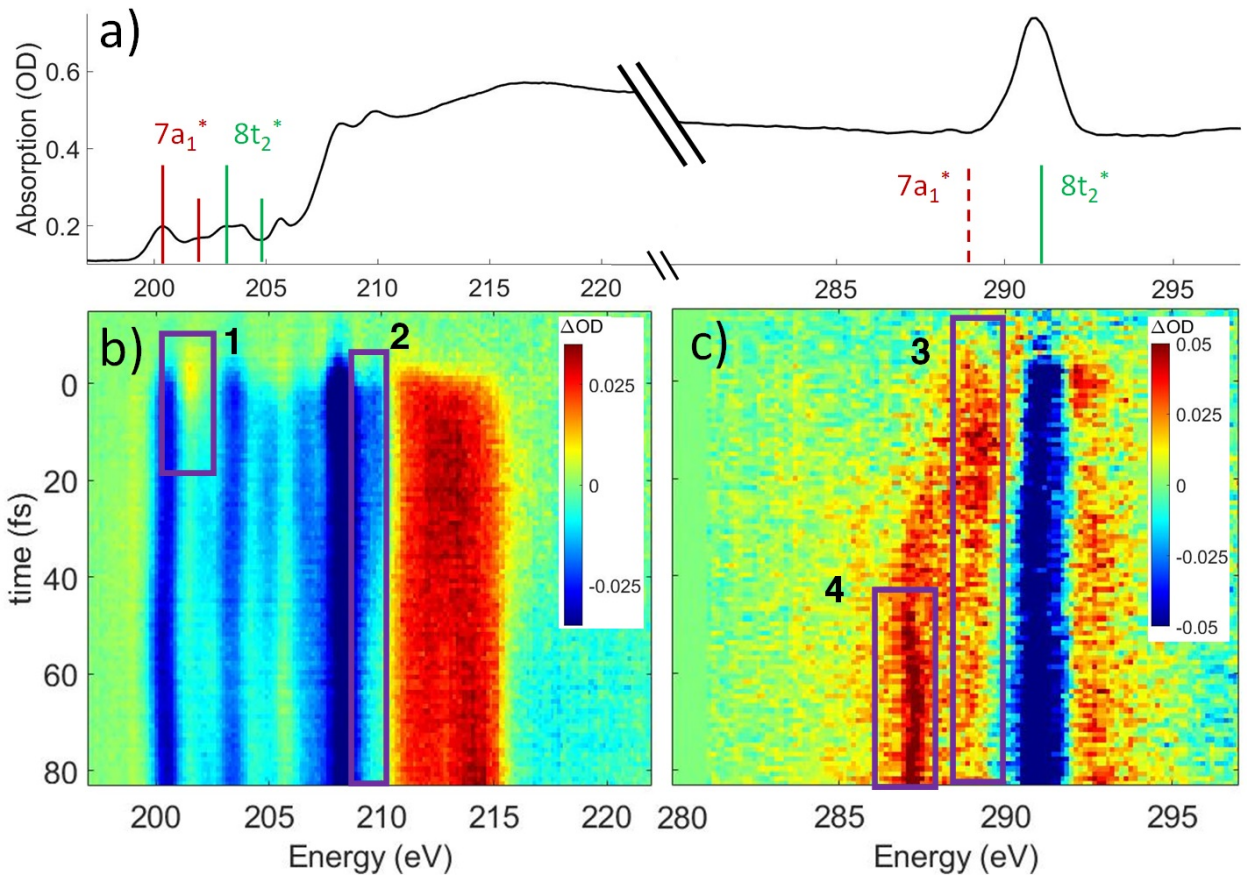

Figure 4.2: a: Static absorption spectrum of neutral CCl_4 at the Cl $L_{2,3}$- and C K-edges, dominated mostly by transitions to the singly degenerate $7a_1^*$ and triply degenerate $8t_2^*$ levels. The C $1s \rightarrow 7a_1^*$ is transition is dipole forbidden, and absent in the static spectrum. b & c: ΔOD data from the highest pump power ($\sim 3\times10^{14}$ W/cm^2) for the Cl $L_{2,3}$-edge (b) and C K-edge (c). Positive time corresponds to 800 nm pump first, while negative time is X-ray probe first. Negative ΔOD represents depletion of neutral CCl_4, while positive ΔOD features indicate presence of new species that absorb stronger than the parent in that region. Prominent transient features are labeled 1 (201.7 eV), 2 (209.5 eV), 3 (289.2 eV) and 4 (287.1 eV). A discussion of the features and their assignments is presented in the text.

In contrast, the C K-edge spectrum of neutral CCl_4 consists of a single intense peak at 290.9 eV[171], followed by a rising edge at $\sim$295 eV. The 290.9 eV peak arises from the C $1s \rightarrow 8t_2^*$ excitation, as the transition to the lower energy $7a_1^*$ orbital is dipole forbidden[171]. OO-DFT predicts the C$1s \rightarrow 8t_2^*$ excitation to be at 290.8 eV, in excellent agreement with experiment, and the forbidden C$1s \rightarrow 7a_1^*$ transition at 289.0 eV. There is also significant absorption from the tail of the chlorine edge in the experimental spectrum, which reduces

the signal-to-noise at the C K-edge.

Strong-field ionization by the pump pulse induces dynamics that leads to differences in absorption (ΔOD), as shown in Fig. 4.2b & c. The many spectral overlaps at the Cl edge (Fig. 4.2b) make it difficult to identify individual signals in the ΔOD data. Negative signal from ground state bleach is predominant from 200 to 210 eV with positive signal appearing in the 211-216 eV range, possibly due to a positive local charge on the chlorines leading to a net blue shift. The C edge is easier to resolve, with only a ground state bleach at 290.8 eV, and positive absorption at both higher ($\sim$ 292 eV) and lower (287-290 eV) energies.

Within these broad signals, several notable features can be observed. The first is a small positive feature at the Cl edge, labeled feature 1 in Fig. 4.2b. This feature only appears transiently at early times and rapidly decays within a few femtoseconds. The second is at 209.5 eV, feature 2, which initially drops to a negative ΔOD but decays back towards zero values on the timescale of 100 fs. A similar timescale is observed in the decay of feature 3, at 289.2 eV, which suggests that the two decays measure the same process. Additionally, the positive signal of feature 3 initially rises on the same time scale as the decay observed in feature 1, suggesting that the early time behavior of features 1 and 3 reflect the same process. A fraction of feature 3 undergoes a continuous evolution (289.2 to 287.1 eV) to feature 4 at 287.1 eV after $\sim$20 fs. Feature 4 continues to grow after that time, concurrent with the decay of feature 3. Finally, at delays of several hundred femtoseconds to a few picoseconds, much longer times than those shown in Fig 4.2, a series of sharp spectral features between 204 and 207 eV become resolvable from the broader features, shown more clearly in a later section.

Based on the three timescales involved in the evolution of the noted features, few-femtosecond, tens of femtoseconds, and several hundred femtosecond, it is reasonable to conclude that three separate processes are responsible for the dynamics of the dissociation of CCl_4^+. In order to better understand the nature and quantitative times of these processes, these features are averaged and fitted along the time axis, and assignments are made by comparison to theory, as discussed below.

General Considerations for C K-edge

Any distortion away from T_d geometries would alter the symmetry of the σ^*_{CCl} levels, which would no longer form the $7a_1^*$ and $8t_2^*$ SALCs. The most general symmetry-broken case would be of C_1 symmetry, with four unequal bond lengths. This leads to four nondegenerate σ^* levels that permit dipole allowed transitions from the C $1s$ level, although intensities will be lower for the MOs with greater C $2s$ character. The shorter bonds would feature stronger C-Cl interactions, leading to higher energy σ^* MOs, while the longer bonds would conversely lead to lower energy σ^* levels. In particular, the lowest energy σ^*_{CCl} level is expected to be dominated by the longest C-Cl bond, and therefore the lowest energy C K-edge feature in the transient absorption spectrum should correspond to this bond. Conversely, the shortest bonds should lead to the highest energy absorption feature. More symmetric configurations can permit multiple bonds to make comparable contributions to any given σ^* MO, preventing

assignment of a transition to one particular bond. In general, however, the longest bonds should lead to the lower energy features in the C K-edge spectrum, while the higher energy features should arise from shorter bonds. However, there is no such simple rule of thumb available for the Cl L-edges, due to the complexity of the spectrum.

Jahn-Teller Distortion of CCl_4^+

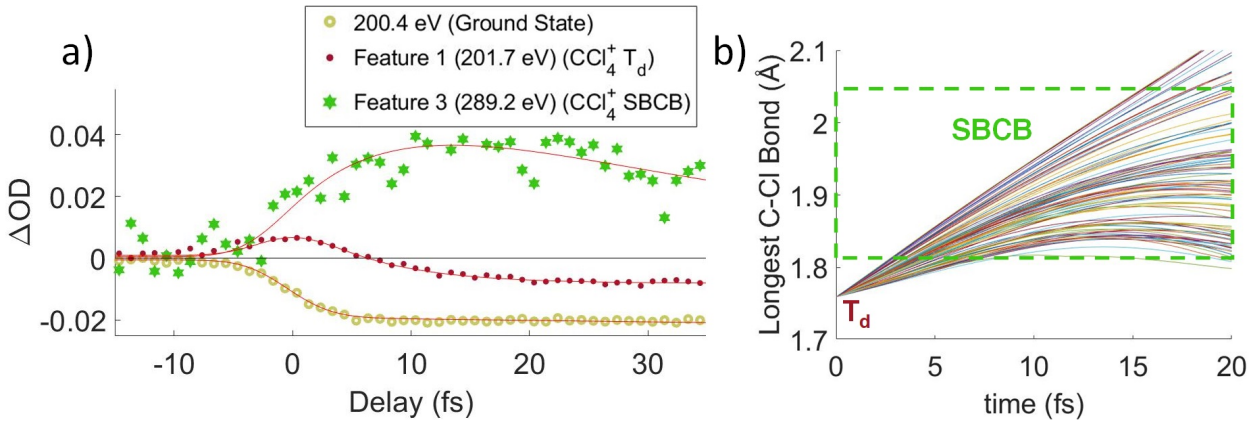

Figure 4.3: a: Averaged lineouts of features 1 and 3 in the first 35 fs. Fitting including the 8 ± 2 fs cross-correlation gives a lifetime of 6 ±2 fs and 7 ± 3 fs for the decay and rise of features 1 and 3, respectively. b: The longest C-Cl bond length for a set of 100 trajectory calculations, because that bond will correspond to the lowest energy absorption at the C K-edge. It shows that the bond elongates into the SBCB region rapidly, assisting the assignment that feature 1 corresponds to the T_d.

Lineouts of the few-femtosecond process are shown in Fig. 4.3a. These shows decay of feature 1 in 6 ± 2 fs and the rise of feature 3 in 7 ± 3 fs. These lifetimes, along with those extracted from the other fits, are compiled in Table 4.1. The ground state bleach at 200.3 eV from depletion of the neutral CCl_4 represents the instrument response function (i.e., the temporal broadening introduced by the experiment). Comparison to the ground state bleach in Fig. 4.3a show these lifetimes are significant beyond the experimental cross-correlation.

The lowest vertical ionization energy of CCl_4 is 11.7 eV[203], corresponding to loss of an electron from the non-bonding t_1 SALC of Cl 3p orbitals and forming the cation X state[199, 203, 204]. Making the assumption that the SFI process abruptly populates a CCl_4^+ cation state or states in a Franck-Condon-like manner, those states then undergo geometry changes. The states may also have significant internal vibrational excitation. The electron hole is delocalized over all four Cl atoms in the T_d geometry, and the computed C K-edge XAS is consequently quite similar to neutral CCl_4. None of the features of the C K-edge experimental spectrum can therefore be unambiguously assigned to T_d CCl_4^+. At

Feature # Energy (eV)	Assigned Transition	Time Constant, τ ($e^{-1/\tau \times t}$) (fs)
1 (201.7 eV)	$T_d \rightarrow$ SBCB	6 ± 2
3 (289.2 eV)	$T_d \rightarrow$ SBCB	7 ± 3
2 (209.5 eV)	SBCB $\rightarrow$ NBC	90 ± 10
3 (289.2 eV)	SBCB $\rightarrow$ NBC	80 ± 30
4 (287.1 eV)	NBC Appearance	τ: 50 ± 20 Delay: 23 ± 8
204.2, 206.6 eV	Atomic Cl Appearance	800 ± 200
214.7 eV	Cl^+ Appearance	τ: 85 ± 10 Delay: 37 ± 6

Table 4.1: Time constants for each of the fits shown in the figures.

the Cl $L_{2,3}$-edges, the hole density should blue shift the absorption spectrum[26], so feature 1 is assigned to T_d CCl_4^+.

From theory, the closest local minimum to the T_d starting structure is a C_{2v} symmetry distorted tetrahedron with two long (1.82 Å) and two short (1.70 Å) C-Cl bonds. The calculations indicate that a C_{2v} form of CCl_4^+ is lower in energy by 0.4 eV, and there is no energy barrier between this minimum and the initial T_d geometry. This energy stabilization is smaller than the 1.5 eV stabilization observed for the analogous CH_4 structure[193]. This result is unsurprising as the CCl_4 ionization is from Cl lone-pairs while the CH_4 electron loss is from bonding orbitals. The energy stabilization from JT distortion will be available to the vibrational modes of the ion, so many different nuclear configurations will be accessible around the C_{2v} local minimum configuration. This range of configurations will be referred to as the Symmetry-Broken Covalently Bonded (SBCB) form of CCl_4^+.

The OO-DFT C K-edge spectrum of the C_{2v} stationary point was computed in order to determine if SBCB forms were contributing to feature 3. At the C_{2v} stationary point, all four σ^* SALCs are nondegenerate and the C $1s$ transitions to these SALCs are all formally dipole allowed. The two lower energy SALCs correspond to the long C−Cl bonds, which is computed to lead to absorption at 289.8 eV, and the shorter bonds lead to higher energy σ^* SALCs that are computed to absorb at ∼292 eV. A comparison of these energies in Fig. 4.4a with the absorption of feature 3, corrected for ground state bleach, shows that the energies match well. This validates the assignment that feature 3 arises from distorted CCl_4^+ with four covalent bonds.

In order to get an idea of the timescales of this distortion, Fig. 4.3b shows the longest C-Cl bond distance for a random subset of 100 calculated trajectories. The longest C-Cl bond is used here as a measure of distortion away from T_d, for best comparison to the experimental X-ray absorption.It shows that at least one C-Cl bond rapidly elongates to the C_{2v} value of 1.82 Å at ∼5 fs on average. The ∼5 fs time from the trajectories is comparable to the 6 ± 2 fs

decay of feature 1 and the 7 ± 3 fs rise of feature 3. Both time constants should measure the same process, the lifetime of the CCl_4^+ T_d geometry, with feature 1 more directly measuring the decay of the initial T_d state and feature 3 measuring formation of the distorted state. They confirm the rapidity of the JT process and the barrierless energy surface between the two. The JT distortion is faster than any of the normal vibrational modes of CCl_4, the fastest of which has a period of 43 fs[169]. On changing the pump intensity, the lifetimes exhibited no power dependence beyond what is necessary for ionization within the error bounds.

Covalent Bond Breakage of CCl_4^+

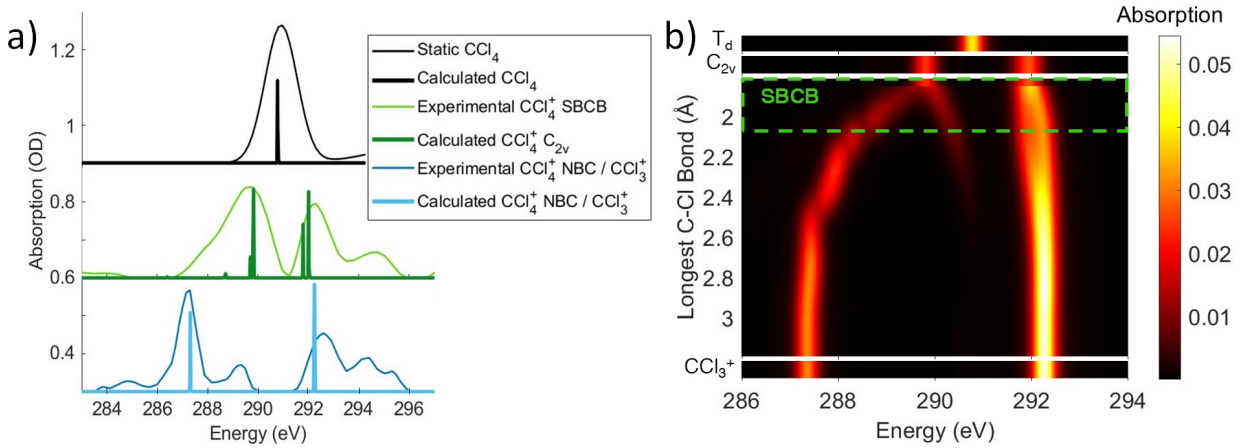

Figure 4.4: a: The experimental features 3 and 4 as well as the neutral static are disambiguated and corrected for ground state bleach to obtain an absorption spectrum, using a method described in Section 3.2. Notably, this shows that feature 3 ΔOD signal at 289.2 eV corresponds to an actual maximum at 289.8 eV. These spectra are compared to OO-DFT calculations for energies and oscillator strengths of the excitations (given by the peak position and heights, respectively). This allows for assignment of feature 3 to the SBCB form and feature 4 to the NBC or CCl_3^+ moeity. b: OO-DFT absorption spectra for various CCl_4^+ geometries. The third plot from the top shows absorption as a function of a single increasing bond distance (and other nuclear coordinates being optimized with this constraint). This shows splitting of absorption energies with the lower energies corresponding to the longest bond and higher energies to the shortest. The region of maximum bond extension without cleavage is shown in the SBCB region. These longer bonds account for the low energy tail in the SBCB experimental spectrum.

The evolution of some fraction of feature 3 to the much lower energy feature 4 in the experimental spectrum suggests further C-Cl bond stretching. OO-DFT calculations confirm this, with Fig. 4.4b showing the absorption of energy in CCl_4^+ as a function of the

longest C-Cl bond distance (with all other nuclear coordinates being optimized). Fig. 4.4b further explains the lower energy tail of the experimental SBCB spectrum in Fig 4.4a, as the experiment will sample many molecules spanning a wide range of SBCB geometries.

Feature 4 at 287.1 eV absorbs at the same energies as an extremely elongated C-Cl distance ($\sim$ 3 Å) in Fig 4.4a and b, suggesting that feature 4 corresponds to a CCl_3^+ moiety. This is consisent with the theoretical prediction that the lowest energy forms of CCl_4^+ are noncovalently bonded complexes (NBCs) between atomic Cl and CCl_3^+. The global energy minimum of CCl_4^+ is an NBC with approximately C_{3v} symmetry, a nearly planar CCl_3^+ moiety having a Cl atom vertically above the C, at a distance of 3.4 Å. A C_s symmetry minimum with the atomic Cl coordinating to a bonded Cl in the CCl_3^+ moiety is also found at 0.02 eV above the NBC minimum, with a Cl-Cl distance of 3.24 Å. Given the only slight energy preference for the minimum energy position of the Cl in the NBC and the available vibrational energy, it is likely that the Cl does not stay at this position under experimental conditions and instead samples a wide range of locations around CCl_3^+. However, the experiment is not directly sensitive to the position of the noncovalently bound Cl. The large distances between CCl_3^+ and Cl for all such species in fact indicate that C K-edge transitions to valence orbitals would be essentially unaffected by the particulars of the noncovalent interaction.

An energy decomposition analysis (EDA[205]) calculation reveals that the -0.15 eV interaction energy between atomic Cl and CCl_3^+ in the minimum energy NBC geometry is mostly (56%) from the polarization of the atom by the cation, with a much smaller amount (19%) arising from charge-transfer (the remaining 25% being permanent electrostatics, Pauli repulsion and dispersion). The system effectively acts as a charge-induced dipole complex. It is also worth noting that these NBC structures do not have any covalent Cl-Cl interactions, contrary to some early assignments[206–208].

The timescale of the SBCB to NBC transition is shown through lineouts of features 2, 3, and 4 in Fig. 4.5a. This shows decay times of features 2 and 3 in 90$\pm$10 fs and 80$\pm$30 fs, respectively. Feature 4 appears only after a delay of 23$\pm$8 fs, which implies that the nuclear motions take at least 23 fs to get to the point that the ion starts to resemble its dissociated form. After this delay, it has an additional lifetime of 50$\pm$20 fs to reach its asymptotic value. Because of the delay from nuclear movement, the experimental time for the SBCB to NBC process is taken from the more precise feature 2, 90$\pm$10 fs, and no pump power dependence is observed. This time is expected to be significantly longer than the JT distortion due to the computed barrier of 0.2 eV for this process. In varying the pump power, no difference is observed in the SBCB decay times, possibly due to the large intensity already required to ionize the CCl_4.

The trajectory calculations in Fig. 4.5b show that a portion of the ions continue their initial distortion and dissociate immediately, which is observed experimentally by the direct evolution of the feature 3 $\rightarrow$ feature 4 signal. Another portion remains trapped in the SBCB form for longer than a vibrational period, showing longest C-Cl distances between 1.8 and 2.05 Å, which serves to define the SBCB region. Note that the trajectory calculations show a significant population persisting in the SBCB form for a longer time than the experimen-

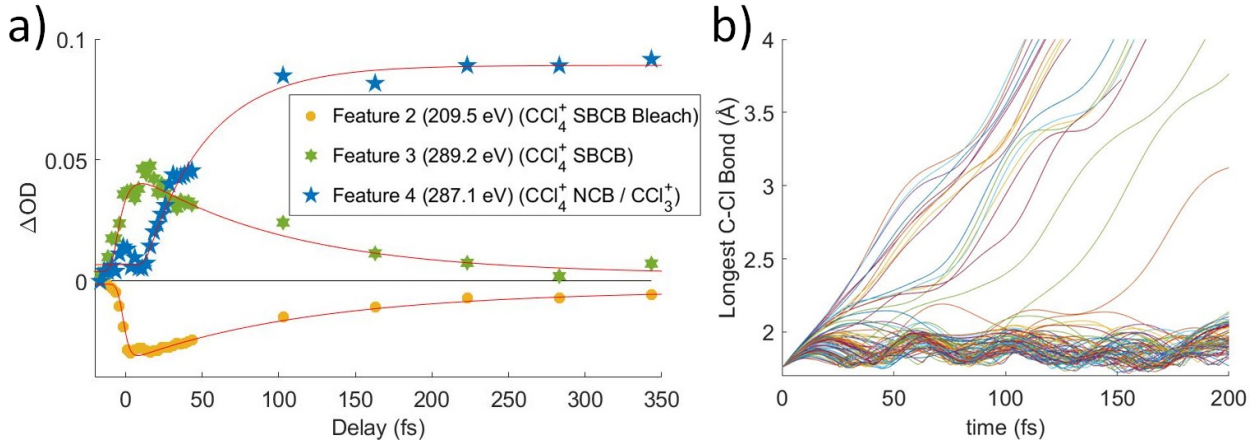

Figure 4.5: a: Averaged lineouts of features 2, 3, and 4 out to 350 fs. Fitting gives decay times of features 2 and 3 in 90±10 fs and 80±30 fs, respectively. Feature 4 appears only after a delay of 23±8 fs, followed by an exponential of 50±20 fs. b: A set of 100 trajectory calculations, showing the longest C-Cl bond distance. It shows a population that temporarily remains the in SBCB with longest bonds going between 1.8 and 2.05 Å. It also shows a portion of ions have sufficient velocity in the appropriate chlorine to break the C-Cl covalent bond immediately, while others require additional time to redistribute the energy such that the bond may be broken. The trajectories show more population remaining in the SBCB form for longer, but the difference is likely due to excess vibrational energy in the experiment or another particular of the strong-field ionization, which are not included in the trajectories.

tally measured lifetime. This likely arises from the trajectory calculations not including the excess vibrational energy added by the pump pulse. The calculations only include the zero-point energy of neutral CCl_4, leading to the SBCB form persisting longer than what is experimentally observed.

Atomic Cl Dissociation

Although the C K-edge cannot distinguish between NBC and free Cl, the Cl $L_{2,3}$ edge can make this distinction, as atomically sharp Rydberg lines corresponding to atomic Cl become evident upon completion of the dissociation, which is shown in Fig. 4.6a and b. Very little change is observed in the ΔOD spectra between 250 fs and 3.5 ps at either the C K-edge or chlorine $L_{2,3}$-edge, other than the appearance of these sharp lines, which is consistent with the previous assignment of the NBC form. While weakly bound in the NBC, the atomic lines are broadened by a combination of two factors. Firstly, the transitions are already of low intensity due to their Rydberg character, the lowest energy lines being of $2p \rightarrow 4s$ character. Secondly, the diffuse nature of the Rydberg levels mean that the excitation energy would be sensitive to the precise position of the CCl_3^+ entity, and the flatness of the NBC ground state

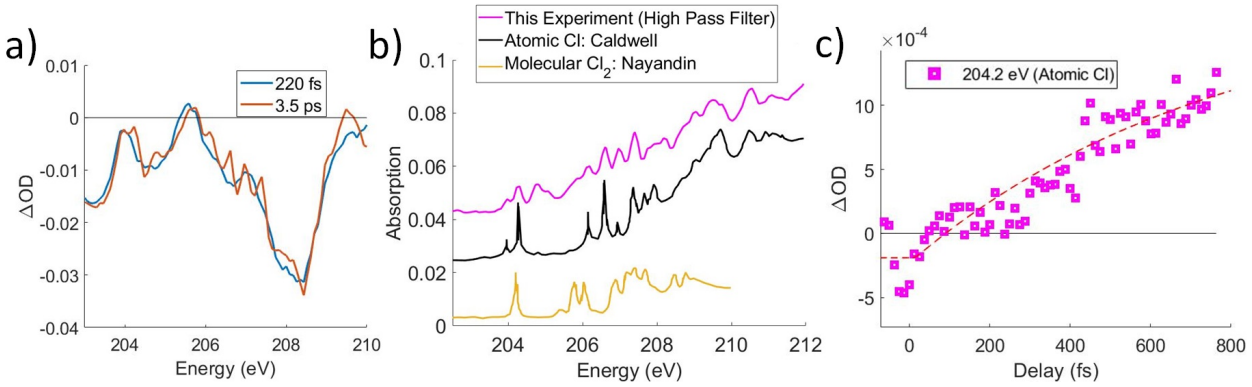

Figure 4.6: a: Lineouts in energy for 220 fs and 2.5 ps at the Cl $L_{2,3}$-edges. They show that although the overall shape and intensity of the ΔOD signal remains constant, sharp spectral features appear at longer delays. The difference between 3.5 ps and 220 fs is taken and added to an error function to obtain the spectrum in b. b: A comparison of the sharp spectral features is made to atomic Cl[209] and to molecular Cl_2[210], which shows that the features match well with atomic Cl. c: A high-pass spectral filter is applied to the ΔOD data and an average of the two most prominent lines at 204.2 and 206.6 eV are a lineout is shown against time. A fit is taken starting from t=0, due to noise preventing a better determination of a start point. This fit with $\sim 3\times10^{14}$ W/cm^2 pump intensity has a lifetime of 800 ± 200 fs.

potential energy surface permits a large range of accessible nuclear configurations. However, over time, the atomic Cl irreversibly dissociates, leading to atomic Cl lines appear at 204.5 eV and upward from 206 eV, which agrees with previous experimental absorption data[209]. Thus, the Cl atomic lines can be used to track the time it takes for the NBC species to completely dissociate to CCl_3^+ and Cl. While molecular Cl_2 has absorption in this energy range as well[210], comparison to experimental atomic absorbance in Fig. 4.6b shows much better agreement with atomic Cl.

A simple exponential fit of these lines in 4.6c gives a lifetime longer than 800 fs. The exponential starts at time zero, despite the Cl signal not clearly departing from 0 until ∼300 fs. This may correspond to the minimum time required for atomic Cl to move far enough to show the Rydberg lines, although the signal-to-noise of this experiment is not sufficient to make that distinction.

The 800 fs time scale is much longer than the 90 fs observed for NBC formation, despite the excess of energy available to the system. However, the interactions and thus rate of energy transfer between the CCl_3^+ moeity and the neutral Cl are much weaker than a covalent bond. This situation is similar to van der Waals complexes, which sometimes show lifetimes exceeding milliseconds with vibrational energy in the molecular moeity[211, 212]. The 800 fs value is the fastest Cl formation time and was measured from the most intense pump

pulse of 3×10^{14} W/cm^2. Datasets collected at lower pump power show slower dissociation times, and some do not exhibit significant atomic Cl formation up to 3 ps. The NBC signal from feature 4 at 287.1 eV is still present, suggesting that the strong-field ionization may be capable of forming long-lived NBC CCl_4^+ species; although times longer than a few ps were not measured. It has been observed that otherwise unstable parent ions can be generated by few-cycle strong field ionizing laser pulses, such as tetramethyl silane and CS_2[213, 214], and an analogous NBC may be a potential explanation of these signals. A quantitative comparison of the power dependence on this timescale was not carried out.

4.4 Additional Channel Leading to Cl^+ Formation

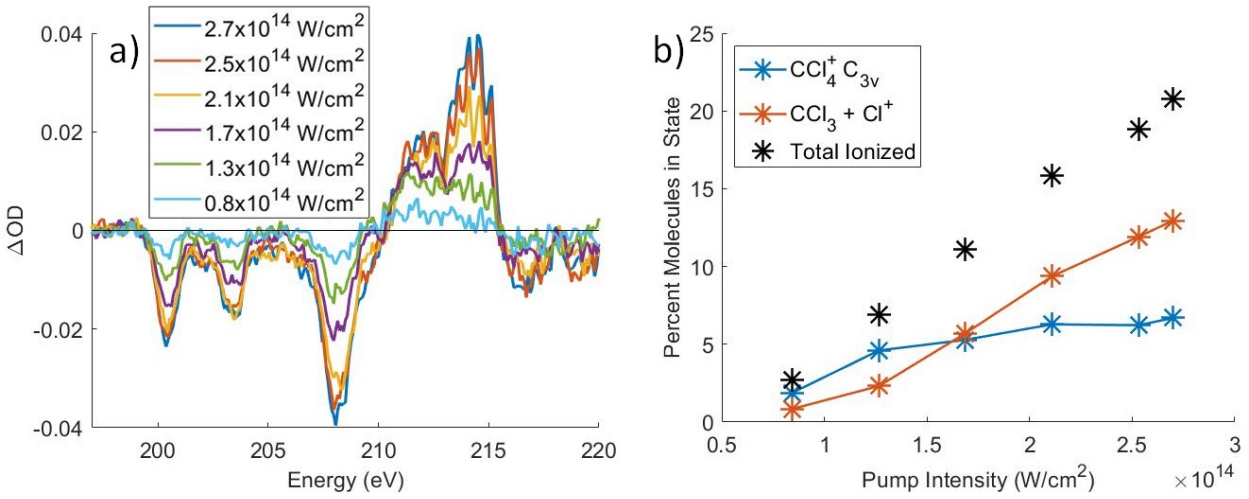

Figure 4.7: a: Spectral lineouts averaged from 190-230 fs as a function of increasing pump power, measured before the vacuum chambers and recombination mirror. Note that at high powers, the sharp lines at 214 eV corresponding to Cl^+ become increasingly prevalent. b: Percentage of molecules in each channel between generation of atomic neutral Cl or cationic Cl^+. The X-axis uses estimated intensities of the pump pulse, but the relative intensities are accurate. At the powers and pulse duration used, the amount of the neutral channel plateaus quickly and has only slight increases with increasing power, whereas the Cl^+ channel increases nearly linearly after $\sim 1.3 \times 10^{14}$ W/cm^2. At the highest power, the relative amounts of Cl and Cl^+ from CCl_4^+ dissociation are 35% and 65%, respectively.

While the dissociation to CCl_3^+ and Cl can be well explained by the intermediate forms and pathways discussed in the main manuscript, another channel that appears to result in neutral CCl_3 and cationic Cl^+ constitutes a significant part of our data. This channel is clearest at the chlorine $L_{2,3}$-edge where very sharp lines with similar widths to the atomic Cl

lines are observed at 214 eV with less obvious components at 212.6 eV, shown in Fig. 4.7, which is the range that our ab initio calculations predict for the Rydberg states ($2p \rightarrow 3d, 4s$) of Cl^+. These atomically sharp peaks begin to appear with a delay of 37±6 fs relative to the onset of the main cationic CCl_4 signal, and from that point, it shows a time to grow in of 85±10 fs for the best signal-to-noise dataset. For the intensity scan, these dissociation times are found to be 70±40 fs, 94±94 fs, and 229±559 fs, for 2.3, 1.8, and 1.3 $\times 10^{14}$ W/cm^2, respectively. This suggests the dissociation times of Cl^+ have a slight dependence on pump intensity; although, uncertainties in the data do not allow a quantitative analysis. The delay of 37 fs is similar to the delay of 23 fs delay of the 287.1 eV NBC signal to start appearing, which suggests that the time it takes for a Cl^+ atom to move far enough from the molecule to show atomic lines is about that time ∼37 fs, and that the nuclear motion may be similar to the case that forms neutral Cl.After this delay, there is the somewhat long exponential time of 85±10 fs for the lines to reach their maximum value, which may suggest the presence of a shallow energy minimum, possibly corresponding to a NBC complex, before complete dissociation. The Cl^+ lines appear at much earlier times than Cl lines for two possible reasons. Firstly, the 3d and 4s levels of the cation have greater valence character due to the positive charge, leading to stronger absorption that is harder to broaden into the baseline. Secondly, the associated CCl_3 moiety for this pathway is neutral, and thus plays less of a role in influencing the energy levels of Cl^+ than CCl_3^+ does for Cl.

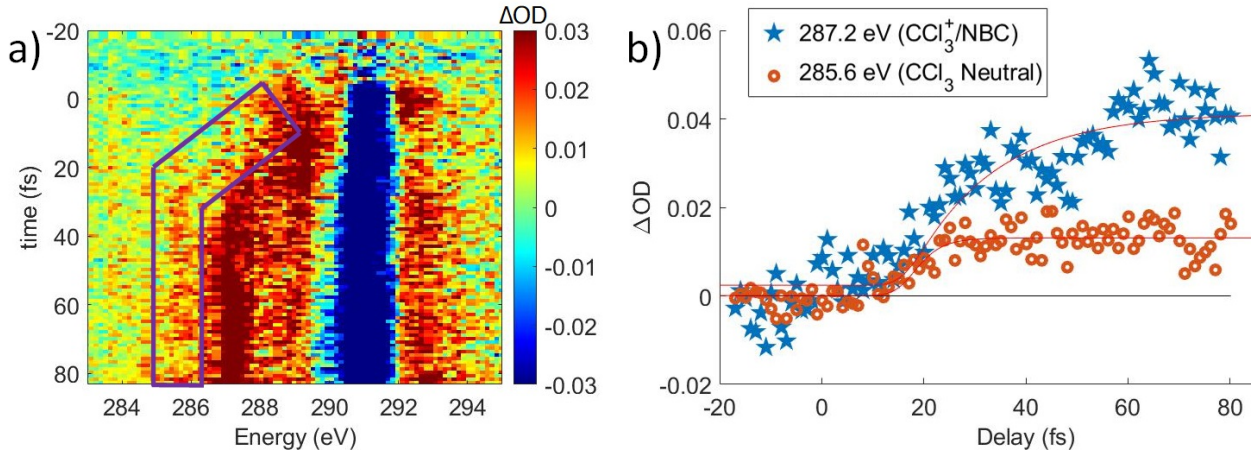

Figure 4.8: a: ΔOD colormap at C K-edge with colors saturated to better show a feature that splits from the main feature and continues to 285.5 eV. b: Lineouts comparing the growth of the 287.2 eV CCl_3^+/NBC feature to the 285.5 eV feature, which is assigned to neutral CCl_3. The NBC lineout has a delay of 23 ± 8 fs and a rise time of 50 ± 20 fs. The CCl_3 lineout has a delay of 20 ± 10 fs and a rise time of 8 ± 6 fs.

At the C K-edge, evidence of this channel can also be seen in a feature that appears at 285.5 eV, shown in figure 4.8. OO-DFT calculations show CCl_3 is expected to have

absorption at 285.5 eV. It shows a delay in appearance of 20 ± 10 fs, followed by a rise time of 8 ± 6 fs. The delay is very similar to the 23 ± 8 fs delay in the NBC formation, again suggesting similar nuclear motion along the pathways. However, the much shorter rise time suggests that only the trajectories that dissociate immediately contribute to the Cl^+ formation pathway.

The formation of Cl^+ is a much higher energy channel, with final energies about 4.8 eV higher than the normal dissociation channel. Cl^+ formation has been observed in previous CCl_4 ionization experiments from both electron impact[215] and single-photon ionization[199, 216]. However, it was always found to be a minor channel, with an abundance of 0-5% around ∼ 20 eV ionization energy. A larger percentage of Cl^+, ∼36%, is observed in strong-field ionization[217], and in the power scaling shown in Fig. 4.7, this experiment observes more than 65% forming, with the difference from other results[217] likely arising from shorter pulse durations and higher intensities.

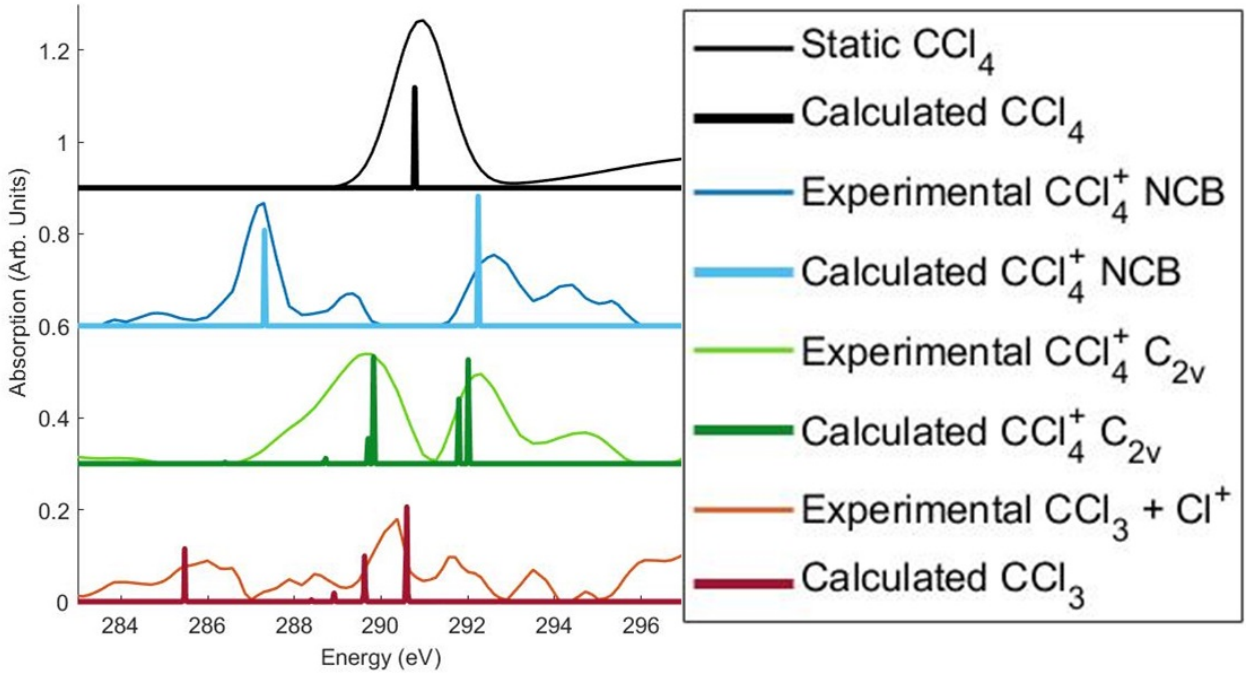

Figure 4.9: A comparison between experiment and theory, including neutral CCl_3, SBCB form, and NBC shows good agreement with each. The experimental curves are the result of the fitting method described in Section 3.2.

The final products, CCl_3 + Cl^+ are 4.8 eV higher in energy than CCl_3^+ + Cl, so the product supersystem is in an excited state, which can happen through two paths, crossing upward from the ground state of CCl_4^+ or dissociation starting on an excited state surface. The energy for crossing upward can in principle be available if there is significant vibrational

energy from Raman excitations during SFI to allow access to the crossing point. However, OO-DFT calculations spanning the nuclear parameter space appeared to suggest that the CCl_3 + Cl^+ channel is at least 1.5 eV above the ground state, which suggests there is no state crossing available to the ground state that leads to these products.

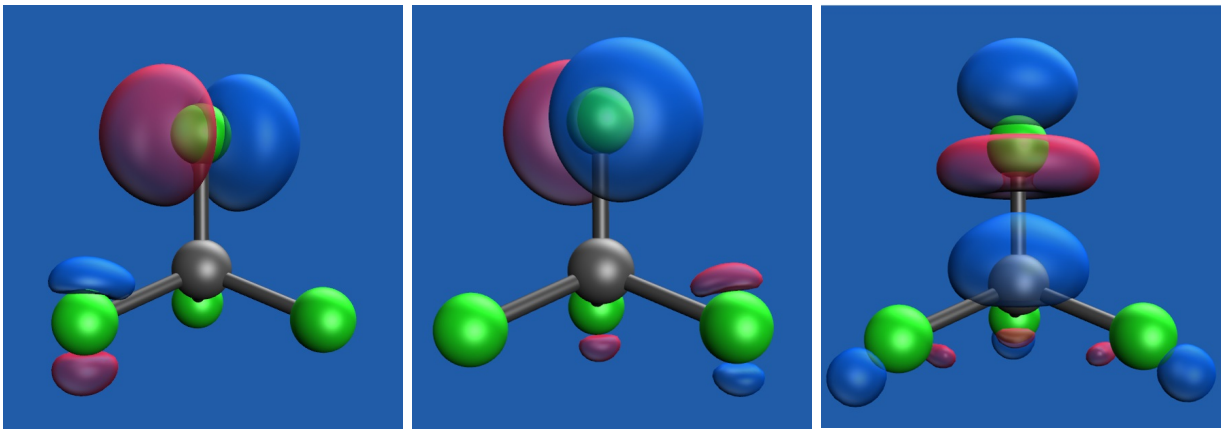

Localized lone-pair | Localized lone-pair | Localized σ^*_{CCl}.

Figure 4.10: ωB97M-V/pcseg-3 singly occupied orbitals for the lowest energy quartet state of CCl_4^+ at Franck-Condon region, with a 0.05 a.u. field aligned with the molecular axis. These orbitals are calculated by Diptarka Hait.

For an excited state, first consider the excited states formed by ionization from a deeper energy level, the X, A, B, C, etc. states from photoionization. Ionization from the T_2 and e symmetry Cl lone pair SALCs of neutral CCl_4 requires $\sim$ 12.5 eV and $\sim$ 13.5 eV energy respectively, corresponding to the A and B states [199]. Neither has enough energy to directly form Cl^+, being lower in energy than the products by 3.3 eV and 2.3 eV respectively. Ionization from the T_2 bonding orbital (the C state of the ion) requires $\sim$16 eV, indicating there is sufficient energy to form the final state. Photoionization experiments show that this is the energy where Cl^+ starts to form [199, 216]. However, Cl^+ is a very minor component of the data in those experiments. Furthermore, Diptarka Hait has calculated that there should be a strong absorption in the C K-edge associated with the C state of CCl_4^+ at 281 eV, as the ionization is from a bonding level and thus has significant contribution from the C atom. No such feature is present in our data, so this state is not likely. However, the field can also induce an excitation from the Cl lone pairs into an antibonding σ^*_{CCl} level, along with the ionization, leading to a state with three unpaired electrons that is inaccessible from photoionization. Populating the σ^* level should lead to faster bond cleavage, consistent with the fast 8 ± 6 fs rise time of the CCl_3 C K-edge signal. However, this channel should normally form neutral Cl as the SALCs are delocalized over all four Cl atoms, leaving no specific Cl with a large deficit of electrons. The equivalence of the Cl atoms however can be broken by the strong field, leading to both excitation and ionization happening from one local Cl site.

The positive charge on this double hole Cl site is stabilized by the electric field, and this atom becomes a precursor for Cl^+. DFT calculations with a field of 0.05 a.u. (corresponding to peak field strength of 1×10^{14} W/cm^2 intensity) aligned with a particular C-Cl bond indicate the viability of such a route, with the lowest energy quartet state of $CCl_4{}^+$ having two singly occupied levels that are holes on the targeted Cl and the remaining singly occupied level being the σ^*_{CCl} orbital localized along the field axis (as shown in Fig 4.10). This state can dissociate into CCl_3 and Cl^+, with the latter taking both of the electrons in the σ_{CCl} bond and leaving the σ^*_{CCl} electron on the C. While the field is only momentary ($\sim$6 fs) and oscillates in time (reversing sign after 1.3 fs), the duration may be sufficient to elongate one CCl bond to the extent that the charge stays localized on that Cl. Such a process would also be aided by Raman activation of the asymmetric stretch modes.

4.5 Summary

In this chapter, experimental and theoretical results provide evidence for both a transient Jahn-Teller distorted symmetry-broken covalently bonded $CCl_4{}^+$, similar to the stable ion of $CH_4{}^+$, and a potentially metastable form of $CCl_4{}^+$ as an noncovalently bound complex between $CCl_3{}^+$ and Cl. Neither of these intermediates have been observed previously in experiments. A summary of each of the time constants experimentally extracted is shown in Tab. 4.1. The transition from the initial tetrahedral ion to the C_{2v} state is found to be 6$\pm$2 fs, showing that the Jahn-Teller distortion is very fast, on the order of the duration of the pump laser pulse. It provides an order of magnitude estimate for other symmetric molecules undergoing JT distortion, which can aid chemical simulations as well as help predict the vibrational energies and nuclear dynamics of those other systems, especially given that this SBCB intermediate was not assumed to exist prior to this work[197, 198].

The NBC intermediate is bound largely by the polarization of the neutral species, forming an ion-induced dipole complex that lasts much longer than the time it takes for the covalent bond to break. The final dissociation time for free Cl or Cl^+ seems to be slightly dependent on the strong-field power, but for the highest power used in this experiment, the lifetime is more than 800 fs (vs 90 fs for NBC formation). This is a potential explanation for otherwise unstable parent ions appearing in mass-spectra of ultra-short strong-field ionization.

Additionally, a channel producing CCl_3 and Cl^+ has been found in large excess of expectations from previous electron impact and photoionization[216][215] experiments, with more than 65% of the final product going into this channel at the highest pump energy. W e hypothesize that this dissociation occurs from an excited state of the cation, wherein the strong applied field leads to localization of holes on a single Cl site.

Chapter 5

X-ray Spectroscopy in Solids

5.1 Introduction

Solids exhibit very different processes than those in molecules. Due to the extended network of atoms, the electronic energy levels cover a wide range of energies of accessible states, called the density of states (DOS)[218]. semiconductors are the cornerstone of the computing industry due to their ability to change their electronic characteristics[218]. The band gap of semiconductors are also ideal for absorbing light and is widely used in sensors and as switchable devices[219, 220]. Exciting semiconductors with light moves electrons from the valence band to the conduction band and leaves behind a positively charged hole[15]. The energy in the electron-hole exciton can be utilized in solar energy, so the time required to recombine the electron and hole matters for the amount of energy that can be extracted[15]. An excitation also leads to a number of effects on the ultrafast time scale, such as electron thermalization, band gap renormalization, or ultrafast depolarization[221–223]. Measurement of the various effects has many potential applications. X-ray spectroscopy is able to probe the holes and electrons separately from the core level, which can access more information about the dynamics and identification of other states that may play a role in the movement of electrons[224].

5.2 Static Absorption of Defect States in NV-Nanodiamonds

The NV center defect in diamond is a nitrogen substitution for a carbon that neighbors a missing carbon, also called a vacancy (NV = nitrogen-vacancy), and these are used in sensing and quantum computing applications[219]. They are made from a precursor of Nitrogen Center defects (P1, also called C-nitrogen center), which have a substituted nitrogen, but no neighboring vacancy. The samples examined are NV center nanodiamonds and precursor P1 nanodiamonds[225]. The concentration of NV centers can be determined by visible absorp-

tion, but the concentration of P1 centers is usually determined by electron paramagnetic resonance[226], and being able to count both has significant advantages, which has been shown with X-ray absorption[227]. Additionally, NV centers have been shown to undergo Jahn-Teller distortion on the femtosecond time scale after excitation, so the ultrafast dynamics would be of interest[223]. The samples are examined with a static X-ray absorption near edge spectroscopy (XANES) technique, using the carbon K-edge high harmonic apparatus.

Materials and Preparation

Measuring the X-ray absorption of diamonds presents several challenges. Firstly, the attenuation length of X-ray light is much shorter than in the visible range, which means that in order to transmit enough photons to make a meaningful measurement, the diamond sample must be very thin, on the order of $\sim$ 100 nm. The typical films or plates of diamond used in applications is on the order of micrometers[228]. For that reason, nanodiamonds were used, which are balls, 70 nm in diameter on average. These diamonds were purchased from Adámas Nanotechnologies[225]. These nanodiamonds are made with a relatively high P1 defect (nitrogen substitution) density of 90 ppm[225]. The Yao group then irradiated and heated these to convert the P1 defects to NV defects (nitrogen neighboring a vacancy), and these are compared to samples that contain the P1 defects (that did not have the NV treatment). These diamonds were suspended in water at a concentration of $\sim$1 mg/mL.

Figure 5.1: The sample is drop-cast and dried in atmosphere on a silicon nitride window. The samples are held in a a holder that sandwiches the edges and allows for simultaneous static spectra to be taken for the NV, P1, and a blank sample.

The second challenge of measuring absorption of solids in the X-ray is transferring a sample onto a substrate that can be measured with the X-ray apparatus. The substrate

that is typically used is a 30-50 nm thick silicon nitride window, mounted in a silicon frame, purchased from Norcada. This substrate contains no carbon and has a relatively small absorption in the 150-350 eV range that the instrument has access to. The process of transferring the sample to the substrate is slightly different for each substrate. For the nanodiamonds, they were drop-cast, which involves suspending them in a mixture, in this case using purified water as the solvent, then dropping a drop of the mixture onto the window. Several permutations of concentration, drop size and number, and drying methods were tried. The best results were obtained with a 1 mg/mL concentration and one or two 10 μL drops. More drops were more likely to break the substrates; although, it is possible this could have been avoided with thicker windows. The drying method chosen was simply evaporation, which took several hours for a single drop and left a large portion of sample in the outer ring. Heating was attempted, but the heat transferred more efficiently through the silicon wafer, leading to deposition of sample on the frame, but not the window. Spin-coating was also tried, which is drop-casting onto a rapidly spinning substrate that uses the centrifugal force to push the solvent off, leaving the sample remaining, but this lead to waste of sample in larger quantities than could be afforded. Eventually, a method of drying by flowing nitrogen over the window was found to be effective, but it was not employed for the nanodiamonds. The resulting samples and their holder are shown in figure 5.1.

Static Absorption and Defect Disambiguation

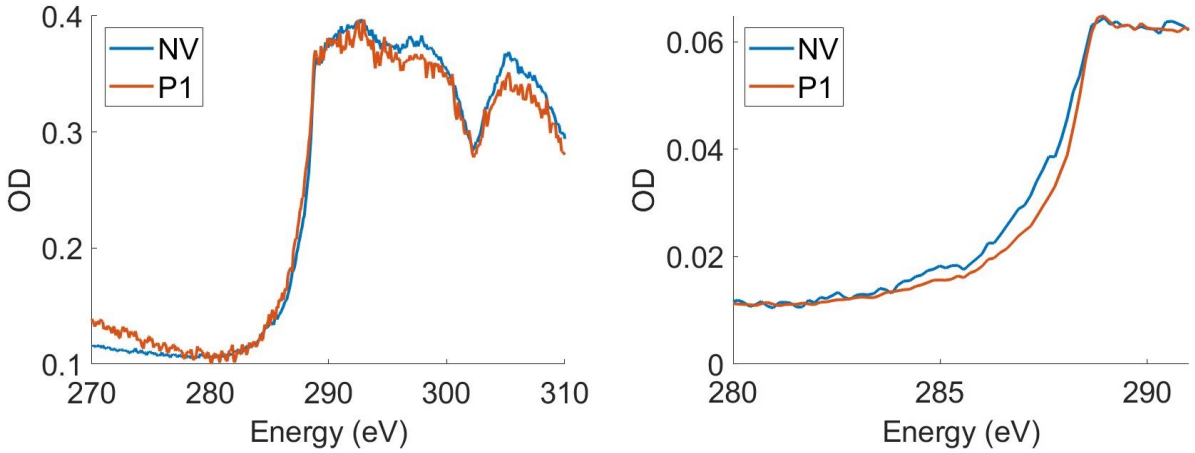

Figure 5.2: The static absorption for both the NV and P1 doped nanodiamonds are shown with normalized absorption. On the left, the overview spectra show the expected diamond shape and the absolute gap at 303 eV. On the right, the buildup that contains the defect states is expanded, showing that there are much smaller absorptions.

The samples were affixed to a solid sample holder that held the windows between 2 steel

plates, so that no glue or other carbon-containing device would be required. The static absorption of the diamonds was measured in the standard way, with a 10000 ms integration of the X-ray flux through the sample, followed by a 10000 ms integration with the sample moved out of the way. This was repeated to increase the signal-to-noise ratio, up to 250 times. The absorption is: $A = -log_{10}(\frac{I_{sample}}{I_0})$. This yields the absorption, shown in figure 5.2. The absorption shows features typical of previous X-ray diamond spectra, namely a sharp rise at 290 eV, including a small peak at the top due to the core-level exciton, followed by a 10 eV long plateau and a dip in absorption at 303 eV, referred to as the absolute gap, which is a common identifying feature for diamond[229].

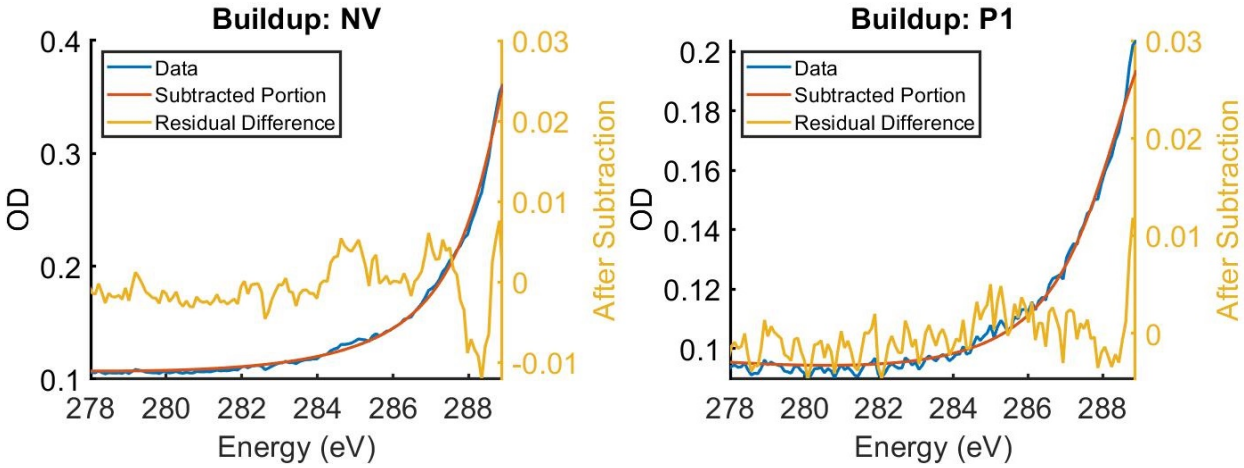

Figure 5.3: The buildup, also called pre-edge absorption or below conduction band absorption, is shown for the two nanodiamond samples. The left are the nanodiamonds that have been radiated to convert P1 defects into NV defects. The right has nanodiamonds that are the precursor. Left axis: The blue is the measured absorption data. The red is the fit, according to equation 5.1. Right axis: the yellow is the data minus the fit. What remains should be the defect absorptions. However, it shows sharp spikes and subtraction in the negative, suggesting overfitting.

The tetrahedral covalent lattice of diamond produces a large band gap, so the valence band begins at the relatively high energy of 290 eV[227]. The defects in diamonds break up this structure and provide lower energy states that exist below the conduction band[227]. The lower energy of these states mean that absorptions due to defects should appear at energies lower than the 290 eV absorption onset. Unfortunately, the energies leading up to the maximum absorption, called the buildup, contains absorption itself, which is usually subtracted by fitting and removing an arctangent shape[230]. Additionally, there is commonly a downward slope of absorption at lower energies than this, so a slightly quadratic slope is also fitted and subtracted, in order to separate the absorption of the defects from the rest.

The part that is fit and subtracted is:

$$A = (a * x + b * x^2 + c) + (d * \arctan((x - e) * f)) \tag{5.1}$$

where x is the energy in eV, and a, b, c, d, e, and f are fit parameters. The result is shown in figure 5.3. With this, peaks can be observed more clearly, notably, there is a clear peak at ∼285.4 eV in both the P1 and NV diamond as well as 2 other potential peaks higher and lower in energy. Unfortunately, there are also places where the subtracted absorption becomes negative, due to the fitting for subtraction containing the absorption of the defect peaks.

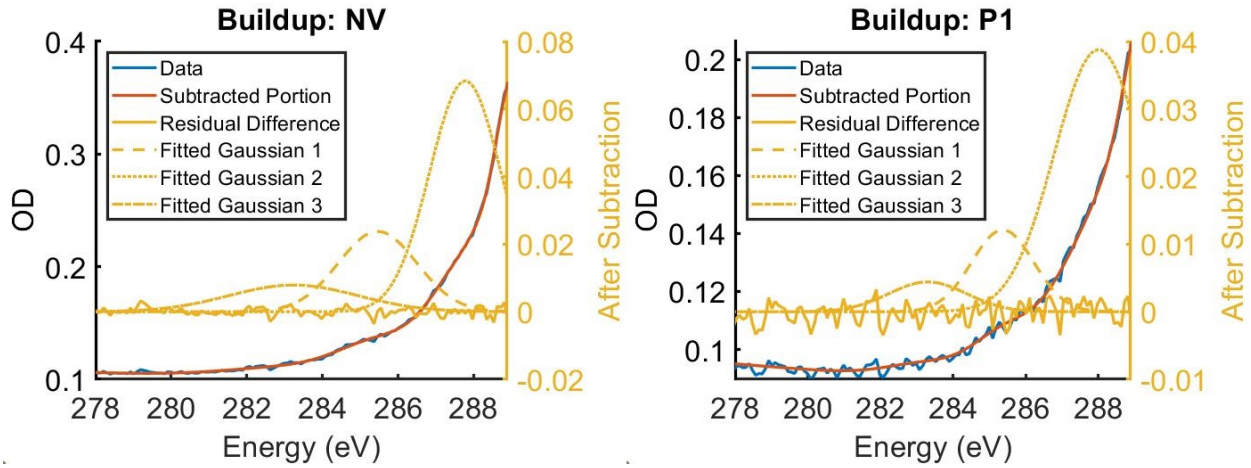

Figure 5.4: The same buildup absorption as in Fig. 5.3 but using equation 5.2 to model the absorption. Left axis: The blue is the measured absorption data. The red is the fit, according to equation 5.2. Right axis: the yellow is the data minus the fit. The fitted Gaussians are shown as dashed lines. The lack of features of the residual shows that the model has the power to adequately describe the data.

The way to deal with the overfitting of the subtraction is to include the expected absorptions of the defect states in the fitting:

$$A = (a * x + b * x^2 + c) + (d * \arctan((x - e) * f)) + 3Gaussians \tag{5.2}$$

as the defects are expected to absorb at relatively specific energies and be broadened by the resolution of the experiment and the lifetime of the state. Doing this reveals 3 Gaussians that comprise the absorptions that might be the defect states. They are found to occur at 285.5 ± 0.6 eV, 287.4 ± 0.5 eV, and 282.5 ± 0.7 eV, which is shown in figure 5.4. The full parameters from the fitting in Fig. 5.4 are shown in table 5.1. It should be noted that the model assumes a level of knowledge about the expected states and absorption that is in

Gaussian Parameter	NV Defect Sample	P1 Defect Sample
Peak 1: Height	0.018 OD	0.021 OD
Peak 1: Center	285.50 ± 0.6 eV	285.49 ± 0.6 eV
Peak 1: σ	1.20 eV	1.34 eV
Peak 2: Height	0.031 OD	0.033 OD
Peak 2: Center	287.38 ± 0.5 eV	287.30 ± 0.5 eV
Peak 2: σ	0.80 eV	0.79 eV
Peak 3: Height	0.004 OD	0.005 OD
Peak 3: Center	282.49 ± 0.7 eV	282.36 ± 0.7 eV
Peak 3: σ	1.22 eV	0.64 eV

Table 5.1: The parameters for the Gaussian peak fitting in Fig. 5.4. The height parameters are scaled by the same factor used to normalize the static absorptions in Fig. 5.2.

reality absent, and that it may be considered overparameterized. However, features at each of these energies have been previously observed and assigned[227, 231, 232].

For identification of the pre-edge features, the energy of their absorption are compared with previous measurements in literature. The first is the most intense peak at 285.5 ± 0.6 eV, which is likely due to graphite-like sp^2 hybridized carbon π^* state on the surface of the nanodiamonds. Graphite has been measured with an absorption at 285.4 eV in multiple experiments[229, 231, 233]. This type of defect is observed at the surface of diamonds, where the tetrahedral lattice structure must stop and be capped[229]. Based on the 70 nm diameter, the surface of a diamond sphere can have up to a 5,350 ppm defect density, compared to the manufacturer's 90 ppm P1 or NV defect density, so it is likely that this absorption peak is graphite-like.

The second absorption feature is at 287.4 ± 0.5 eV. A peak at 287.5 eV was previously assigned to excitation to a C-H σ^* orbital[232]. The presence of hydrogen is often a capping site for the outer layer of the diamond[232]. Similar to the π^* defect, the 287.7 eV feature does not contain additional information about the NV or P1 centers.

The last peak that has a previous literature assignment is the 282.5 ± 0.7 eV peak. One paper has assigned this peak to an NV defect, previously[227]. That paper shows an absorption peak at 282.5 eV in synchrotron absorption of NV nanodiamonds and shows a theoretical calculation at the same energy to make its assignment. However, samples with only P1 defects were not tested, so no comparison could be made. In this experiment, the 282.5 eV peak is observed in both the NV and P1 samples, which suggests that it cannot be due entirely to NV defects. It is possible that this peak is due to other defects, but there is a difference between the P1 and NV samples. In all collected data, the 282.5 eV peak in the NV was wider than that in the P1 samples. Conversion from P1 to NV defects is not 100%[226], and the energies may be similar (carbon neighboring nitrogen). Without experimental spectral resolution to separate two peaks, the presence of both would lead to

a broader absorption peak, and the separate concentrations of NV and P1 defects cannot be determined.

Unfortunately, these data were taken at a relatively early stage of the apparatus build, so the carbon K-edge photon flux was about 15x lower than what the instrument is capable of now. Without that extra flux, a transient measurement of the nanodiamonds was not attempted, as there would not be sufficient signal-to-noise ratio. As a future possibility, if this is ever revisited, the NV and P1 defects may be able to be differentiated in a transient measurement with excitations tuned to the defect. The two defects have different absorptions in the visible range, where NV centers have narrow absorptions of the zero-phonon line (ZPL), 637 nm for NV^{-1} [234], compared to a broad visible absorption or sharper absorption in the infrared at 6900 nm for P1[235]. The NV centers could be selectively excited with wavelengths tuned to their ZPL, and the transient absorption might show differences between the samples. Although, using narrow bandwidths as the pump laser will require using a long pulse and reduce the temporal resolution of the experiment. The temporal resolution could be maintained by utilizing a pulse shaper to selectively remove the appropriate wavelengths and looking for signal that disappears between removal of the wavelengths. However, pulse shaping experiments are not currently possible with the apparatus.

5.3 Weak Signals in MoS_2 and WS_2

A class of semiconductors that have interesting potential applications are transition metal dichalcogenides (TMDC). The structure of these semiconductors consist of individual layers, held together by van der Waals forces[236]. The individual layers of one material can be stacked with a variety of other materials and create unique electronic devices[236]. Prior to that, it would be beneficial to have a better understanding of the electronic dynamics of the individual materials, so two materials were studied, MoS_2 and WS_2. These have band gaps of 1.23 eV (MoS_2[237]) and 1.35 eV (WS_2[238]. A similar semiconductor with the same structure has been studied previously in this group, $MoTe_2$[87]. In that study, they observed an electron-hole recombination time of 1.5 $\pm$ 0.1 ps, as well as hole thermalization and cooling times of 15 $\pm$ 5 fs and 380 $\pm$ 90 fs, respectively, but in that experiment, most of the information gained was from the Te $4d$ levels. This experiment looks at the sulfur $2p$, the $L_{2,3}$-edges, at 163 eV.

The previous experiments in the group also took limited measurements on MoS_2 and WS_2, so samples that were used in this experiment that had previously been made at the Molecular Foundry by a series of chemical vapor deposition and heating[239]. The samples used were 50-100 nm thick, mounted on 30 nm thick silicon nitride windows. The relatively thick samples were chosen because a large amount of absorption was found to be necessary to obtain signals large enough to be measured.

The static absorption of both MoS_2 and WS_2 is shown in figure 5.5. In it, the absorption consists of a small feature, consisting of 3 peaks at 163 eV, followed by a large rising edge at 170 eV. These peaks have been measured and assigned previously, and it suggests that

the first feature is the start of the conduction band[97]. The reason that the first feature is so small, despite the conduction band consisting of a large density of states, is that the lowest energy valleys are predominantly S 3p character, and the S 2p to 3p transition is dipole forbidden[97]. The small absorption in this region comes from the small amount of 3 d character in the density of states, and the rising edge maps well to the transition to the 3 d dominated parts of the density of states. The small absorption to the bottom of the conduction band is detrimental to the types of measurements that this experiment would undertake, because the majority of changes occur where the electrons and holes are moved across the band gap, i.e. the top of the valence band and the bottom of the conduction band.

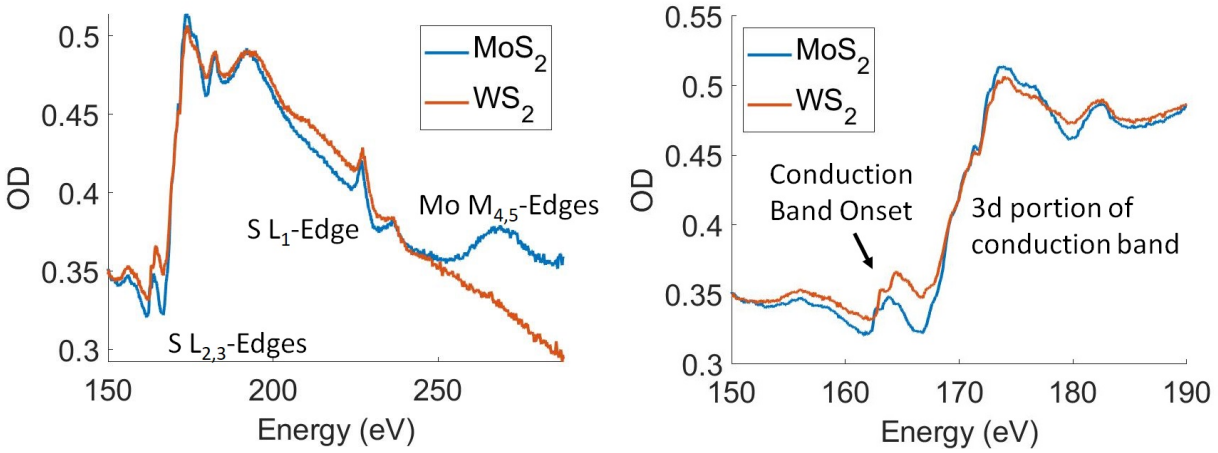

Figure 5.5: Static absorption of MoS_2 and WS_2 are shown and the relevant edges are labeled. The right shows a portion highlighting the relevant concudtion band onset.

The transient measurements were taken with a pump pulse of <5 μJ, focused to 65 μm FWHM, covering 650-1000 nm, and compressed to ~6 fs. This resulted in a ΔOD of ~6 mOD that was due to heating of the sample that remains hot between the 1 ms between pulses at 1 kHz, shown in figure 5.6. This signal was reduced both by decreasing the frequency of laser pulses to 250 Hz with choppers and by rastering the sample as quickly as possible. Due to the small beam at the early point along the optical path at which the pump and probe are split and the high intensity at that point making chopping unsafe, two separate choppers were used on the pump and probe arms after the hollow-core fibers. Having two choppers running required that they be synchronized to pass light at the same point in their rotations, which was achieved by turning one on, then turning the second one on, allowing the second one to reach a stable spin speed, and measuring if the two were in sync. If not, the second chopper was very briefly turned off, then turned back on to a stable spin speed, forcing its phase to change, as the old choppers used do not have the capability to do as large of a phase change as necessary. The synchronicity of the choppers was monitored by the sum-frequency generation between the two pulses, through the balanced optical cross-

correlator (BOC). The 250 Hz was achieved by use of a standard 10 slot, 50% duty cycle chopper with tape covering an additional 5 slots, making a 25% duty cycle chopper, and it was run at 500 Hz on the chopper control box.

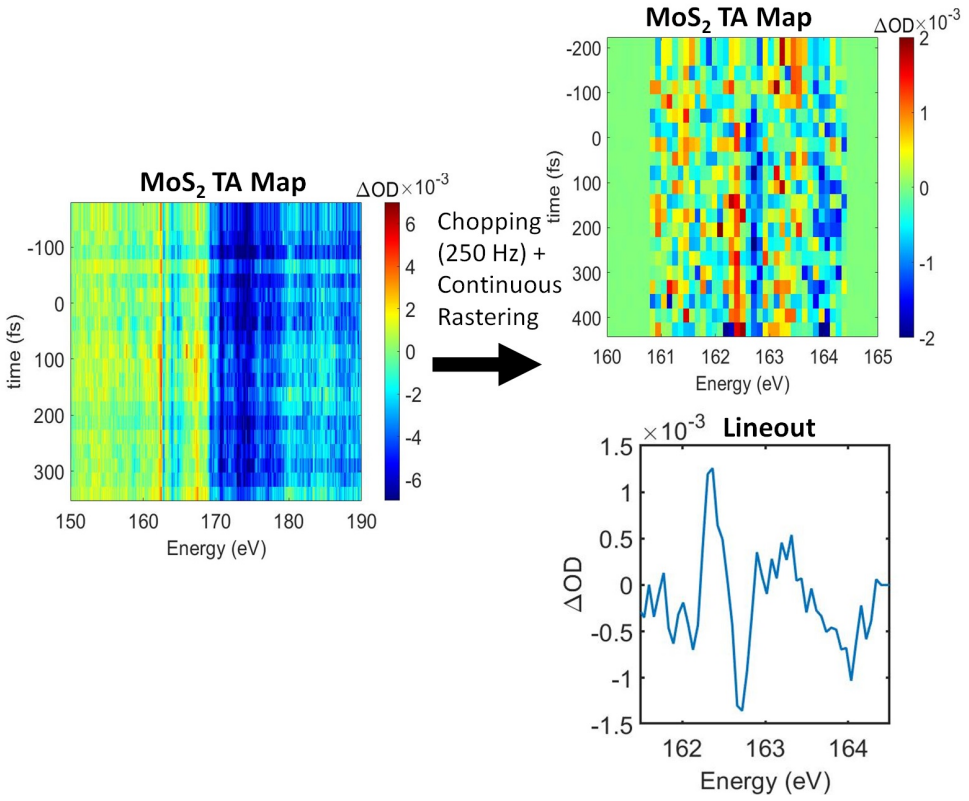

Figure 5.6: Left: ΔOD data showing the signal dominated by heat. Right, top: transient signal from MoS_2. The signal-to-noise ratio is low, due to the small signal and the requirement of running at 250 Hz, 4x fewer photons. Right, bottom: An averaged signal, showing the main features more clearly.

The rastering was done with the motors usually used to position the sample relative to the X-Ray beam, VT-80 motors from PI. These are nominally capable of a top speed of 3 mm/s; although, measurements showed this speed closer to 2.67 mm/s. A rastering pattern, consisting of a series of non-overlapping U-bends was chosen. Based on these speeds and the spot size of the pump pulse, assuming a Gaussian shape, simple calculations showed that at 1 kHz, the probe would be measuring a spot that experienced 94% of the peak intensity from the previous shot, whereas with 250 Hz, this value drops to 34%. This does not include heat dissipation. These numbers suggest that the heat feature was reduced more effectively by chopping than rastering in this case, but that in samples that do not conduct heat well, rastering is an option for reducing those signals.

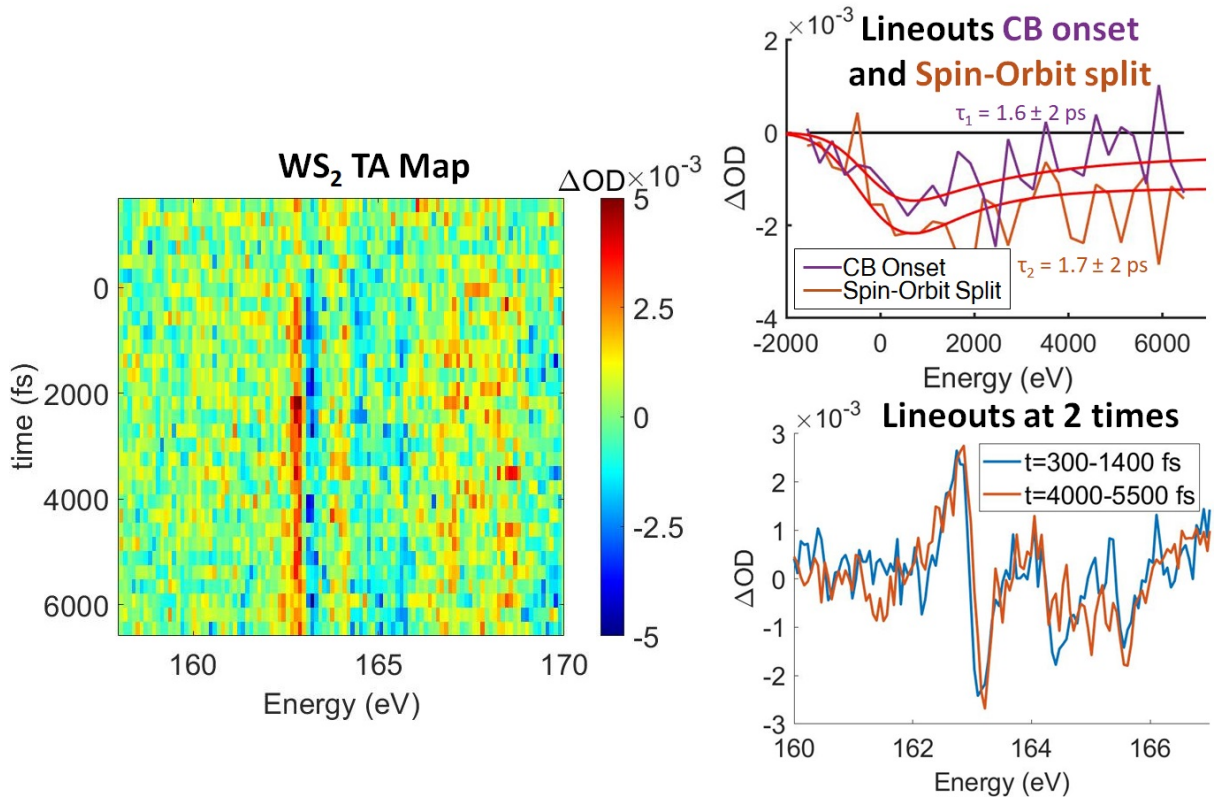

Figure 5.7: Left: ΔOD data showing the transient data from WS_2. Right, top: Fitting of the negative features, showing decay on a similar timescale to 1.5 ps; although, the signal-to-noise ratio is not high enough to make a good fit. The purple corresponds to absorption from the S $2p_{3/2}$, and the maroon corresponds to the spin-orbit split energies, absorption from the S S $2p_{1/2}$. Right, bottom: An averaged signal around 2 time points, ∼1 ps and ∼5 ps, showing that the point at which the signal crosses 0 is shifting, as was seen in the $MoTe_2$ data[87].

The actual signal of the MoS_2 was predictably low. It consisted of a ±1.5 mOD signal at the onset of the static absorption, shown on the right of Fig. 5.6. Specifically, the positive signal occurs at 162.6 eV and the negative at 162.9 eV. This is much smaller than the typical band gap experimentally measured of 1.23 eV (MoS_2)[237], which suggests that it is not entirely due to state blocking/opening that would be expected from the presence of electrons and holes in the conduction band and valence band, respectively. It is more indicative of band gap renormalization, which causes the absorption of the conduction band to shift to lower energies, leading to the positive feature. There is some evidence of another positive feature at 161.9 eV, which is closer to the expected spacing from the band gap, but that feature is not above the signal-to-noise ratio level.

The molybdenum $M_{4,5}$-edge and sulfur L_1-edge are visible in the static absorption, but both edges are very broad, which does not produce strong transient signals, and indeed, no signal is observed at these edges.

The WS_2 sample was pumped using photons that were better suited to crossing the band gap by using a short wave reflector mirror to remove the wavelengths above 700 nm; although, this lengthened the pulse significantly in time. This sample showed a slightly stronger signal, up to 3 mOD with a similar structure to the MoS_2 signal, shown in Fig. 5.7. It consists of a positive then negative ΔOD signal at the bottom of the conduction band, 162.8 and 163.1 eV, respectively. Because of the increased signal, the spin-orbit split negative signal can also be observed 1.2 eV higher in energy at 164.3 eV. No signal is observed that could be associated with the valence band holes, which should be around 161.9 eV, based on the 1.35 eV band gap[238]. Lineouts can be taken of the two negative signals and fit to exponentials, which results in measured decay times of 1.6 $\pm$ 2 ps and 1.7 $\pm$ 2 ps for the $2p_{3/2}$ and $2p_{1/2}$, respectively. These are similar to the decay constant found in the previous study on $MoTe_2$, 1.5 $\pm$ 0.1 ps, but this study does not thave sufficient S/N to provide additional interpretation or meaning[87].

The signals in MoS_2 and WS_2 at the bottom of the conduction band are very weak due to the forbidden dipole transition from the $L_{2,3}$ edge, and that forbidden transition can be predicted, based on the small feature at low energies before the large rise in the static XUV absorption. Unfortunately, this effect is also observed in several other sulfides, such as other transition metal dichalcogenides (PtS_2, ZrS_2, TiS_2)[240], cubic CdS[241], Cu_xS[242], and more complicated structures like $CuFeS_2$[243]. That suggests that the sulfur $L_{2,3}$-edges, despite being strong and sharp XUV absorption edges, are not well suited for studies on semiconductors.

5.4 Carbon Nanotubes

Graphene has very interesting an unique electrical proprieties[244]. It is a mono-layer, 2-D material, of conjugated carbon, which gives it massless Fermions at the interface of the valence and conduction bands in the ideal case[245]. Rolling the sheet of graphene into a tube structure gives a 1-D material, called carbon nanotubes (CNTs). The electrical properties of these tubes can be tuned from metallic to semiconducting by changing the angle at which the tube is rolled, essentially taking a slice of the 2-D graphene k-space[7]. The angle of the internal graphene is referred to as the chirality of the CNT, which is represented as a pair of whole numbers (n,m), the chiral vector[246]. In general, the larger n and m are, the larger diameter tube and the smaller the band gap[247]. The lifetime of the electron-hole excitons is of interest for using CNTs in solar cells and as a wire for transfer of energy, and the lifetime has been studied in many experiments in the visible[248–253]. These studies give times that range between 300 fs and several ps; although, some of the studies suggest a large factor in the time depends on how connected the nanotube bundles are[252, 253]. These studies were all measuring visible, infrared or UV absorption, so they could not measure the effect of

metallic nanotubes, because those do not have a specific absorption energy in the visible[7]. X-ray spectroscopy is sensitive to metals[254], so as a method it is able to measure the lifetime of metallic nanotubes, including multi-walled carbon nanotubes (MWCNTs), which are generally considered metallic[7].

Materials and Preparation

This experiment compares the signals from multi-walled carbon nanotubes (MWNCTs) and single-walled carbon nanotubes (SWCNTs). Samples of carbon nanotubes were purchased off-the-shelf from vendors. The MWCNTs were obtained from Cheaptubes.com, part number: 030407, Short Multi Walled Carbon Nanotubes, which are listed as having an outer diameter: 50-80nm, inside diameter: 5-10 nm, length: 0.5-2.0 μm, Purity: 95 wt%. The SWCNTs are purchased from Sigma-Aldrich in 2 categories: SWCNTs that do not have a specific chirality and SWCNTs that have chiralities that are preferentially semiconducting. The non-specific SWCNTs are part number: 704113, Carbon Nanotube, single-walled, which only have the specification of having diameter: 0.7-1.3 nm, 70 wt% carbon nanotubes, median length: 1 μm, G/D ratio $\geq$ 15, defined next. The G/D ratio measures the ratio of 2 peaks in the Raman spectrum, and a higher G/D ratio meaning the sample has fewer defects; a ratio of 15 is somewhat low quality[255]. The chiral specific SWCNTs are part number: 773735, with specifications of diameter: 0.78 nm, median length: 1 μm, G/D ratio $\geq$ 20, 95 wt% carbon nanotubes, 95% CNTs as semiconducting, and $\sim$40% as the specific (6,5) chirality.

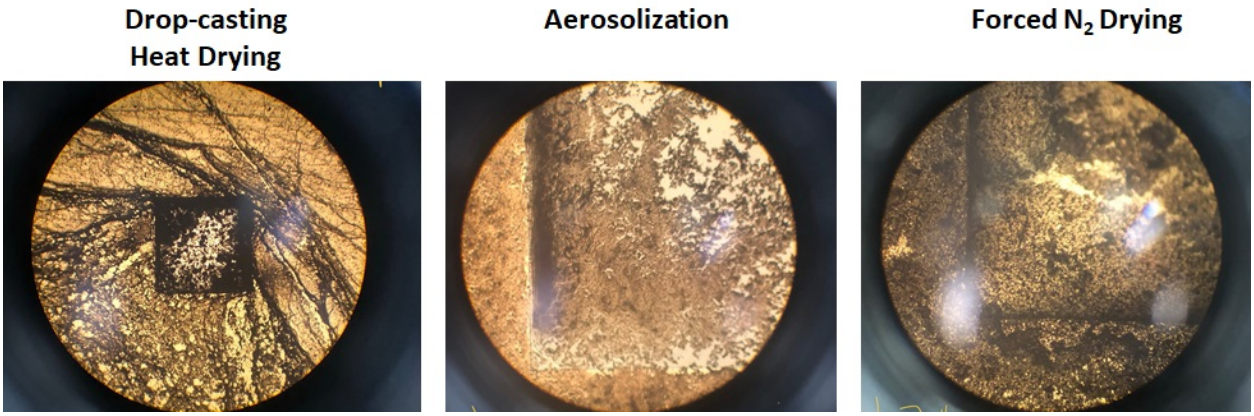

Figure 5.8: Different methods of drop-casting the carbon nanotubes are shown, taken under an optical microscope with 10x magnification. A method of aerosolization, explained in the text, was found to make the most even layer, but it resulted in a large amount of waste, so drying with forced N_2 was used.

The MWCNTs are not chiral specific and contain many possible chiralities in each nan-

otube. A mixture of semiconducting and metallic tubes in an MWCNT has the density of states of the sum and is considered to be metallic[7]. The non-specific chirality SWCNTs contain a mixture of semiconducting and metallic nanotubes, and the expected signal is an average of each individual component. The (6,5) SWCNTs are semiconducting with the (6,5) chirality having a band gap of 1.27 eV[247].

Each of the nanotube types were suspended in isopropyl alcohol (IPA) at a concentration of ∼0.1 mg/mL. The suspensions were shaken and sonicated at low energies, 130 W, to break up clumps of CNTs. Clumping remained a problem in drop-casting the CNTs onto the silicon nitride windows, so different methods of deposition were tested. Because of the low concentrations to reduce clumping, a single drop from drop-casting did not introduce enough CNTs for measurement. Multiple drops were needed, so additional drying was necessary in addition to evaporation of the IPA. The first method of drying was heating on a hot plate. This had the same problem as with water and the nanodiamonds; it heats the silicon wafer more efficiently and little sample stays on the window. In addition, the CNTs tended to clump with this method, shown in Fig. 5.8. All samples in Fig. 5.8 use MWCNTs, because the samples cost much less than the SWCNTs. The second method attempted was aerosolization of the suspension. This was done cheaply by utilizing a paint airbrush with N_2. It produced the best results, in terms of reducing clumping with MWCNTs, but the majority of the sample missed the window substrate, so it was not cost efficient enough to use with the more expensive SWCNTs. The last method of drying was with forced N_2 drying, which involved drop-casting a drop of the suspension then blowing nitrogen to dry it off. This had efficacy in reducing clumping between the other two methods, shown in Fig. 5.8. The sample could be steered as it dried to get more CNTs on the window. Drying with N_2 made use of all of the sample, so it was the method of applying the CNTs to the sample.

IPA contains carbon, so in order to ensure that the IPA did not introduce additional signals to the samples, pure IPA on silicon nitride was tested, and no absorption was observed. The IPA has a high enough vapor pressure that it all evaporates and does not affect the experiment.

For further characterization, the samples on the silicon nitride windows were examined using a scanning electron microscope (SEM), specifically a Zeiss Gemini Supra 55 VP-SEM at the Molecular Foundry at LBNL by Sheena Louisia. Magnification up to 50,000x were taken, shown in Fig. 5.9. The MWCNTs are stiffer, due to the multiple layers and larger overall diameters, which leads to less interlocking of multiple tubes. The SWCNTs, alternatively, are flexible enough to form a tight-knit network of highly interconnected tubes. It shows tube crossings spaced by only 10s of nm, at most. There is not an obvious different between the two SWCNT samples. The images are typical of nanotube bundles[255].

Static Absorption Data

The absorption of the nanotubes is shown in Fig. 5.10. The X-ray spectra of all three CNT samples show 2 distinct features: a standalone peak at 285.3 eV and a sharp rise, followed by a plateau at 291.7 eV. In previous literature, the 285.5 eV peak is attributed to the π^*

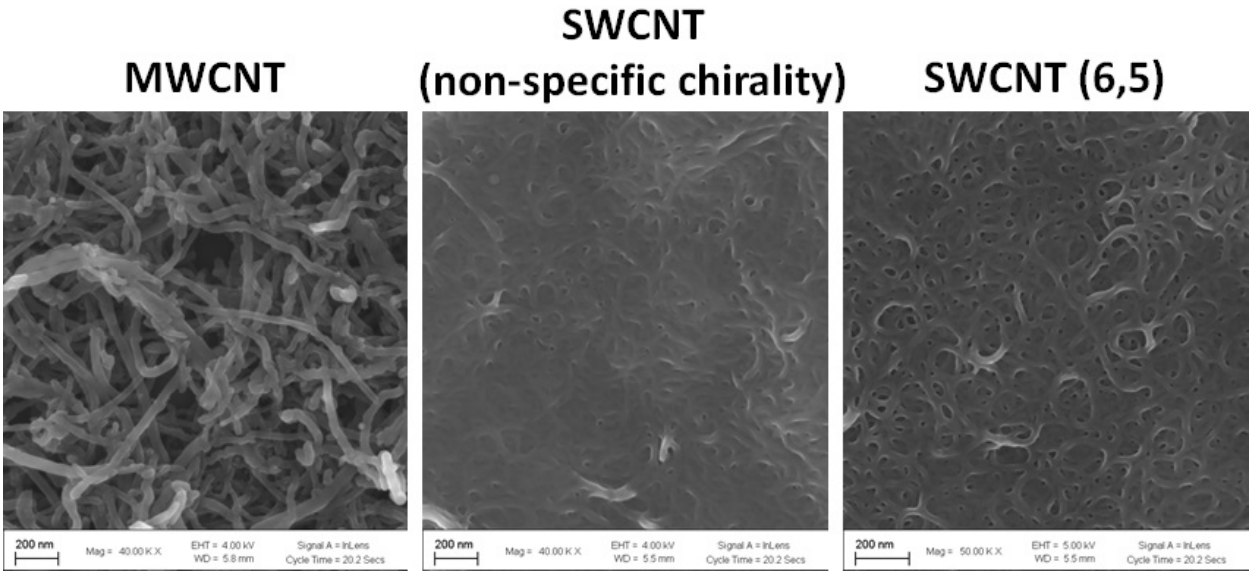

Figure 5.9: Magnification of the different types of carbon nanotubes with an electron microscope are shown. Magnifications are 40,000x for the left 2 and 50,000x for the right. It shows a high degree of interconnectivity between each of the tubes. The stiffer MWCNTs do not bend and link as much as the SWNCTs.

density of states (DOS) and the 292 eV to the σ^* DOS[256]. Comparing the absorption of the three samples, the SWCNT samples show a dip after the π^* peak, followed by a plateau and a less sharp rise to the σ^* peak, which is typical of single-walled absorption[256]. Additionally, the MWCNT has a slightly wider π^* peak that extends to lower energies. The difference comes from the SWCNTs having a better defined DOS that correspond to similar tube diameters, while the MWCNTs have many different diameters, up to 50-80 times as wide as the SWCNT.

The visible and infrared absorption of the suspensions in IPA is also shown in Fig. 5.10. It shows that the (6,5) SWCNT samples have three distinct peaks around 1050 nm that are repeated around 600 nm, which might be expected of a sample that contains three different semiconducting chiralities, containing the (6,5) chirality[247]. The MWCNT sample shows a near infrared peak[257], which shows that both samples are what was purchased. Unfortunately, the non-specific chirality SWCNT was not on-hand when the measurement was taken.

Transient Data and Discussion

The transient data for each of the samples again contains similar features, shown in Fig. 5.11. In order from lowest energy to highest, feature 1 is a positive signal centered at 283.6

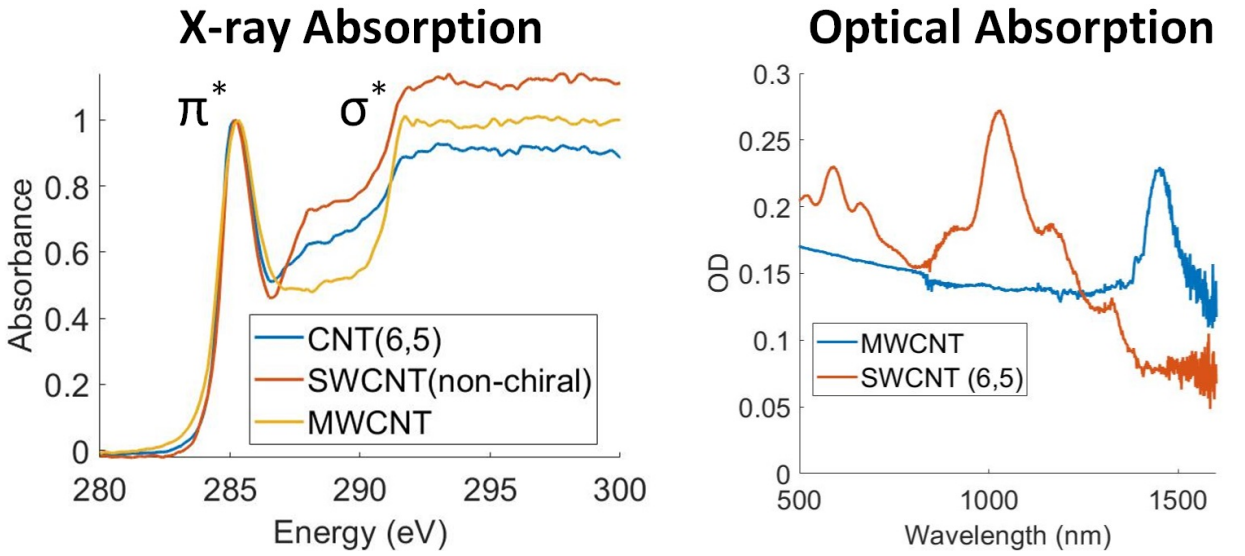

Figure 5.10: The static absorption for the different types of carbon nanotubes are shown. The left shows the soft X-ray absorption at the C K-edge. The right shows the visible absorption, showing that different spectra are present between the MWCNTs and SWCNTs.

eV, at a lower energy than the π^* peak, which would suggest it corresponds to the previously inaccessible π valence band. It rises quickly and decays in 100s of fs. Similarly, feature 2, at 284.9 eV, has similar time scales but is negative ΔOD. There is a negative feature, labeled feature 3, close to feature 2 that rises with in roughly 100 fs. It can be seen that it shows different time dynamics and it can be temporally resolved in the lineouts on the right of Fig. 5.11. Feature 4 is a more intense positive feature at energies directly lower than the σ^* peak. It has a slightly longer rise time on the order of 100 fs. There is also a less clear negative feature above feature 3 that shows the same time dynamics.

These features are compared between samples and to literature and integrated to get time information. The ΔOD colormaps are shown in Fig. 5.12. The first qualitative difference that can be seen is that the MWCNTs show a slightly stronger signal than the SWCNTs in feature 4. This is likely due to the same effect that causes the sharper edge in the σ^* feature, where a shift or broadening in energy would lead to a larger ΔOD. The second difference is that the MWCNTs show a slight broadening in feature 1 after time zero; although, it is possible that this is simply due to noise in the measurement. The effect can be seen in the positive to negative crossing between features 1 and 2, which shifts to slightly lower energy during this time. However, the converse effect can be seen in the SWCNT (6,5) and to a lesser extent in the non-specific SWCNT sample. This shift in energy of the positive feature towards higher energies is typically associated with hot holes migrating to the top of the valence band[221]. The initial broadening of feature 1 in the graphite paper was attributed

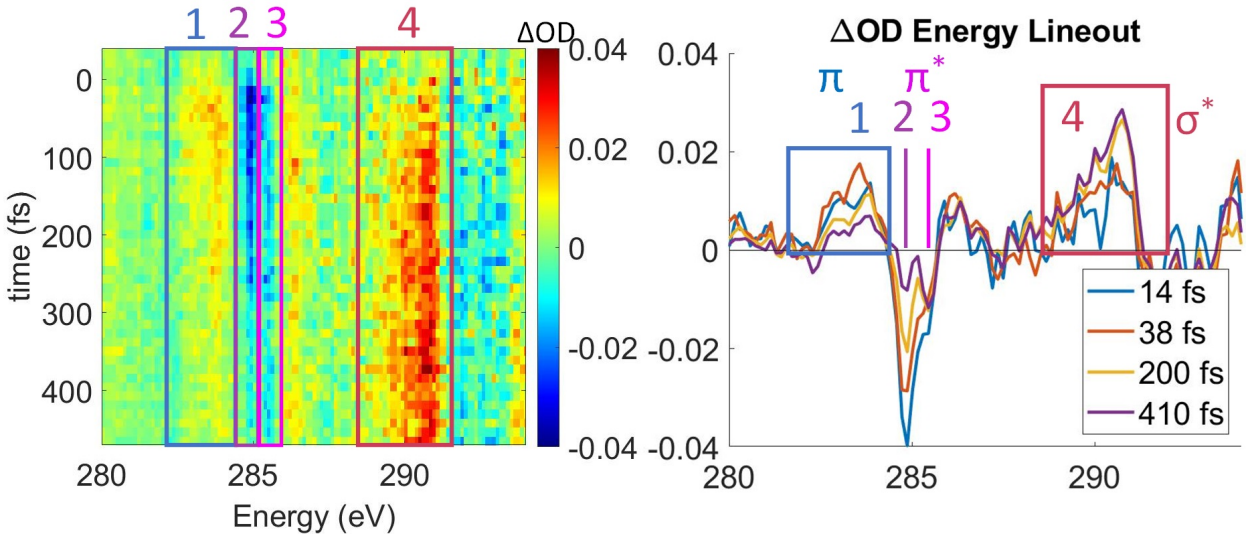

Figure 5.11: An example ΔOD transient of the chiral non-specific SWCNT sample is shown on the left. The right shows lineouts integrated near selected times. Four features are identified and are discussed in the text.

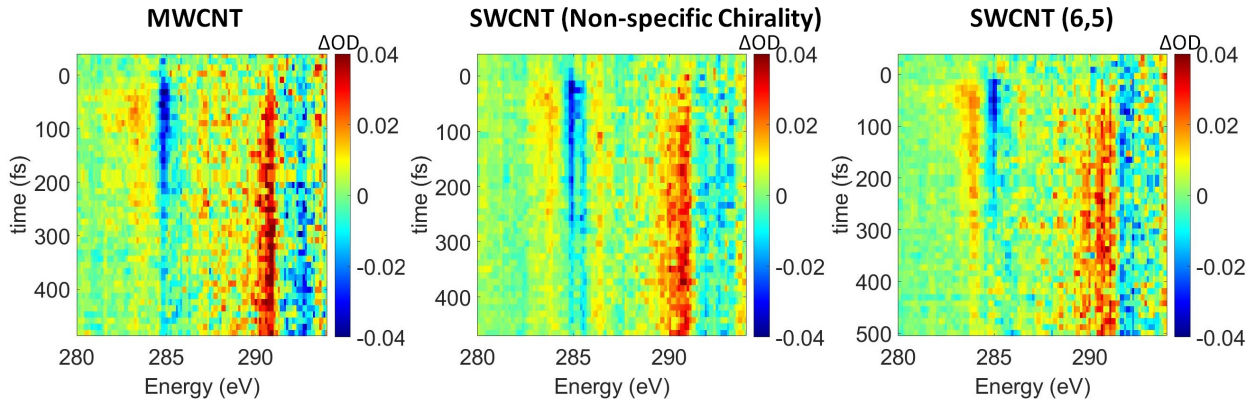

Figure 5.12: The transient data for all three CNT samples are shown. The three show very similar signals, displaying all 4 features from Fig. 5.11.

to a combination of Auger heating and impact excitation[86]. Auger heating is a scattering process of hot electrons or holes with each other, such that one goes down in energy while another goes up, which would lead to broadening of more energies occupied in the band, broadening the signal. Impact excitation is a slight variation, where a hot electron in the conduction band and an electron in the valence band scatter and both move towards a middle

spot in the conduction band, creating extra carriers[86].

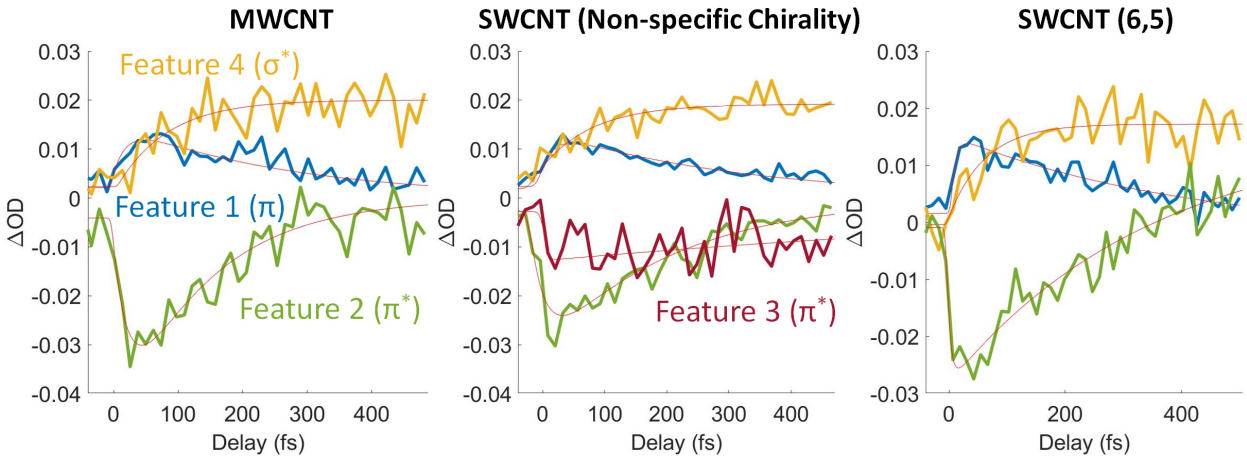

Figure 5.13: The lineouts from Fig. 5.12 for features 1, 2, and 4 are shown. Feature 3 is not integrated, because the signal is not consistent in all 3 measurements, so it would only be distracting. The time constants for each of these lineouts are given in table 5.2.

Sample	MWCNT	SWCNT Non-specific	SWCNT (6,5)
Feature 1 (283.6 eV, π) Rise (fs)	24 ± 17	20 ± 10	17 ± 9
Feature 1 (283.6 eV, π) Decay (fs)	270 ± 90	320 ± 70	300 ± 60
Feature 2 (284.8 eV, π^*) Rise (fs)	22 ± 12	23 ± 10	9 ± 7
Feature 2 (284.8 eV, π^*) Decay (fs)	140 ± 40	210 ± 40	240 ± 30
Feature 3 (290.5 eV, σ^*) Rise (fs)	80 ± 40	80 ± 50	60 ± 50

Table 5.2: The lifetimes of the fits in Fig. 5.13. The decay of feature 3 is not included here, as no significant decay in the first 500 fs is measured for that feature.

Lineouts along the time dimension are shown in Fig. 5.13 and the lifetimes of each fit are given in table 5.2. Feature 3 at 285.5 eV is only shown for the non-specific SWCNT, as that dataset happened to have better signal-to-noise ratio for that feature. The feature appears in the other samples more prominently in other datasets, so it is not unique to non-specific SWCNT. The figure shows the feature appearing to grow in slightly later; although, noise may have a factor in that. Feature 3 continues to remain near -10 mOD for the rest of the 500 fs. Another feature that remains present largely throughout the 500 fs is feature 4, which rises with a time constant of ∼80 fs for each of the samples. Feature 1 and 2 have more similar timescales, both decaying visibly during the measurement. The rise for both is ∼20 fs with the MWCNT rise times having a slight tendency to be longer than the SWCNT

samples, especially the SWCNT (6,5) sample, with 24 ± 17 in MWNCT compared to 17 ± 9 in SWCNT (6,5) and 20 ± 10 in non-specific SWCNT. The SWNCT (6,5) has the shortest rise with 17 ± 9 fs in feature 1 and 9 ± 7 fs in feature 2. These numbers do not clear the error bars of each other, so it is only a tendency for the MWCNT to be longer. The decay of the two features is more interesting, as feature 1 decays slightly slower than feature 2. The decay times of feature 1 are 270 ± 90 fs, 320 ± 70 fs, and 300 ± 60 fs for MWCNT, non-specific SWCNT, and SWNCNT (6,5), respectively. The decay times of feature 2 are 140 ± 40 fs, 210 ± 40 fs, and 240 ± 30 fs again for MWCNT, non-specific SWCNT, and SWNCNT (6,5), respectively. The decay times for features 1 and 2 are significantly different between features 1 and 2 for MWCNT and non-specific SWCNT; although, the linouts were taken with the assumption that the signal would end at a ΔOD of 0. Not making that assumption would increase the error bars significantly, as the measurements do not extend far enough in time to determine if there are very long-lived absorptions that may move it from zero. To that end, though, a measurement was taken out to 2.5 ps (only for the SWCNT (6,5) sample), shown in Fig. 5.14. It shows that feature 1 remains slightly positive at long times, feature 3 remains slightly negative, and feature 2 goes nearly to 0. It also shows that feature 4 decays with a lifetime on the picosecond range; although, it is still out of the scan range for this scan to accurately determine its lifetime.

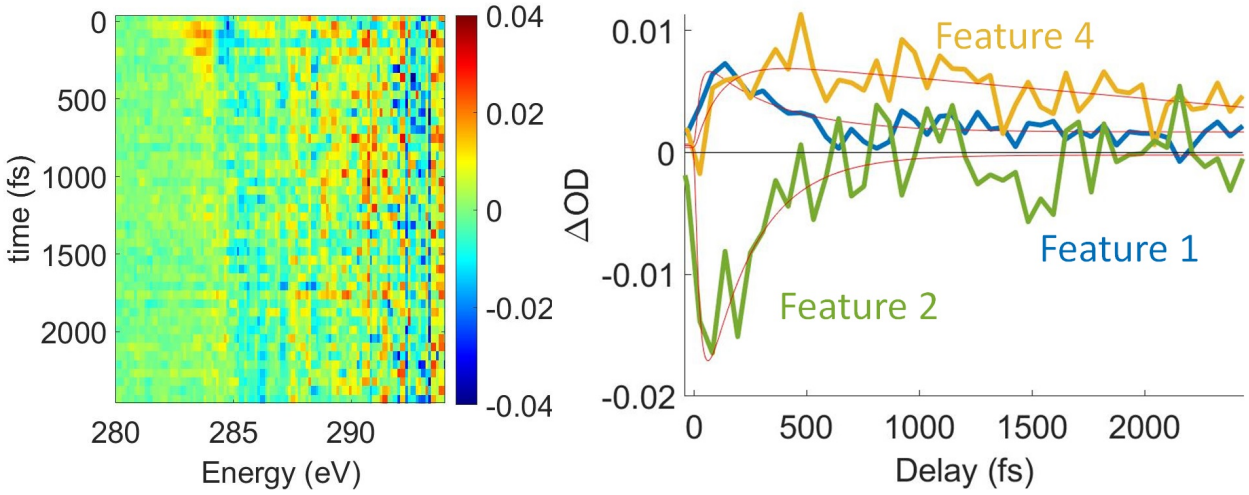

Figure 5.14: The transient data and lineouts for the CNT (6,5) sample are shown for a scan that measures out to 2.5 ps.

For assignments of each of the features, we start with the assignments made to the similar features in the graphite paper[86]. Feature 1 was assigned to the holes in the valence band, and feature 2 to the electrons in the conduction band. Feature 4 was assigned as shift and broadening of the static, due to lattice heating, based on previous work in this group[28]. Feature 3 was not observed separately from feature 2 in their data. They note that

broadening and shifting are considered as possible causes of features 1 and 2, but then discard that interpretation, because their signal does not match contributions from just shifting. Based on the long, continued signal after 2 ps in these data, some component of feature 1 likely contains a heat signal, leading to broadening and shifting. Heat in CNT bundles randomly interlocked might be expected to dissipate heat more slowly than graphite[258]. Heat broadening is also likely the cause of feature 3; although, a full decomposition into state-blocking, broadening, and shifting was not attempted on these data[28]. The graphite paper showed biexpoential decays for each of their features, which may be due to heating, and if so, it would cast doubt on their assignment of Auger heating and impact excitation in the holes and electrons[86].

To take the lifetime of the electron-hole pairs from features 1 and 2, both likely contain contributions from both their carriers and from heat effects. The 2.5 ps scan shows that feature 1 ends more significantly away from 0, which is likely the reason that the fitted feature 1 lifetimes are longer than feature 2 lifetimes; although, it is possible the long time feature 1 signal is longer hole lifetimes. Previous work shows that bare nanotubes can have electron-hole recombination times of ∼300 fs, which is close to the measured times of either feature. For this experiment, the electron-hole recombination times are taken for the cleaner feature 2, which gives lifetimes of 140 ± 40 fs, 210 ± 40 fs, and 240 ± 30 fs for MWCNT, non-specific SWCNT, and SWNCNT (6,5), respectively. Of these, MWCNT are outside the 95% confidence interval of the SWCNT samples, so it has a shorter recombination time, and the SWCNT being purely semiconducting does not give it an exceptionally longer lifetime. It was observed in previous experiments that the bandgap of different chiralities did not have an effect on hole-electron exciton transfer and that the major determining factor in recombination times was the distance the tubes were isolated before touching other tubes[251–253]. The two SWCNT samples have similar diameters and likely have similar amounts of interconnectivity, giving the similar time constants.

Nanotube Conclusions

Unfortunately, not much can be said about the quantitative dynamics of the carbon nanotubes. The datasets shown were taken from multiple different days, introducing potential factors in comparison of the samples. The attempts to take measurements of the 3 samples simultaneously resulted in some or all of the measurements having terrible signal-to-noise ratio. The most common cause of the bad noise was choosing a bad spot to take a scan on the sample window. The samples were prone to clumping, especially the SWCNT samples, which can lead to scattering. There were attempts to determine if microscopic differences lead to the changes by using the SEM to look at multiple spots on the window (and multiple windows that had the same sample), and no differences were clear, other than the obvious differences between the MWCNT and SWCNT samples. Additionally, some time dynamics showed differences for the same sample on different days. For example, the rise time of the MWCNT sample was measured between 70 fs and 17 fs. This largest difference was measured over several months, so it is possible that it was due to upgrading the apparatus to have

better time resolution, but there are doubts raised by these variations. There is too much variability in the sample preparation that cannot be accounted for, despite best efforts.

What can be concluded are a few qualitative results. The first is that CNT shows similar features to graphite in XTAS[86], which is expected given that both have the highly conjugated π network of graphene. It shows that the signals are relevant to the 1-dimensional networks. The recombination lifetimes were shorter than the reported recombination times in graphite[86]. The reason for the shorter lifetimes may be that the interconnectivity of the tubes leads to crossings, similar to defects, where the hole and electron can recombine[252]. Similarly, this work can be compared to the carbon nanotube work of Martin Zanni and coworkers, where lifetimes of electron-hole excitons were observed to be $\sim$300 fs. The lower limit of lifetimes was achieved by using bare nanotubes, similarly interconnected as the ones used in this experiment[251]. This experiment is able to observe metallic nanotubes in addition to semiconducting, and no substantive difference is observed between the purely semiconducting (6,5) SWCNTs and the non-specific SWCNTs. That bolsters the conclusion made in the Zanni work, that for nanotubes that can touch one another, the limiting factor in lifetime is how far apart the tube crossings are, not the electronic structure of an individual tube[251]. Still, the MWCNTs were shown in the SEM images to cross each other far less often than the SWCNTs, but both samples had similar lifetimes, and the MWCNT lifetime was potentially slightly shorter. That suggests that MWCNTs may be recombining holes and electrons between the walls of a single nanotube, which would be a finding that is unique to this experiment; although, the strength of such a claim cannot be made quantitative without additional evidence.

5.5 Summary

Various solids have been studied with X-ray spectroscopy. Many of them have low signal-to-noise ratio. Defect states are observed in the buildup of nanodiamonds. Features from sp^2-hybridized carbon and σ^* C-H bonds are measured in addition to the desired NV and P1 defects; although, the NV and P1 defects are not able to be disambiguated. Transient absorption in MoS_2 and WS_2 is measured and found to have very low signal, due to the $3p$ character and forbidden transition to the conduction band onset. A similar recombination time to $MoTe_2$ is found in WS_2, 1.6 $\pm$ 2 ps, but the error was large. Finally, in carbon nanotubes, recombination times are measured in MWCNT, non-specific chirality SWCNT, and semiconducting (6,5) SWCNT to be 140 $\pm$ 40 fs, 210 $\pm$ 40 fs, and 240 $\pm$ 30 fs, respectively. These agree with previous measurements that showed that bare nanotubes recombine excitons quickly due to high amounts of cross-linking[251]. They also show that the MWCNT recombines faster than the SWCNT, despite less cross-linking.

Bibliography

(1) Brinks, D.; Hildner, R.; Van Dijk, E. M.; Stefani, F. D.; Nieder, J. B.; Hernando, J.; Van Hulst, N. F. Ultrafast dynamics of single molecules. *Chemical Society Reviews* **2014**, *43*, 2476–2491.

(2) Aghanim, N.; Akrami, Y.; Ashdown, M.; Aumont, J.; Baccigalupi, C.; Ballardini, M.; Banday, A.; Barreiro, R.; Bartolo, N.; Basak, S., et al. Planck 2018 results-VI. Cosmological parameters. *Astronomy & Astrophysics* **2020**, *641*, A6.

(3) Dickenson, G. D.; Niu, M. L.; Salumbides, E. J.; Komasa, J.; Eikema, K. S.; Pachucki, K.; Ubachs, W. Fundamental vibration of molecular hydrogen. *Physical review letters* **2013**, *110*, 193601.

(4) Chou, K.-C. Low-frequency vibrations of DNA molecules. *Biochemical Journal* **1984**, *221*, 27–31.

(5) Zewail, A. H. Femtochemistry: atomic-scale dynamics of the chemical bond using ultrafast lasers (Nobel Lecture). *Angewandte Chemie International Edition* **2000**, *39*, 2586–2631.

(6) Ponseca Jr, C. S.; Chabera, P.; Uhlig, J.; Persson, P.; Sundstrom, V. Ultrafast electron dynamics in solar energy conversion. *Chemical reviews* **2017**, *117*, 10940–11024.

(7) Bandaru, P. R. Electrical properties and applications of carbon nanotube structures. *Journal of nanoscience and nanotechnology* **2007**, *7*, 1239–1267.

(8) Jelezko, F.; Wrachtrup, J. Single defect centres in diamond: A review. *physica status solidi (a)* **2006**, *203*, 3207–3225.

(9) Dong, P.-T.; Cheng, J.-X. Pump–probe microscopy: theory, instrumentation, and applications. *Spectroscopy* **2017**, *32*, 2–11.

(10) Jager, M. F.; Ott, C.; Kraus, P. M.; Kaplan, C. J.; Pouse, W.; Marvel, R. E.; Haglund, R. F.; Neumark, D. M.; Leone, S. R. Tracking the insulator-to-metal phase transition in VO2 with few-femtosecond extreme UV transient absorption spectroscopy. *Proceedings of the National Academy of Sciences* **2017**, *114*, 9558–9563.

(11) Berera, R.; van Grondelle, R.; Kennis, J. Ultrafast transient absorption spectroscopy: principles and application to photosynthetic systems. *Photosynthesis research* **2009**, *101*, 105–118.

(12) Vrakking, M. J. Showtime for Molecular Movies. *Physics* **2016**, *9*, 112.

(13) Busch, P.; Heinonen, T.; Lahti, P. Heisenberg's uncertainty principle. *Physics Reports* **2007**, *452*, 155–176.

(14) Attwood, D.; Sakdinawat, A. In *X-Rays and Extreme Ultraviolet Radiation: Principles and Applications*, 2nd ed.; Cambridge University Press: 2017, pp 279–314.

(15) Kaplan, C. J.; Kraus, P. M.; Ross, A. D.; Zürch, M.; Cushing, S. K.; Jager, M. F.; Chang, H.-T.; Gullikson, E. M.; Neumark, D. M.; Leone, S. R. Femtosecond tracking of carrier relaxation in germanium with extreme ultraviolet transient reflectivity. *Physical Review B* **2018**, *97*, 205202.

(16) Coherent Legend Elite PreInstallation, 2022.

(17) Timmers, H.; Zhu, X.; Li, Z.; Kobayashi, Y.; Sabbar, M.; Hollstein, M.; Reduzzi, M.; Martınez, T. J.; Neumark, D. M.; Leone, S. R. Disentangling conical intersection and coherent molecular dynamics in methyl bromide with attosecond transient absorption spectroscopy. *Nature Communications* **2019**, *10*, 3133.

(18) Fidler, A. P.; Camp, S. J.; Warrick, E. R.; Bloch, E.; Marroux, H. J. B.; Neumark, D. M.; Schafer, K. J.; Gaarde, M. B.; Leone, S. R. Nonlinear XUV signal generation probed by transient grating spectroscopy with attosecond pulses. *Nature Communications* **2019**, *10*, 1384.

(19) Elkins, M. H.; Williams, H. L.; Shreve, A. T.; Neumark, D. M. Relaxation mechanism of the hydrated electron. *Science* **2013**, *342*, 1496–1499.

(20) Scherer, N. F.; Carlson, R. J.; Matro, A.; Du, M.; Ruggiero, A. J.; Romero-Rochin, V.; Cina, J. A.; Fleming, G. R.; Rice, S. A. Fluorescence-detected wave packet interferometry: Time resolved molecular spectroscopy with sequences of femtosecond phase-locked pulses. *The Journal of chemical physics* **1991**, *95*, 1487–1511.

(21) Pertot, Y.; Schmidt, C.; Matthews, M.; Chauvet, A.; Huppert, M.; Svoboda, V.; von Conta, A.; Tehlar, A.; Baykusheva, D.; Wolf, J.-P.; Wörner, H. J. Time-resolved x-ray absorption spectroscopy with a water window high-harmonic source. *Science* **2017**, *355*, 264–267.

(22) Li, J.; Lu, J.; Chew, A.; Han, S.; Li, J.; Wu, Y.; Wang, H.; Ghimire, S.; Chang, Z. Attosecond science based on high harmonic generation from gases and solids. *Nature Communications* **2020**, *11*, 1–13.

(23) Gaumnitz, T.; Jain, A.; Pertot, Y.; Huppert, M.; Jordan, I.; Ardana-Lamas, F.; Wörner, H. J. Streaking of 43-attosecond soft-X-ray pulses generated by a passively CEP-stable mid-infrared driver. *Optics express* **2017**, *25*, 27506–27518.

(24) Geneaux, R.; Marroux, H. J. B.; Guggenmos, A.; Neumark, D. M.; Leone, S. R. Transient absorption spectroscopy using high harmonic generation: a review of ultrafast X-ray dynamics in molecules and solids. *Philosophical Transactions of the Royal Society A: Mathematical, Physical and Engineering Sciences* **2019**, *377*, 20170463.

(25) B.L. Henke, E. G.; Davis, J. X-ray interactions: photoabsorption, scattering, transmission, and reflection at E=50-30000 eV, Z=1-92. *Atomic Data and Nuclear Data Tables* **July 1993**, *54*, 181–342.

(26) Vura-Weis, J.; Jiang, C.-M.; Liu, C.; Gao, H.; Lucas, J. M.; de Groot, F. M. F.; Yang, P.; Alivisatos, A. P.; Leone, S. R. Femtosecond M2,3-Edge Spectroscopy of Transition-Metal Oxides: Photoinduced Oxidation State Change in Î±-Fe2O3. *The Journal of Physical Chemistry Letters* **2013**, *4*, 3667–3671.

(27) Vleck, J. V. The Puzzle of Rare-earth Spectra in Solids. *Journal of physical chemistry* **1937**, *41*, 67–80.

(28) Zürch, M.; Chang, H.-T.; Borja, L. J.; Kraus, P. M.; Cushing, S. K.; Gandman, A.; Kaplan, C. J.; Oh, M. H.; Prell, J. S.; Prendergast, D., et al. Direct and simultaneous observation of ultrafast electron and hole dynamics in germanium. *Nature communications* **2017**, *8*, 1–11.

(29) Camara, C. G.; Escobar, J. V.; Hird, J. R.; Putterman, S. J. Correlation between nanosecond X-ray flashes and stick–slip friction in peeling tape. *nature* **2008**, *455*, 1089–1092.

(30) Arslan, M.; KACAR, İ.; YADİGAROĞLU, T.; MUHSUROĞLU, M. Design and production of a fixed anode x-ray tube. *International Advanced Researches and Engineering Journal* **2018**, *2*, 153–158.

(31) Bilderback, D. H.; Elleaume, P.; Weckert, E. Review of third and next generation synchrotron light sources. *Journal of Physics B: Atomic, molecular and optical physics* **2005**, *38*, S773.

(32) Jaeschke, E. J.; Khan, S.; Schneider, J. R.; Hastings, J. B., *Synchrotron light sources and free-electron lasers: accelerator physics, instrumentation and science applications*; Springer: 2016.

(33) Kulipanov, G.; Skrinsky, A.; Vinokurov, N. Synchrotron light sources and recent developments of accelerator technology. *Journal of Synchrotron Radiation* **1998**, *5*, 176–178.

(34) Attwood, D.; Sakdinawat, A. In *X-Rays and Extreme Ultraviolet Radiation: Principles and Applications*, 2nd ed.; Cambridge University Press: 2017, pp 148–226.

(35) Decker, G. In *Proceedings of DIPAC*, 2005; Vol. 5.

(36) Attwood, D.; Sakdinawat, A. In *X-Rays and Extreme Ultraviolet Radiation: Principles and Applications*, 2nd ed.; Cambridge University Press: 2017, pp 227–278.

(37) Hartmann, N.; Hartmann, G.; Heider, R.; Wagner, M.; Ilchen, M.; Buck, J.; Lindahl, A.; Benko, C.; Grünert, J.; Krzywinski, J., et al. Attosecond time–energy structure of X-ray free-electron laser pulses. *Nature Photonics* **2018**, *12*, 215–220.

(38) Nam, I.; Min, C.-K.; Oh, B.; Kim, G.; Na, D.; Suh, Y. J.; Yang, H.; Cho, M. H.; Kim, C.; Kim, M.-J., et al. High-brightness self-seeded X-ray free-electron laser covering the 3.5 keV to 14.6 keV range. *Nature Photonics* **2021**, *15*, 435–441.

(39) Ackermann, W. a.; Asova, G.; Ayvazyan, V.; Azima, A.; Baboi, N.; Bähr, J.; Balandin, V.; Beutner, B.; Brandt, A.; Bolzmann, A., et al. Operation of a free-electron laser from the extreme ultraviolet to the water window. *Nature photonics* **2007**, *1*, 336–342.

(40) Kelly, J.; Knottenbelt, W. The UK-DALE dataset, domestic appliance-level electricity demand and whole-house demand from five UK homes. *Scientific data* **2015**, *2*, 1–14.

(41) Eden, J. G. High-order harmonic generation and other intense optical field–matter interactions: review of recent experimental and theoretical advances. *Progress in Quantum Electronics* **2004**, *28*, 197–246.

(42) Teichmann, S. M.; Silva, F.; Cousin, S.; Hemmer, M.; Biegert, J. 0.5-keV Soft X-ray attosecond continua. *Nature Communications* **2016**, *7*, 1–6.

(43) Johnson, A. S.; Austin, D. R.; Wood, D. A.; Brahms, C.; Gregory, A.; Holzner, K. B.; Jarosch, S.; Larsen, E. W.; Parker, S.; Strüber, C. S., et al. High-flux soft x-ray harmonic generation from ionization-shaped few-cycle laser pulses. *Science advances* **2018**, *4*, eaar3761.

(44) Amini, K.; Biegert, J.; Calegari, F.; Chacón, A.; Ciappina, M. F.; Dauphin, A.; Efimov, D. K.; de Morisson Faria, C. F.; Giergiel, K.; Gniewek, P., et al. Symphony on strong field approximation. *Reports on Progress in Physics* **2019**, *82*, 116001.

(45) Fu, Y.; Nishimura, K.; Shao, R.; Suda, A.; Midorikawa, K.; Lan, P.; Takahashi, E. J. High efficiency ultrafast water-window harmonic generation for single-shot soft X-ray spectroscopy. *Communications Physics* **2020**, *3*, 1–10.

(46) Eckardt, R.; Reintjes, J. Phase matching limitations of high efficiency second harmonic generation. *IEEE journal of quantum electronics* **1984**, *20*, 1178–1187.

(47) Grinblat, G.; Li, Y.; Nielsen, M. P.; Oulton, R. F.; Maier, S. A. Efficient third harmonic generation and nonlinear subwavelength imaging at a higher-order anapole mode in a single germanium nanodisk. *ACS nano* **2017**, *11*, 953–960.

(48) Corkum, P. B. Plasma perspective on strong field multiphoton ionization. *Physical review letters* **1993**, *71*, 1994.

(49) Schafer, K.; Yang, B.; DiMauro, L.; Kulander, K. Above threshold ionization beyond the high harmonic cutoff. *Physical review letters* **1993**, *70*, 1599.

(50) Ge, X.-L.; Du, H.; Guo, J.; Liu, X.-S. Quantum control of electron wave packet during high harmonic process of H2+ in a combination of a circularly polarized laser field and a Terahertz field. *Optics Express* **2015**, *23*, 8837–8844.

(51) Severt, T.; Tross, J.; Kolliopoulos, G.; Ben-Itzhak, I.; Trallero-Herrero, C. Enhancing high-order harmonic generation by controlling the diffusion of the electron wave packet. *Optica* **2021**, *8*, 1113–1121.

(52) Kohler, M. C.; Ott, C.; Raith, P.; Heck, R.; Schlegel, I.; Keitel, C. H.; Pfeifer, T. High harmonic generation via continuum wave-packet interference. *Physical review letters* **2010**, *105*, 203902.

(53) A. Kramida; Yu. Ralchenko; J. Reader; and NIST ASD Team, NIST Atomic Spectra Database (ver. 5.9), [Online]. Available: https://physics.nist.gov/asd [2017, April 9]. National Institute of Standards and Technology, Gaithersburg, MD. 2021.

(54) Amplitude Product Finder, 2022.

(55) Spectra Physics fs Research Lasers, 2022.

(56) Fan, H.; Pratt, S. Photoionization of hot radicals: C 2 H 5, n-C 3 H 7, and i-C 3 H 7. *The Journal of chemical physics* **2005**, *123*, 204301.

(57) Zou, P.; Strecker, K. E.; Ramirez-Serrano, J.; Jusinski, L. E.; Taatjes, C. A.; Osborn, D. L. Ultraviolet photodissociation of vinyl iodide: Understanding the halogen dependence of photodissociation mechanisms in vinyl halides. *Physical Chemistry Chemical Physics* **2008**, *10*, 713–728.

(58) Ren, X.; Li, J.; Yin, Y.; Zhao, K.; Chew, A.; Wang, Y.; Hu, S.; Cheng, Y.; Cunningham, E.; Wu, Y., et al. Attosecond light sources in the water window. *Journal of Optics* **2018**, *20*, 023001.

(59) Shiner, A. D.; Trallero-Herrero, C.; Kajumba, N.; Bandulet, H.-C.; Comtois, D.; Légaré, F.; Giguère, M.; Kieffer, J.-C.; Corkum, P. B.; Villeneuve, D. M. Wavelength Scaling of High Harmonic Generation Efficiency. *Phys. Rev. Lett.* **2009**, *103*, 073902.

(60) Attar, A. R.; Bhattacherjee, A.; Pemmaraju, C.; Schnorr, K.; Closser, K. D.; Prendergast, D.; Leone, S. R. Femtosecond x-ray spectroscopy of an electrocyclic ring-opening reaction. *Science* **2017**, *356*, 54–59.

(61) Kraus, P. M.; Wörner, H. J. Perspectives of attosecond spectroscopy for the understanding of fundamental electron correlations. *Angewandte Chemie International Edition* **2018**, *57*, 5228–5247.

(62) Johnson, A. S.; Wood, D.; Austin, D. R.; Brahms, C.; Gregory, A.; Holzner, K. B.; Jarosch, S.; Larsen, E. W.; Parker, S.; Strüber, C.; Ye, P.; Tisch, J. W. G.; Marangos, J. P. Apparatus for soft x-ray table-top high harmonic generation. *Review of Scientific Instruments* **2018**, *89*, 083110.

(63) Johnson, A. S.; Austin, D. R.; Wood, D. A.; Brahms, C.; Gregory, A.; Holzner, K. B.; Jarosch, S.; Larsen, E. W.; Parker, S.; Strüber, C. S.; Ye, P.; Tisch, J. W. G.; Marangos, J. P. High-flux soft x-ray harmonic generation from ionization-shaped few-cycle laser pulses. *Science Advances* **2018**, *4*, DOI: `https://doi.org/10.1126/sciadv.aar3761`.

(64) Yu, C.; Jiang, S.; Lu, R. High order harmonic generation in solids: a review on recent numerical methods. *Advances in Physics: X* **2019**, *4*, 1562982.

(65) Seres, J.; Seres, E.; Verhoef, A. J.; Tempea, G.; Streli, C.; Wobrauschek, P.; Yakovlev, V.; Scrinzi, A.; Spielmann, C.; Krausz, F. Source of coherent kiloelectronvolt X-rays. *Nature* **2005**, *433*, 596–596.

(66) Buades, B.; Picón, A.; Berger, E.; León, I.; Di Palo, N.; Cousin, S. L.; Cocchi, C.; Pellegrin, E.; Martin, J. H.; Mañas-Valero, S., et al. Attosecond state-resolved carrier motion in quantum materials probed by soft x-ray XANES. *Applied Physics Reviews* **2021**, *8*, 011408.

(67) Tang, X.; Wang, K.; Li, B.; Chen, Y.; Lin, C. D.; Jin, C. Optimal generation and isolation of attosecond pulses in an overdriven ionized medium. *Optics Letters* **2021**, *46*, 5137–5140.

(68) Major, B.; Kovács, K.; Svirplys, E.; Anus, M.; Ghafur, O.; Varjú, K.; Vrakking, M.; Tosa, V.; Schütte, B. High-harmonic generation in a strongly overdriven regime. *arXiv preprint arXiv:2203.11021* **2022**.

(69) Chini, M.; Zhao, K.; Chang, Z. The generation, characterization and applications of broadband isolated attosecond pulses. *Nature Photonics* **2014**, *8*, 178–186.

(70) Spielmann, C.; Curley, P. F.; Brabec, T.; Krausz, F. Ultrabroadband femtosecond lasers. *IEEE Journal of quantum electronics* **1994**, *30*, 1100–1114.

(71) Brabec, T.; Krausz, F. Intense few-cycle laser fields: Frontiers of nonlinear optics. *Reviews of Modern Physics* **2000**, *72*, 545.

(72) Chang, Z.; Corkum, P. Attosecond photon sources: the first decade and beyond. *JOSA B* **2010**, *27*, B9–B17.

(73) Li, J.; Ren, X.; Yin, Y.; Zhao, K.; Chew, A.; Cheng, Y.; Cunningham, E.; Wang, Y.; Hu, S.; Wu, Y., et al. 53-attosecond X-ray pulses reach the carbon K-edge. *Nature communications* **2017**, *8*, 1–5.

(74) Yuan, X.; Wei, P.; Liu, C.; Ge, X.; Zheng, Y.; Zeng, Z.; Li, R. Effect of nuclear motion on spectral broadening of high-order harmonic generation. *Opt. Express* **2016**, *24*, 8194–8201.

(75) Chang, Z.; Rundquist, A.; Wang, H.; Murnane, M. M.; Kapteyn, H. C. Generation of coherent soft X rays at 2.7 nm using high harmonics. *Physical Review Letters* **1997**, *79*, 2967–2970.

(76) Géneaux, R.; Chang, H.-T.; Schwartzberg, A. M.; Marroux, H. J. B. Source noise suppression in attosecond transient absorption spectroscopy by edge-pixel referencing. *Opt. Express* **2021**, *29*, 951–960.

(77) Bressler, C.; Chergui, M. Ultrafast X-ray absorption spectroscopy. *Chemical reviews* **2004**, *104*, 1781–1812.

(78) Friedrich, H.; Sonntag, B.; Pittel, B.; Rabe, P.; Schwarz, W. Overlapping core to valence and core to Rydberg transitions and resonances in the XUV spectra of SiF4. *Journal of Physics B: Atomic and Molecular Physics (1968-1987)* **1980**, *13*, 25.

(79) Wu, T.; Higashiguchi, T.; Li, B.; Arai, G.; Hara, H.; Kondo, Y.; Miyazaki, T.; Dinh, T.-H.; O'Reilly, F.; Sokell, E., et al. Analysis of unresolved transition arrays in XUV spectral region from highly charged lead ions produced by subnanosecond laser pulse. *Optics Communications* **2017**, *385*, 143–152.

(80) Eckstein, M.; Yang, C.-H.; Kubin, M.; Frassetto, F.; Poletto, L.; Ritze, H.-H.; Vrakking, M. J.; Kornilov, O. Dynamics of N2 dissociation upon inner-valence ionization by wavelength-selected XUV pulses. *The journal of physical chemistry letters* **2015**, *6*, 419–425.

(81) Ott, C.; Jager, M. F.; Kaplan, C. J.; Marvel, R. E.; Haglund, R. F.; Neumark, D. M.; Leone, S. R. In *International Conference on Ultrafast Phenomena*, 2016, UM1A–3.

(82) Eschenlohr, A. Spin dynamics at interfaces on femtosecond timescales. *Journal of Physics: Condensed Matter* **2020**, *33*, 013001.

(83) Kolbasova, D.; Hartmann, M.; Jin, R.; Blättermann, A.; Ott, C.; Son, S.-K.; Pfeifer, T.; Santra, R. Probing ultrafast coherent dynamics in core-excited xenon by using attosecond XUV-NIR transient absorption spectroscopy. *Physical Review A* **2021**, *103*, 043102.

(84) Epshtein, M.; Scutelnic, V.; Yang, Z.; Xue, T.; Vidal, M. L.; Krylov, A. I.; Coriani, S.; Leone, S. R. Table-Top X-ray Spectroscopy of Benzene Radical Cation. *The Journal of Physical Chemistry A* **2020**, *124*, PMID: 33107734, 9524–9531.

(85) Key, M.; Barbee Jr, T.; Da Silva, L.; Glendinning, S.; Kalantar, D.; Rose, S.; Weber, S. New plasma diagnostic possibilities from radiography with xuv lasers. *Journal of Quantitative Spectroscopy and Radiative Transfer* **1995**, *54*, 221–226.

(86) Sidiropoulos, T.; Di Palo, N.; Rivas, D.; Severino, S.; Reduzzi, M.; Nandy, B.; Bauerhenne, B.; Krylow, S.; Vasileiadis, T.; Danz, T., et al. Probing the Energy Conversion Pathways between Light, Carriers, and Lattice in Real Time with Attosecond Core-Level Spectroscopy. *Physical Review X* **2021**, *11*, 041060.

(87) Attar, A. R.; Chang, H.-T.; Britz, A.; Zhang, X.; Lin, M.-F.; Krishnamoorthy, A.; Linker, T.; Fritz, D.; Neumark, D. M.; Kalia, R. K., et al. Simultaneous observation of carrier-specific redistribution and coherent lattice dynamics in 2H-MoTe2 with femtosecond core-level spectroscopy. *ACS nano* **2020**, *14*, 15829–15840.

(88) Reitsma, G.; Patchkovskii, S.; Dura, J.; Drescher, L.; Mikosch, J.; Vrakking, M. J.; Kornilov, O. Vibrational Relaxation of XUV-Induced Hot Ground State Cations of Naphthalene. *The Journal of Physical Chemistry A* **2021**, *125*, 8549–8556.

(89) Engel, N.; Bokarev, S. I.; Moguilevski, A.; Raheem, A. A.; Al-Obaidi, R.; Möhle, T.; Grell, G.; Siefermann, K. R.; Abel, B.; Aziz, S. G., et al. Light-induced relaxation dynamics of the ferricyanide ion revisited by ultrafast XUV photoelectron spectroscopy. *Physical Chemistry Chemical Physics* **2017**, *19*, 14248–14255.

(90) Krems, R. V. Molecules in electromagnetic fields : from ultracold physics to controlled chemistry `https://search.ebscohost.com/login.aspx?direct=true&scope=site&db=nlebk&db=nlabk&AN=1814516`.

(91) Barreau, L.; Ross, A. D.; Garg, S.; Kraus, P. M.; Neumark, D. M.; Leone, S. R. Efficient table-top dual-wavelength beamline for ultrafast transient absorption spectroscopy in the soft X-ray region. *Scientific Reports* **2020**, *10*, 5773.

(92) Van Dao, L.; Tran, K. A.; Hannaford, P. Cascaded four-wave mixing in the XUV region. *Optics Letters* **2018**, *43*, 134–137.

(93) Ott, C.; Kaldun, A.; Argenti, L.; Raith, P.; Meyer, K.; Laux, M.; Zhang, Y.; Blättermann, A.; Hagstotz, S.; Ding, T., et al. Reconstruction and control of a time-dependent two-electron wave packet. *Nature* **2014**, *516*, 374.

(94) Géneaux, R.; Timrov, I.; Kaplan, C. J.; Ross, A. D.; Kraus, P. M.; Leone, S. R. Coherent energy exchange between carriers and phonons in Peierls-distorted bismuth unveiled by broadband XUV pulses. *Physical Review Research* **2021**, *3*, 033210.

(95) Teichmann, S. M.; Silva, F.; Cousin, S. L.; Hemmer, M.; Biegert, J. 0.5-keV Soft X-ray attosecond continua. *Nature Communications* **2016**, *7*, 11493.

(96) Stoicheff, B. High resolution Raman spectroscopy of gases: XI. Spectra of CS2 and CO2. *Canadian Journal of Physics* **1958**, *36*, 218–230.

(97) Parija, A.; Choi, Y.-H.; Liu, Z.; Andrews, J. L.; De Jesus, L. R.; Fakra, S. C.; Al-Hashimi, M.; Batteas, J. D.; Prendergast, D.; Banerjee, S. Mapping catalytically relevant edge electronic states of MoS2. *ACS central science* **2018**, *4*, 493–503.

(98) Nisoli, M.; De Silvestri, S.; Svelto, O.; Szipöcs, R.; Ferencz, K.; Spielmann, C.; Sartania, S.; Krausz, F. Compression of high-energy laser pulses below 5 fs. *Optics Letters* **1997**, *22*, 522–524.

(99) Giguère, M.; Schmidt, B. E.; Shiner, A. D.; Houle, M.-A.; Bandulet, H. C.; Tempea, G.; Villeneuve, D. M.; Kieffer, J.-C.; Légaré, F. Pulse compression of submillijoule few-optical-cycle infrared laser pulses using chirped mirrors. *Opt. Lett.* **2009**, *34*, 1894–1896.

(100) Mahieu, B.; Gauthier, D.; Perdrix, M.; Ge, X.; Boutu, W.; Lepetit, F.; Wang, F.; Carré, B.; Auguste, T.; Merdji, H., et al. Spatial quality improvement of a Ti: Sapphire laser beam by modal filtering. *Applied Physics B* **2015**, *118*, 47–60.

(101) Timmers, H.; Kobayashi, Y.; Chang, K. F.; Reduzzi, M.; Neumark, D. M.; Leone, S. R. Generating high-contrast, near single-cycle waveforms with third-order dispersion compensation. *Opt. Lett.* **2017**, *42*, 811–814.

(102) Silva, F.; Miranda, M.; Alonso, B.; Rauschenberger, J.; Pervak, V.; Crespo, H. Simultaneous compression, characterization and phase stabilization of GW-level 1.4 cycle VIS-NIR femtosecond pulses using a single dispersion-scan setup. *Optics Express* **2014**, *22*, 10181–10191.

(103) Kobayashi, Y.; Chang, K. F.; Zeng, T.; Neumark, D. M.; Leone, S. R. Direct mapping of curve-crossing dynamics in IBr by attosecond transient absorption spectroscopy. *Science* **2019**, *365*, 79–83.

(104) Ishii, N.; Kaneshima, K.; Kanai, T.; Watanabe, S.; Itatani, J. Generation of sub-two-cycle millijoule infrared pulses in an optical parametric chirped-pulse amplifier and their application to soft x-ray absorption spectroscopy with high-flux high harmonics. *Journal of Optics* **2018**, *20*, 014003.

(105) Li, J.; Ren, X.; Yin, Y.; Zhao, K.; Chew, A.; Cheng, Y.; Cunningham, E.; Wang, Y.; Hu, S.; Wu, Y.; Chini, M.; Chang, Z. 53-attosecond X-ray pulses reach the carbon K-edge. *Nature Communications* **2017**, *8*, 1–5.

(106) Bor, Z. Distortion of Femtosecond Laser Pulses in Lenses and Lens Systems. *Journal of Modern Optics* **1988**, *35*, 1907–1918.

(107) Sairanen, O.-P.; Kivimäki, A.; Nõmmiste, E.; Aksela, H.; Aksela, S. High-resolution pre-edge structure in the inner-shell ionization threshold region of rare gases Xe, Kr, and Ar. *Phys. Rev. A* **1996**, *54*, 2834–2839.

(108) Tate, J.; Auguste, T.; Muller, H. G.; Salières, P.; Agostini, P.; DiMauro, L. F. Scaling of Wave-Packet Dynamics in an Intense Midinfrared Field. *Phys. Rev. Lett.* **2007**, *98*, 013901.

(109) Krause, J. L.; Schafer, K. J.; Kulander, K. C. High-order harmonic generation from atoms and ions in the high intensity regime. *Phys. Rev. Lett.* **1992**, *68*, 3535–3538.

(110) Popmintchev, T.; Chen, M.-C.; Bahabad, A.; Gerrity, M.; Sidorenko, P.; Cohen, O.; Christov, I. P.; Murnane, M. M.; Kapteyn, H. C. Phase matching of high harmonic generation in the soft and hard X-ray regions of the spectrum. *Proceedings of the National Academy of Sciences* **2009**, *106*, 10516–10521.

(111) Takahashi, E. J.; Kanai, T.; Ishikawa, K. L.; Nabekawa, Y.; Midorikawa, K. Coherent water window X ray by phase-matched high-order harmonic generation in neutral media. *Physical Review Letters* **2008**, *101*, 253901.

(112) Chen, M.-C.; Arpin, P.; Popmintchev, T.; Gerrity, M.; Zhang, B.; Seaberg, M.; Popmintchev, D.; Murnane, M. M.; Kapteyn, H. C. Bright, coherent, ultrafast soft X-ray harmonics spanning the water window from a tabletop light source. *Physical Review Letters* **2010**, *105*, 173901.

(113) Constant, E.; Garzella, D.; Breger, P.; Mével, E.; Dorrer, C.; Le Blanc, C.; Salin, F.; Agostini, P. Optimizing High Harmonic Generation in Absorbing Gases: Model and Experiment. *Phys. Rev. Lett.* **1999**, *82*, 1668–1671.

(114) Sutherland, J. R.; Christensen, E. L.; Powers, N. D.; Rhynard, S. E.; Painter, J. C.; Peatross, J. High harmonic generation in a semi-infinite gas cell. *Optics Express* **2004**, *12*, 4430–4436.

(115) Saito, N.; Sannohe, H.; Ishii, N.; Kanai, T.; Kosugi, N.; Wu, Y.; Chew, A.; Han, S.; Chang, Z.; Itatani, J. Real-time observation of electronic, vibrational, and rotational dynamics in nitric oxide with attosecond soft x-ray pulses at 400 eV. *Optica* **2019**, *6*, 1542–1546.

(116) Baltuška, A.; Udem, T.; Uiberacker, M.; Hentschel, M.; Goulielmakis, E.; Gohle, C.; Holzwarth, R.; Yakovlev, V.; Scrinzi, A.; Hänsch, T. W., et al. Attosecond control of electronic processes by intense light fields. *Nature* **2003**, *421*, 611.

(117) Cousin, S. L.; Di Palo, N.; Buades, B.; Teichmann, S. M.; Reduzzi, M.; Devetta, M.; Kheifets, A.; Sansone, G.; Biegert, J. Attosecond streaking in the water window: a new regime of attosecond pulse characterization. *Physical Review X* **2017**, *7*, 041030.

(118) Schibli, T. R.; Kim, J.; Kuzucu, O.; Gopinath, J. T.; Tandon, S. N.; Petrich, G. S.; Kolodziejski, L. A.; Fujimoto, J. G.; Ippen, E. P.; Kaertner, F. X. Attosecond active synchronization of passively mode-locked lasers by balanced cross correlation. *Opt. Lett.* **2003**, *28*, 947–949.

(119) Wang, H.; Chini, M.; Chen, S.; Zhang, C.-H.; He, F.; Cheng, Y.; Wu, Y.; Thumm, U.; Chang, Z. Attosecond time-resolved autoionization of argon. *Physical Review Letters* **2010**, *105*, 143002.

(120) Beck, A. R.; Bernhardt, B.; Warrick, E. R.; Wu, M.; Chen, S.; Gaarde, M. B.; Schafer, K. J.; Neumark, D. M.; Leone, S. R. Attosecond transient absorption probing of electronic superpositions of bound states in neon: detection of quantum beats. *New Journal of Physics* **2014**, *16*, 113016.

(121) Chew, A.; Douguet, N.; Cariker, C.; Li, J.; Lindroth, E.; Ren, X.; Yin, Y.; Argenti, L.; Hill, W. T.; Chang, Z. Attosecond transient absorption spectrum of argon at the $L_{2,3}$ edge. *Phys. Rev. A* **2018**, *97*, 031407.

(122) Manzoni, C.; Huang, S.-W.; Cirmi, G.; Farinello, P.; Moses, J.; Kärtner, F.; Cerullo, G. Coherent synthesis of ultra-broadband optical parametric amplifiers. *Optics letters* **2012**, *37*, 1880–1882.

(123) Miron, C.; Nicolas, C.; Travnikova, O.; Morin, P.; Sun, Y.; Gel'mukhanov, F.; Kosugi, N.; Kimberg, V. Imaging molecular potentials using ultrahigh-resolution resonant photoemission. *Nature Physics* **2012**, *8*, 135–138.

(124) Kimberg, V.; Miron, C. Molecular potentials and wave function mapping by high-resolution electron spectroscopy and ab initio calculations. *Journal of Electron Spectroscopy and Related Phenomena* **2014**, *195*, 301–306.

(125) Schreck, S.; Pietzsch, A.; Kennedy, B.; Såthe, C.; Miedema, P. S.; Techert, S.; Strocov, V. N.; Schmitt, T.; Hennies, F.; Rubensson, J.-E., et al. Ground state potential energy surfaces around selected atoms from resonant inelastic x-ray scattering. *Scientific reports* **2016**, *6*, 1–8.

(126) Eckert, S.; da Cruz, V. V.; Gel'mukhanov, F.; Ertan, E.; Ignatova, N.; Polyutov, S.; Couto, R. C.; Fondell, M.; Dantz, M.; Kennedy, B., et al. One-dimensional cuts through multidimensional potential-energy surfaces by tunable x rays. *Physical Review A* **2018**, *97*, 053410.

(127) Vaz da Cruz, V.; Gel'mukhanov, F.; Eckert, S.; Iannuzzi, M.; Ertan, E.; Pietzsch, A.; Couto, R. C.; Niskanen, J.; Fondell, M.; Dantz, M., et al. Probing hydrogen bond strength in liquid water by resonant inelastic X-ray scattering. *Nature communications* **2019**, *10*, 1–9.

(128) Gelmukhanov, F.; Ågren, H. X-ray resonant scattering involving dissociative states. *Physical Review A* **1996**, *54*, 379.

(129) Simon, M.; Miron, C.; Leclercq, N.; Morin, P.; Ueda, K.; Sato, Y.; Tanaka, S.; Kayanuma, Y. Nuclear Motion of Core Excited BF 3 Probed by High Resolution Resonant Auger Spectroscopy. *Physical review letters* **1997**, *79*, 3857.

(130) Marchenko, T.; Goldsztejn, G.; Jänkälä, K.; Travnikova, O.; Journel, L.; Guillemin, R.; Sisourat, N.; Céolin, D.; Žitnik, M.; Kavčič, M., et al. Potential energy surface reconstruction and lifetime determination of molecular double-core-hole states in the hard x-ray regime. *Physical Review Letters* **2017**, *119*, 133001.

(131) Prince, K. C.; Richter, R.; de Simone, M.; Alagia, M.; Coreno, M. Near edge X-ray absorption spectra of some small polyatomic molecules. *The Journal of Physical Chemistry A* **2003**, *107*, 1955–1963.

(132) Vaz da Cruz, V.; Ignatova, N.; Couto, R. C.; Fedotov, D. A.; Rehn, D. R.; Savchenko, V.; Norman, P.; Ågren, H.; Polyutov, S.; Niskanen, J., et al. Nuclear dynamics in resonant inelastic X-ray scattering and X-ray absorption of methanol. *The Journal of chemical physics* **2019**, *150*, 234301.

(133) Hait, D.; Head-Gordon, M. Highly Accurate Prediction of Core Spectra of Molecules at Density Functional Theory Cost: Attaining Sub-electronvolt Error from a Restricted Open-Shell Kohn–Sham Approach. *J. Phys. Chem. Lett.* **2020**, *11*, 775–786.

(134) Yan, Y.-X.; Gamble Jr, E. B.; Nelson, K. A. Impulsive stimulated scattering: General importance in femtosecond laser pulse interactions with matter, and spectroscopic applications. *The Journal of chemical physics* **1985**, *83*, 5391–5399.

(135) Yan, Y.-X.; Nelson, K. A. Impulsive stimulated light scattering. I. General theory. *The Journal of chemical physics* **1987**, *87*, 6240–6256.

(136) Carniato, S.; Taıeb, R.; Guillemin, R.; Journel, L.; Simon, M.; Gel'mukhanov, F. K–L resonant X-ray Raman scattering as a tool for potential energy surface mapping. *Chemical physics letters* **2007**, *439*, 402–406.

(137) Schmidt, B.; Hartmann, C. WavePacket: A Matlab package for numerical quantum dynamics. II: Open quantum systems, optimal control, and model reduction. *Computer Physics Communications* **2018**, *228*, 229–244.

(138) Schmidt, B.; Klein, R.; Cancissu Araujo, L. WavePacket: A Matlab package for numerical quantum dynamics. III. Quantum-classical simulations and surface hopping trajectories. *Journal of Computational Chemistry* **2019**, *40*, 2677–2688.

(139) Schmidt, B.; Klein, R.; Cancissu Araujo, L. WavePacket: A Matlab package for numerical quantum dynamics. III. Quantum-classical simulations and surface hopping trajectories. *Journal of Computational Chemistry* **2019**, *40*, 2677–2688.

(140) Korn, G.; Dühr, O.; Nazarkin, A. Observation of Raman self-conversion of fs-pulse frequency due to impulsive excitation of molecular vibrations. *Physical review letters* **1998**, *81*, 1215.

(141) Gerber, S.; Yang, S.-L.; Zhu, D.; Soifer, H.; Sobota, J.; Rebec, S.; Lee, J.; Jia, T.; Moritz, B.; Jia, C., et al. Femtosecond electron-phonon lock-in by photoemission and x-ray free-electron laser. *Science* **2017**, *357*, 71–75.

(142) Bhattacherjee, A.; Leone, S. R. Ultrafast X-ray transient absorption spectroscopy of gas-phase photochemical reactions: A new universal probe of photoinduced molecular dynamics. *Accounts of chemical research* **2018**, *51*, 3203–3211.

(143) Liao, C.-T.; Li, X.; Haxton, D. J.; Rescigno, T. N.; Lucchese, R. R.; McCurdy, C. W.; Sandhu, A. Probing autoionizing states of molecular oxygen with XUV transient absorption: Electronic-symmetry-dependent line shapes and laser-induced modifications. *Physical Review A* **2017**, *95*, 043427.

(144) Hudson, E.; Shirley, D. A.; Domke, M.; Remmers, G.; Puschmann, A.; Mandel, T.; Xue, C.; Kaindl, G. High-resolution measurements of near-edge resonances in the core-level photoionization spectra of SF_6. *Phys. Rev. A* **1993**, *47*, 361–373.

(145) Stener, M.; Bolognesi, P.; Coreno, M.; O'Keeffe, P.; Feyer, V.; Fronzoni, G.; Decleva, P.; Avaldi, L.; Kivimäki, A. Photoabsorption and S 2p photoionization of the SF6 molecule: Resonances in the excitation energy range of 200–280 eV. *The Journal of chemical physics* **2011**, *134*, 174311.

(146) Kivimäki, A.; Coreno, M.; Miotti, P.; Frassetto, F.; Poletto, L.; Stråhlman, C.; De Simone, M.; Richter, R. The multielectron character of the S 2p→ 4eg shape resonance in the SF6 molecule studied via detection of soft X-ray emission and neutral high-Rydberg fragments. *Journal of Electron Spectroscopy and Related Phenomena* **2016**, *209*, 26–33.

(147) Besley, N. A.; Asmuruf, F. A. Time-dependent density functional theory calculations of the spectroscopy of core electrons. *Physical Chemistry Chemical Physics* **2010**, *12*, 12024–12039.

(148) Dreuw, A.; Head-Gordon, M. Single-reference ab initio methods for the calculation of excited states of large molecules. *Chemical reviews* **2005**, *105*, 4009–4037.

(149) Claassen, H. H.; Goodman, G. L.; Holloway, J. H.; Selig, H. Raman spectra of MoF6, TcF6, ReF6, UF6, SF6, SeF6, and TeF6 in the vapor state. *The Journal of Chemical Physics* **1970**, *53*, 341–348.

(150) Wagner, N. L.; Wüest, A.; Christov, I. P.; Popmintchev, T.; Zhou, X.; Murnane, M. M.; Kapteyn, H. C. Monitoring molecular dynamics using coherent electrons from high harmonic generation. *Proceedings of the National Academy of Sciences* **2006**, *103*, 13279–13285.

(151) Ferré, A.; Staedter, D.; Burgy, F.; Dagan, M.; Descamps, D.; Dudovich, N.; Petit, S.; Soifer, H.; Blanchet, V.; Mairesse, Y. High-order harmonic transient grating spectroscopy of SF6 molecular vibrations. *Journal of Physics B: Atomic, Molecular and Optical Physics* **2014**, *47*, 124023.

(152) Ferré, A.; Boguslavskiy, A.; Dagan, M.; Blanchet, V.; Bruner, B.; Burgy, F.; Camper, A.; Descamps, D.; Fabre, B.; Fedorov, N., et al. Multi-channel electronic and vibrational dynamics in polyatomic resonant high-order harmonic generation. *Nature Communications* **2015**, *6*, 1–10.

(153) Baykusheva, D.; Ahsan, M. S.; Lin, N.; Wörner, H. J. Bicircular high-harmonic spectroscopy reveals dynamical symmetries of atoms and molecules. *Physical Review Letters* **2016**, *116*, 123001.

(154) Dota, K.; Dharmadhikari, A. K.; Dharmadhikari, J. A.; Patra, K.; Tiwari, A. K.; Mathur, D. A search for the sulphur hexafluoride cation with intense, few cycle laser pulses. *The Journal of Chemical Physics* **2013**, *139*, 194302.

(155) Attwood, D.; Sakdinawat, A. In *X-Rays and Extreme Ultraviolet Radiation: Principles and Applications*, 2nd ed.; Cambridge University Press: 2017, pp 620–621.

(156) Larochelle, S.; Talebpour, A.; Chin, S. Coulomb effect in multiphoton ionization of rare-gas atoms. *Journal of Physics B: Atomic, Molecular and Optical Physics* **1998**, *31*, 1215.

(157) Wang, R.; Zhang, Q.; Li, D.; Xu, S.; Cao, P.; Zhou, Y.; Cao, W.; Lu, P. Identification of tunneling and multiphoton ionization in intermediate Keldysh parameter regime. *Optics Express* **2019**, *27*, 6471–6482.

(158) Hohenberg, P.; Kohn, W. Inhomogeneous electron gas. *Physical review* **1964**, *136*, B864.

(159) Schmidt, M. W.; Baldridge, K. K.; Boatz, J. A.; Elbert, S. T.; Gordon, M. S.; Jensen, J. H.; Koseki, S.; Matsunaga, N.; Nguyen, K. A.; Su, S., et al. General atomic and molecular electronic structure system. *Journal of computational chemistry* **1993**, *14*, 1347–1363.

(160) Becke, A. Density-functional thermochemistry. III. The role of exact exchange (1993) J. *Chem. Phys*, *98*, 5648.

(161) Weigend, F.; Ahlrichs, R. Balanced basis sets of split valence, triple zeta valence and quadruple zeta valence quality for H to Rn: Design and assessment of accuracy. *Physical Chemistry Chemical Physics* **2005**, *7*, 3297–3305.

(162) Runge, E.; Gross, E. K. Density-functional theory for time-dependent systems. *Physical Review Letters* **1984**, *52*, 997.

(163) Neese, F. Software update: the ORCA program system, version 4.0. *Wiley Interdisciplinary Reviews: Computational Molecular Science* **2018**, *8*, e1327.

(164) Neese, F.; Valeev, E. F. Revisiting the atomic natural orbital approach for basis sets: Robust systematic basis sets for explicitly correlated and conventional correlated ab initio methods? *Journal of chemical theory and computation* **2011**, *7*, 33–43.

(165) Kendall, R. A.; Früchtl, H. A. The impact of the resolution of the identity approximate integral method on modern ab initio algorithm development. *Theoretical Chemistry Accounts* **1997**, *97*, 158–163.

(166) De Souza, B.; Farias, G.; Neese, F.; Izsak, R. Predicting phosphorescence rates of light organic molecules using time-dependent density functional theory and the path integral approach to dynamics. *Journal of chemical theory and computation* **2019**, *15*, 1896–1904.

(167) Lu, K.; Chen, J.; Lee, J.; Haw, S.; Chou, T.; Chen, S.; Chen, T. Core-level anionic photofragmentation of gaseous CCl 4 and solid-state analogs. *Physical Review A* **2009**, *80*, 033406.

(168) Fock, J.-H.; Koch, E.-E. Shape resonances and partial photoemission cross sections of solid SF6 and CCl4. *Chemical physics* **1985**, *96*, 125–143.

(169) Chakraborty, T.; Verma, A. Vibrational spectra of CCl4: isotopic components and hot bands. Part I. *Spectrochimica Acta Part A: Molecular and Biomolecular Spectroscopy* **2002**, *58*, 1013–1023.

(170) Gaynor, J. D.; Wetterer, A. M.; Cochran, R. M.; Valente, E. J.; Mayer, S. G. Vibrational Spectroscopy of the CCl4 v 1 Mode: Theoretical Prediction of Isotopic Effects. *Journal of Chemical Education* **2015**, *92*, 1081–1085.

(171) Hitchcock, A.; Brion, C. Inner-shell excitation and EXAFS-type phenomena in the chloromethanes. *Journal of Electron Spectroscopy and Related Phenomena* **1978**, *14*, 417–441.

(172) Lu, K.; Chen, J.; Lee, J.; Chen, C.; Chou, T.; Chen, H. State-specific dissociation enhancement of ionic and excited neutral photofragments of gaseous CCl4 and solid-state analogs following Cl 2p core-level excitation. *New Journal of Physics* **2008**, *10*, 053009.

(173) Briggs, D.; Grant, J. T., *Surface analysis by Auger and X-ray photoelectron spectroscopy*; SurfaceSpectra: 2012.

(174) Epifanovsky, E. et al. Software for the frontiers of quantum chemistry: An overview of developments in the Q-Chem 5 package. *J. Chem. Phys.* **2021**, *155*, 084801.

(175) Mardirossian, N.; Head-Gordon, M. ω B97M-V: A combinatorially optimized, range-separated hybrid, meta-GGA density functional with VV10 nonlocal correlation. *J. Chem. Phys.* **2016**, *144*, 214110.

(176) Jensen, F. Unifying general and segmented contracted basis sets. Segmented polarization consistent basis sets. *J. Chem. Theory Comput.* **2014**, *10*, 1074–1085.

(177) Raghavachari, K.; Trucks, G. W.; Pople, J. A.; Head-Gordon, M. A fifth-order perturbation comparison of electron correlation theories. *Chemical Physics Letters* **1989**, *157*, 479–483.

(178) Hait, D.; Head-Gordon, M. Orbital optimized density functional theory for electronic excited states. *J. Phys. Chem. Lett.* **2021**, *12*, 4517–4529.

(179) Sun, J.; Ruzsinszky, A.; Perdew, J. P. Strongly Constrained and Appropriately Normed Semilocal Density Functional. *Phys. Rev. Lett.* **2015**, *115*, 036402.

(180) Hait, D.; Haugen, E. A.; Yang, Z.; Oosterbaan, K. J.; Leone, S. R.; Head-Gordon, M. Accurate prediction of core-level spectra of radicals at density functional theory cost via square gradient minimization and recoupling of mixed configurations. *J. Chem. Phys.* **2020**, *153*, 134108.

(181) Hait, D.; Head-Gordon, M. Excited state orbital optimization via minimizing the square of the gradient: General approach and application to singly and doubly excited states via density functional theory. *J. Chem. Theory Comput.* **2020**, *16*, 1699–1710.

(182) Barca, G. M.; Gilbert, A. T.; Gill, P. M. W. Simple Models for Difficult Electronic Excitations. *J. Chem. Theory Comput.* **2018**, *14*, 1501–1509.

(183) Ambroise, M. A.; Jensen, F. Probing Basis Set Requirements for Calculating Core Ionization and Core Excitation Spectroscopy by the Δ Self-Consistent-Field Approach. *J. Chem. Theory Comput.* **2018**, *15*, 325–337.

(184) Chakraborty, T.; Rai, S. N. Comparative study of infrared and Raman spectra of CCl4 in vapour and condensed phases: Effect of LO–TO splitting resulting from hetero-isotopic TD–TD interactions. *Spectrochimica Acta Part A: Molecular and Biomolecular Spectroscopy* **2006**, *65*, 406–413.

(185) Eustatiu, I. G.; Tyliszczak, T.; Hitchcock, A. P.; Turci, C. C.; Rocha, A. B.; Bielschowsky, C. E. Experimental and theoretical study of generalized oscillator strengths for C 1s and O 1s excitations in CO_2. *Phys. Rev. A* **2000**, *61*, 042505.

(186) Sham, T. K.; Yang, B. X.; Kirz, J.; Tse, J. S. K-edge near-edge x-ray-absorption fine structure of oxygen- and carbon-containing molecules in the gas phase. *Phys. Rev. A* **1989**, *40*, 652–669.

(187) Heller, E. J.; Stechel, E. B.; Davis, M. J. Molecular spectra, Fermi resonances, and classical motion. *The Journal of Chemical Physics* **1980**, *73*, 4720–4735.

(188) Wang, C.; Wright, R. Raman studies of the effect of density of the fermi resonance in CO2. *Chemical Physics Letters* **1973**, *23*, 241–246.

(189) Adachi, J.-i.; Kosugi, N.; Shigemasa, E.; Yagishita, A. Renner–Teller splitting in the C 1s→ π^* excited states of CS 2, OCS, and CO 2. *The Journal of chemical physics* **1997**, *107*, 4919–4926.

(190) Antonsson, E.; Patanen, M.; Nicolas, C.; Benkoula, S.; Neville, J.; Sukhorukov, V.; Bozek, J.; Demekhin, P. V.; Miron, C. Dynamics of the C 1 s→ π^* excitation and decay in CO 2 probed by vibrationally and angularly resolved Auger spectroscopy. *Physical Review A* **2015**, *92*, 042506.

(191) Jahn, H. A.; Teller, E. Stability of polyatomic molecules in degenerate electronic states-I—Orbital degeneracy. *Proceedings of the Royal Society of London. Series A-Mathematical and Physical Sciences* **1937**, *161*, 220–235.

(192) Knight, L. B.; Steadman, J.; Feller, D.; Davidson, E. R. Experimental evidence for a C2v (2B1) ground-state structure of the methane cation radical: ESR and ab initio CI investigations of methane cation radicals (CH_4^+ and $CD_2H_2^+$) in neon matrixes at 4 K. *Journal of the American Chemical Society* **1984**, *106*, 3700–3701.

(193) Boyd, R. J.; Darvesh, K. V.; Fricker, P. D. Energy component analysis of the Jahn–Teller effect in the methane radical cation. *The Journal of chemical physics* **1991**, *94*, 8083–8088.

(194) Baker, S.; Robinson, J. S.; Haworth, C.; Teng, H.; Smith, R.; Chirilă, C. C.; Lein, M.; Tisch, J.; Marangos, J. P. Probing proton dynamics in molecules on an attosecond time scale. *Science* **2006**, *312*, 424–427.

(195) Gonçalves, C. E. M.; Levine, R. D.; Remacle, F. Ultrafast geometrical reorganization of a methane cation upon sudden ionization: an isotope effect on electronic non-equilibrium quantum dynamics. *Phys. Chem. Chem. Phys.* **2021**, *23*, 12051–12059.

(196) Beynon, J. H., *Mass spectrometry and its applications to organic chemistry.* Elsevier Pub. Co.: Amsterdam; New York, 1960.

(197) Tachikawa, H. Dynamics of Electron Attachment and Ionization Processes in the CCl_4 Molecule: An ab Initio MO and Direct Dynamics Study. *The Journal of Physical Chemistry A* **1997**, *101*, 7454–7459.

(198) Harvey, J.; Tuckett, R. P.; Bodi, A. Shining new light on the multifaceted dissociative photoionisation dynamics of CCl 4. *Physical Chemistry Chemical Physics* **2014**, *16*, 20492–20499.

(199) Kinugawa, T.; Hikosaka, Y.; Hodgekins, A. M.; Eland, J. H. D. New results on the dissociative photoionization of CF_4 and CCl_4. *Journal of Mass Spectrometry* **2002**, *37*, 854–857.

(200) De la Vega, J. M. G.; Miguel, B.; San Fabian, E. Density functional calculations on Jahn-Teller effect of tetrachloromethane cation. *International Journal of Quantum Chemistry* **1997**, *61*, 533–540.

(201) Karplus, M.; Porter, R. N.; Sharma, R. D. Exchange reactions with activation energy. I. Simple barrier potential for (H, H2). *J. Chem. Phys.* **1965**, *43*, 3259–3287.

(202) Jolly, W.; Bomben, K.; Eyermann, C. Core-electron binding energies for gaseous atoms and molecules. *At. Data Nucl. Data Tables* **1984**, *31*, 433–493.

(203) Potts, A.; Lempka, H.; Streets, D.; Price, W. Photoelectron Spectra of the Halides of Elements in Groups III, IV, V and VI. *Philosophical Transactions for the Royal Society of London. Series A, Mathematical and Physical Sciences* **1970**, 59–76.

(204) Dixon, R.; Murrell, J.; Narayan, B. The photoelectron spectra of the halomethanes. *Molecular Physics* **1971**, *20*, 611–623.

(205) Mao, Y.; Loipersberger, M.; Horn, P. R.; Das, A.; Demerdash, O.; Levine, D. S.; Prasad Veccham, S.; Head-Gordon, T.; Head-Gordon, M. From Intermolecular Interaction Energies and Observable Shifts to Component Contributions and Back Again: A Tale of Variational Energy Decomposition Analysis. *Annual review of physical chemistry* **2021**, *72*, 641–666.

(206) Drewello, T.; Weiske, T.; Schwarz, H. Cl2C-Cl-Cl^+, Cl2C-Cl-Br^+, and Br2C-B-C^+ by Gas-Phase Decarbonylation of CX3COY^+. *Angewandte Chemie International Edition in English* **1985**, *24*, 869–870.

(207) Kime, Y. J.; Driscoll, D. C.; Dowben, P. A. The stability of the carbon tetrahalide ions. *J. Chem. Soc., Faraday Trans. 2* **1987**, *83*, 403–410.

(208) Muto, H.; Nunome, K.; Iwasaki, M. An electron spin resonance study of the structure of $CCl_4{}^+$ radical cation in carbon tetrachloride irradiated at low temperatures by powder and single crystal analyses. *The Journal of Chemical Physics* **1989**, *90*, 6827–6832.

(209) Caldwell, C. D.; Krause, M. O.; Cowan, R. D.; Menzel, A.; Whitfield, S. B.; Hallman, S.; Frigo, S. P.; Severson, M. C. Inner-shell photoexcitation in an open-shell atom: The Cl 2 $\vec{p}$ ns, md spectrum as a case study. *Phys. Rev. A* **1999**, *59*, R926–R929.

(210) Nayandin, O.; Kukk, E.; Wills, A. A.; Langer, B.; Bozek, J. D.; Canton-Rogan, S.; Wiedenhoeft, M.; Cubaynes, D.; Berrah, N. Angle-resolved two-dimensional mapping of electron emission from the inner-shell $2p$ excitations in Cl_2. *Phys. Rev. A* **2001**, *63*, 062719.

(211) Nesbitt, D. J. Toward state-to-state dynamics in ultracold collisions: Lessons from high-resolution spectroscopy of weakly bound molecular complexes. *Chemical Reviews* **2012**, *112*, 5062–5072.

(212) Hernández-Lamoneda, R.; Sanz-Sanz, C.; Roncero, O.; Pio, J. M.; Taylor, M. A.; Janda, K. C. A theoretical study on electronic predissociation in the NeBr2 van der Waals molecule. *Chemical Physics* **2012**, *399*, 86–93.

(213) Dota, K.; Garg, M.; Tiwari, A.; Dharmadhikari, J.; Dharmadhikari, A.; Mathur, D. Intense two-cycle laser pulses induce time-dependent bond hardening in a polyatomic molecule. *Physical Review Letters* **2012**, *108*, 073602.

(214) Mathur, D.; Dota, K.; Dharmadhikari, A.; Dharmadhikari, J. Carrier-envelope-phase effects in ultrafast strong-field ionization dynamics of multielectron systems: Xe and CS 2. *Physical Review Letters* **2013**, *110*, 083602.

(215) Lindsay, B. G.; McDonald, K. F.; Yu, W. S.; Stebbings, R. F.; Yousif, F. B. Electron-impact ionization of CCl_4 and CCl_2F_2. *The Journal of Chemical Physics* **2004**, *121*, 1350–1356.

(216) Burton, G. R.; Chan, W. F.; Cooper, G.; Brion, C. Valence-and inner-shell (Cl 2p, 2s; C 1s) photoabsorption and photoionization of carbon tetrachloride. Absolute oscillator strength (5–400 eV) and dipole-induced breakdown pathways. *Chemical physics* **1994**, *181*, 147–172.

(217) Geissler, D. Concerted elimination of Cl_2^+ from CCl_4 and of I_2^+ from CH_2I_2 driven by intense ultrafast laser pulses `http://ultrafast.physics.sunysb.edu/grouptheses/Dominik_thesis_electronic%20version%20final%20fixed.pdf`.

(218) Efros, A. Density of states and interband absorption of light in strongly doped semiconductors. *Soviet Physics Uspekhi* **1974**, *16*, 789.

(219) Schirhagl, R.; Chang, K.; Loretz, M.; Degen, C. L. Nitrogen-vacancy centers in diamond: nanoscale sensors for physics and biology. *Annual review of physical chemistry* **2014**, *65*, 83–105.

(220) Katz, E.; Willner, I.; Wang, J. Electroanalytical and bioelectroanalytical systems based on metal and semiconductor nanoparticles. *Electroanalysis: An International Journal Devoted to Fundamental and Practical Aspects of Electroanalysis* **2004**, *16*, 19–44.

(221) Verkamp, M.; Leveillee, J.; Sharma, A.; Lin, M.-F.; Schleife, A.; Vura-Weis, J. Carrier-Specific Hot Phonon Bottleneck in CH3NH3PbI3 Revealed by Femtosecond XUV Absorption. *Journal of the American Chemical Society* **2021**, *143*, 20176–20182.

(222) Brown-Altvater, F.; Antonius, G.; Rangel, T.; Giantomassi, M.; Draxl, C.; Gonze, X.; Louie, S. G.; Neaton, J. B. Band gap renormalization, carrier mobilities, and the electron-phonon self-energy in crystalline naphthalene. *Physical Review B* **2020**, *101*, 165102.

(223) Ulbricht, R.; Dong, S.; Chang, I.-Y.; Mariserla, B. M. K.; Dani, K. M.; Hyeon-Deuk, K.; Loh, Z.-H. Jahn-Teller-induced femtosecond electronic depolarization dynamics of the nitrogen-vacancy defect in diamond. *Nature communications* **2016**, *7*, 1–6.

(224) Porter, I. J.; Cushing, S. K.; Carneiro, L. M.; Lee, A.; Ondry, J. C.; Dahl, J. C.; Chang, H.-T.; Alivisatos, A. P.; Leone, S. R. Photoexcited small polaron formation in goethite (α-FeOOH) nanorods probed by transient extreme ultraviolet spectroscopy. *The journal of physical chemistry letters* **2018**, *9*, 4120–4124.

(225) Vlasov, I. I.; Shenderova, O.; Turner, S.; Lebedev, O. I.; Basov, A. A.; Sildos, I.; Rähn, M.; Shiryaev, A. A.; Van Tendeloo, G. Nitrogen and luminescent nitrogen-vacancy defects in detonation nanodiamond. *Small* **2010**, *6*, 687–694.

(226) Drake, M.; Scott, E.; Reimer, J. Influence of magnetic field alignment and defect concentration on nitrogen-vacancy polarization in diamond. *New Journal of Physics* **2015**, *18*, 013011.

(227) Chang, S. L.; Barnard, A. S.; Dwyer, C.; Boothroyd, C. B.; Hocking, R. K.; Ōsawa, E.; Nicholls, R. J. Counting vacancies and nitrogen-vacancy centers in detonation nanodiamond. *Nanoscale* **2016**, *8*, 10548–10552.

(228) May, P. W. Diamond thin films: a 21st-century material. *Philosophical Transactions of the Royal Society of London. Series A: Mathematical, Physical and Engineering Sciences* **2000**, *358*, 473–495.

(229) Bressler, P.; Lübbe, M.; Zahn, D.; Braun, W. X-ray absorption spectroscopy study of different solid carbon modifications. *Journal of Vacuum Science & Technology A: Vacuum, Surfaces, and Films* **1997**, *15*, 2085–2087.

(230) Henderson, G. S.; De Groot, F. M.; Moulton, B. J. X-ray absorption near-edge structure (XANES) spectroscopy. *Reviews in Mineralogy and Geochemistry* **2014**, *78*, 75–138.

(231) Buades, B.; Moonshiram, D.; Sidiropoulos, T. P.; León, I.; Schmidt, P.; Pi, I.; Di Palo, N.; Cousin, S. L.; Picón, A.; Koppens, F., et al. Dispersive soft x-ray absorption fine-structure spectroscopy in graphite with an attosecond pulse. *Optica* **2018**, *5*, 502–506.

(232) Laikhtman, A.; Gouzman, I.; Hoffman, A.; Comtet, G.; Hellner, L.; Dujardin, G. Sensitivity of near-edge x-ray absorption fine structure spectroscopy to ion beam damage in diamond films. *Journal of applied physics* **1999**, *86*, 4192–4198.

(233) Brandes, J. A.; Cody, G. D.; Rumble, D.; Haberstroh, P.; Wirick, S.; Gelinas, Y. Carbon K-edge XANES spectromicroscopy of natural graphite. *Carbon* **2008**, *46*, 1424–1434.

(234) Manson, N. B.; Hedges, M.; Barson, M. S.; Ahlefeldt, R.; Doherty, M. W.; Abe, H.; Ohshima, T.; Sellars, M. J. NV—N+ pair centre in 1b diamond. *New Journal of Physics* **2018**, *20*, 113037.

(235) Shigley, J. E.; Breeding, C. M. Optical defects in diamond: A quick reference chart. *Gems & Gemology* **2013**, *49*, 107–111.

(236) Duan, X.; Wang, C.; Pan, A.; Yu, R.; Duan, X. Two-dimensional transition metal dichalcogenides as atomically thin semiconductors: opportunities and challenges. *Chemical Society Reviews* **2015**, *44*, 8859–8876.

(237) Böker, T.; Severin, R.; Müller, A.; Janowitz, C.; Manzke, R.; Voß, D.; Krüger, P.; Mazur, A.; Pollmann, J. Band structure of MoS 2, MoSe 2, and α- MoTe 2: Angle-resolved photoelectron spectroscopy and ab initio calculations. *Physical Review B* **2001**, *64*, 235305.

(238) Gusakova, J.; Wang, X.; Shiau, L. L.; Krivosheeva, A.; Shaposhnikov, V.; Borisenko, V.; Gusakov, V.; Tay, B. K. Electronic properties of bulk and monolayer TMDs: theoretical study within DFT framework (GVJ-2e method). *physica status solidi (a)* **2017**, *214*, 1700218.

(239) Zhou, D.; Shu, H.; Hu, C.; Jiang, L.; Liang, P.; Chen, X. Unveiling the growth mechanism of MoS2 with chemical vapor deposition: from two-dimensional planar nucleation to self-seeding nucleation. *Crystal Growth & Design* **2018**, *18*, 1012–1019.

(240) Chen, J. G. NEXAFS investigations of transition metal oxides, nitrides, carbides, sulfides and other interstitial compounds. *Surface Science Reports* **1997**, *30*, 1–152.

(241) Han, M.; Luo, Y.; Moryl, J.; Osgood Jr, R.; Chen, J. A near-edge X-ray absorption fine structure study of atomic layer epitaxy: the chemistry of the growth of CdS layers on ZnSe (100). *Surface science* **1998**, *415*, 251–263.

(242) Vegelius, J. R.; Kvashnina, K.; Hollmark, H.; Klintenberg, M.; Kvashnin, Y.; Soroka, I. L.; Werme, L.; Butorin, S. M. X-ray spectroscopic study of Cu2S, CuS, and copper films exposed to Na2S solutions. *The Journal of Physical Chemistry C* **2012**, *116*, 22293–22300.

(243) Li, D.; Bancroft, G.; Kasrai, M.; Fleet, M.; Yang, B.; Feng, X.; Tan, K.; Peng, M. Sulfur K-and L-edge X-ray absorption spectroscopy of sphalerite, chalcopyrite and stannite. *Physics and Chemistry of Minerals* **1994**, *20*, 489–499.

(244) Allen, M. J.; Tung, V. C.; Kaner, R. B. Honeycomb carbon: a review of graphene. *Chemical reviews* **2010**, *110*, 132–145.

(245) Novoselov, K. S.; Geim, A. K.; Morozov, S. V.; Jiang, D.; Katsnelson, M. I.; Grigorieva, I.; Dubonos, S.; Firsov, a. Two-dimensional gas of massless Dirac fermions in graphene. *nature* **2005**, *438*, 197–200.

(246) Artyukhov, V. I.; Penev, E. S.; Yakobson, B. I. Why nanotubes grow chiral. *Nature Communications* **2014**, *5*, 1–6.

(247) Bachilo, S. M.; Strano, M. S.; Kittrell, C.; Hauge, R. H.; Smalley, R. E.; Weisman, R. B. Structure-assigned optical spectra of single-walled carbon nanotubes. *science* **2002**, *298*, 2361–2366.

(248) Reich, S.; Dworzak, M.; Hoffmann, A.; Thomsen, C.; Strano, M. Excited-state carrier lifetime in single-walled carbon nanotubes. *Physical Review B* **2005**, *71*, 033402.

(249) Park, J.; Reid, O. G.; Blackburn, J. L.; Rumbles, G. Photoinduced spontaneous free-carrier generation in semiconducting single-walled carbon nanotubes. *Nature communications* **2015**, *6*, 1–8.

(250) Hertel, T.; Fasel, R.; Moos, G. Charge-carrier dynamics in single-wall carbon nanotube bundles: a time-domain study. *Applied Physics A* **2002**, *75*, 449–465.

(251) Mehlenbacher, R. D.; Wang, J.; Kearns, N. M.; Shea, M. J.; Flach, J. T.; McDonough, T. J.; Wu, M.-Y.; Arnold, M. S.; Zanni, M. T. Ultrafast exciton hopping observed in bare semiconducting carbon nanotube thin films with two-dimensional white-light spectroscopy. *The Journal of Physical Chemistry Letters* **2016**, *7*, 2024–2031.

(252) Mehlenbacher, R. D.; Wu, M.-Y.; Grechko, M.; Laaser, J. E.; Arnold, M. S.; Zanni, M. T. Photoexcitation dynamics of coupled semiconducting carbon nanotube thin films. *Nano letters* **2013**, *13*, 1495–1501.

(253) Grechko, M.; Ye, Y.; Mehlenbacher, R. D.; McDonough, T. J.; Wu, M.-Y.; Jacobberger, R. M.; Arnold, M. S.; Zanni, M. T. Diffusion-assisted photoexcitation transfer in coupled semiconducting carbon nanotube thin films. *ACS nano* **2014**, *8*, 5383–5394.

(254) Cushing, S. K.; Porter, I. J.; de Roulet, B. R.; Lee, A.; Marsh, B. M.; Szoke, S.; Vaida, M. E.; Leone, S. R. Layer-resolved ultrafast extreme ultraviolet measurement of hole transport in a Ni-TiO2-Si photoanode. *Science advances* **2020**, *6*, eaay6650.

(255) Miyata, Y.; Mizuno, K.; Kataura, H. Purity and defect characterization of single-wall carbon nanotubes using Raman spectroscopy. *Journal of Nanomaterials* **2011**, *2011*.

(256) Brzhezinskaya, M.; Baitinger, E.; Belenkov, E.; Svirskaya, L. Defect electron states in carbon nanotubes and graphite from the NEXAFS spectroscopy data. *Physics of the Solid State* **2013**, *55*, 850–854.

(257) Saeed, A.; Elsayed, A. A.; Marty, F.; Nefzaoui, E.; Bourouina, T.; Shawkey, H. A.; Sabry, Y. M.; Khalil, D. In *MOEMS and Miniaturized Systems XIX*, 2020; Vol. 11293, 112930U.

(258) Kumanek, B.; Janas, D. Thermal conductivity of carbon nanotube networks: A review. *Journal of materials science* **2019**, *54*, 7397–7427.